Dynamic Analysis of Magnetorheological Elastomer Configured Sandwich Structures

by
Won Jun Choi

A thesis submitted for the degree of **Doctor of Philosophy**

School of Engineering Sciences
University of Southampton, Highfield
Southampton SO17 1BJ

June 2009

UNIVERSITY OF SOUTHAMPTON

ABSTRACT

FACULTY OF ENGINEERING, SCIENCE AND MATHEMATICS
SCHOOL OF ENGINEERING SCIENCES

Doctor of Philosophy

DYNAMIC ANALYSIS OF MAGNETORHEOLOGICAL ELASTOMER CONFIGURED SANDWICH STRUCTURES

by Won Jun Choi

The work presented in this thesis is concerned with the investigation of the dynamic behaviour of magnetorheological elastomers (MREs) and smart sandwich structures. An extensive review, covering existing smart materials and their applications, has highlighted that smart materials and structures can be applied to large scale structures. Comprehensive experimental tests have been carried out in order to gain knowledge and data on the dynamic shear properties and behaviour of stiffness change of MRE and MRE cored adaptive sandwich beam structures depending on magnetic fields. Dynamic shear property tests with different curing stages have been enhanced to obtain various properties. The new developed forced vibration test rig enabled forced vibration tests of MRE embedded sandwich beam with various aspects such as different magnetic field strength, various oscillations of force amplitudes, boundary conditions and damping effects under localised magnetic fields to be made. In parallel to these experimental investigations, a new theoretical model was developed by combining the magnetisation effects on iron particles in terms of the curing times. In addition, a new macro scale modelling approach for rubber like materials (nonlinear behaving materials) was made by adopting FEA analysis to obtain the optimum volume of pores and size of iron particles to enhance the performance of MREs. A higher order sandwich beam theory is extended to include damping properties of MRE. It has been demonstrated that a higher order sandwich beam theory appears to be the most versatile and accurate modelling method for a sandwich beam with an MRE core material. The results from higher order theory have been combined with a power flow analysis for the smart floating sandwich raft vibration isolation system. Finally, an experimental study was performed to illustrate the control capabilities of MRE adaptive vibration absorber for a propeller shaft in real time. From this research work, a better understanding of the dynamic behaviour of MRE embedded sandwich beam has been acquired.

Contents

List of Tables

*

List of Figures

*

Acknowledgements

I would like to express my deep sense of gratitude to my supervisors Prof. Ajit Shenoi and Dr. Yeping Xiong for their continuous interest, encouragement, inspirational guidance, suggestions, unselfish help and support through out this research.

I am thankful to Prof. Mike Brennan for the valuable advice and providing me experimental facilities in ISVR for my research work. I also wish to express my appreciation to Professor Jong Gye Shin from the Seoul National University in Korea for his consistent encouragement. I owe my deepest gratitude to Dr. Esa Yunus for helping me to work with SEM, Richard Fruehmann for helping me to carry out with material tests. I equally wish to extend my appreciation and thanks to Dr. Nick Townsend, Dr. Suleiman Abu-Sharkh and Dr. Ajaya Nayak for their useful discussions. I wish to thank to the technicians, Rob, Kris, David and Eric in TSRL and EDMC for their endless advice and help making experimental device. Mike in cryogenics laboratory for his advice on magnetic experimental setup.

It is an honour for me to acknowledge the greatest support from Republic of Korea Navy. I also wish to acknowledge defense Attache, ROK Navy Captain Jin Kyu Kim, for his endless support. I am indebted to many of my Korean friends and colleagues in the University and their families to support me.

I am deeply in debt to my parents, parents-in-law, and their families. This acknowledgement will not be complete without expressing my gratitude to my wife, Jae Min, and my son, Sung Hwan for their warmest love and long patience. Without their supports, sacrifices, encouragement, and everything they have done for me, it was impossible to carry out this work.

Nomenclature

English Alphabet

Upper Case Symbols

A	shear area
A_t, A_b	cross sectional areas of the top and bottom skin
B	magnetic flux density
E^*	complex Young's modulus of the skin
E_c^*	complex Young's modulus of the core
E', E''	storage and loss Young's modulus of the skin
E_c', E_c''	storage and loss Young's modulus of the core
E_{ref}	reference Young's modulus
G_0	base shear modulus without magnetic field
G_{host}	shear modulus of host elastomer
G_{mag}	magnetically pre-yield shear modulus
G_c^*	complex shear modulus of the core
G_c', G_c''	storage and loss shear modulus of the core
H	Hermitian transpose
H	magnetic field strength
I_t, I_b	second moments of inertia of the top and bottom skin
L	length of the beam
M_p	average particle polarization
M_s	saturation polarization of the particles
M_{xx}^p	bending moment of the skin

M_i, M_r	values of the induced and regime magnetisations
N_{xx}^p	axial force of the skin
P_i	power flow through any interface of the ith substructure
R	radius of iron particle
R_i	radius of each particle
S_i (i=1,...,n)	substructures in general coupled system
T	kinetic energy
U	strain energy
U_{host}	strain energy density of a host elastomer
U_{mag}	strain energy density of a magnetically induced elastomer

Lower Case Symbols

b	width of the beam
d	particle diameter
h	the gap between particles in a chain
m_t	mass per unit length of the top skin
m_b	mass per unit length of the bottom skin
m_c	mass per unit length of the core
dv	volume of a differential segment
$q_n^p(t)$	time dependent coordinates
r	distance between the origin of each particle
t	time in seconds
u_b, u_t	displacement of bottom and top skin in the horizontal direction
u_c	displacement of core in the horizontal direction
$\dot{u}_b$, $\dot{u}_t$	velocity of bottom and top skin in the longitudinal direction
$\dot{u}_c$	velocity of core in the horizontal direction
v_{bot}, v_{top}	volume of bottom and top skin
v_{core}	volume of the core

w_b, w_t	displacement of bottom and top skin in the vertical direction
w_b	displacement of core in the vertical direction
$\dot{w}_b$, $\dot{w}_t$	velocity of bottom and top skin in the vertical direction
$\dot{w}_c$	velocity of core in the vertical directions
x	longitudinal co-ordinate
x_a	location where concentrated load applied

Greek Alphabet

α	fractional unsaturated area of particle
α_x	uniaxial stress-strain parameter
β	curve fitting constant
γ_c	the shear strain in the core
δ	variation operator
tanδ	loss angle
ϵ	normal strain
ϵ_{xx}^t	longitudinal normal strain in the top skin
ϵ_{xx}^b	longitudinal normal strain in the bottom skin
ϵ_{zz}	vertical normal strain in the core
η	modal loss factor
λ^*	complex eigenvalue
$\lambda_n^{'}$	real eigenvalue
$\lambda_n^{''}$	imaginary eigenvalue
λ_x (x=1, 2, 3)	principal extension ratio
μ_0	magnetic permeability of a vacuum (4$\pi\times$10^{-7}H/m)
μ_1	relative permeability
ν_x	uniaxial stress-strain parameter
ξ	damping ratio
ρ_c	density of core

σ_{xx}^{t}	longitudinal normal stress in the top skin
σ_{xx}^{b}	longitudinal normal stress in the bottom skin
σ_{zz}	vertical normal stress in the core
τ	time constant varied by temperature
τ_c	shear stress in the core
ϕ	volume fraction of particles
$\varphi_n^{(5)}$	normal mode functions for the base structure
$\psi_n^p(x)$	mass normalised mode shapes
ω_n	resonance frequency

Matrix and Vector Notations

$\mathbf{A}_i^e$	equivalent mobility matrix of substructure
$\mathbf{A}_i$	generalized mobility matrix
$\mathbf{F}$	vector of force applied
$[\mathbf{K}^*]$	complex stiffness matrix
$[\bar{\mathbf{K}}^*]$	complex stiffness matrices
$[\mathbf{M}]$	mass matrix
$[\bar{\mathbf{M}}]$	ordinary symmetric matrices of the mass
$\mathbf{N}_i^v$	velocity transmissibility matrix
$\mathbf{e}_z$	unit vector in z direction
$\mathbf{m}_i$	dipole moment of spherical shape of each iron particle
$\mathbf{v}_i$	velocity response vector
$\hat{\mathbf{v}}_{n+1}$	unit velocity input
$\hat{\mathbf{v}}_{n+1}$	boundary motion excitations
$[\Lambda]$	matrix of eigenvectors

Other Symbols

$\dot{()}$	derivative with respect to time
$\ddot{()}$	second derivative with respect to time

Abbreviations

AUV	autonomous underwater vehicle
ERF	electrorheological elastomer
MRE	magnetorheological elastomer
MRF	magnetorheological fluid
MSMA	magnetic shape memory alloy
MsS	magnetostrictive sensor
PFC	piezoceramic fibre composite
PVC	Polyvinyl chloride
PVDF	polyvinyldene flouride
PZT	lead zirconate titanate
SEM	scanning electron microscopy
SMA	shape memory alloy
SMP	shape memory polymer
TVA	tuneable vibration absorber

Chapter 1

Introduction

Smart materials have been used to tackle vibration problems with various control schemes. Smart materials, such as piezoelectric materials, shape memory alloys, controllable fluids and elastomers, have the abilities as sensors, actuators and controllers by adding some amount of secondary sources such as thermal, magnetic or electric energy. A lot of studies and applications for aircraft, astronautics and civil engineering to attenuate vibration problem using smart materials have been developed. However, up until now, less effort has been focused at ship structures. A ship structure is subjected to various kinds of dynamic loads exciting ship vibrations which not only affect operation and health of crew on board but cause damages to ship and its cargo. These vibration sources have been controlled by structural modification of local supporting structure in a passive way. However, when the frequency ranges of vibration source of ship structure are variable, the passive control scheme is no longer suitable. This is to say, it is essential to adopt smart materials to attenuate vibration forces. Smart materials have been used by means of bonding or embedding to composite or sandwich structures. A sandwich structure consists of two laminated skins and one core material which can be tailored to produce stiffened structural properties by several means of lamina or ply. The greatest advantage with sandwich structure is that the strength and stiffness are increased without a corresponding increase in the weight. The increasing uses of sandwich structure is mainly due to its advantages of light weight, high stiffness and strength. The other advantage of sandwich structure is its adaptiveness. This has brought about the requirement for smart sandwich structures. In this study, magnetorheological elastomer (MRE) is mainly considered as a core material in a sandwich structure in this thesis.

The aim of this thesis is to present the use of MRE to reduce the vibration problems in large scale ship structures. The principal objectives of the thesis are accordingly

- To achieve the better performance of MRE through the dynamic shear property test with various aspects in conjunction with the enhanced theory and macro scaled finite element analyses;
- To investigate dynamic behaviour of MRE core configured smart sandwich structure in terms of different magnetic field and various boundary conditions, as well as to estimate the changes of resonant frequencies and modal damping of the MRE configured sandwich beam using higher order sandwich beam theory;
- To apply smart sandwich structure as a floating raft vibration isolation system through a power flow analysis;
- To explore a potential application of smart vibration absorber for a propeller shaft in the ship structure.

Chapter 2

Literature Review on Smart Materials and Smart Structures

2.1 Background

The term smart structures might come from wide acceptance of knowledge of structures that responsed in a reasonable way to environmental stimuli and self-actuate without external human intervention. A smart structure can also be called an active structure (Wada *et al.* , 1990), an intelligent structure (Crawley, 1992), and an adaptive structure when a smart material is adapted to a conventional structure, which involves some vital factors including static structural material, integral components such as sensors, processors and actuators that sense a force from the environment and adjust the shape, making the structure more rigid or more flexible depending upon the force (Clark *et al.* , 1998).

Smart structures can be controlled by smart materials which can change their shape or properties under power such as electrical voltages or magnetic fields. Smart materials such as piezoelectric, electrorheological, magnetorheological materials and shape memory alloy are designed into structures by means of embedding or bonding to structural surfaces directly and utilized as actuators, sensors and feedback controllers.

The development of smart materials has provided the potential feasibilities and changed design methodologies of structures. As a result, smart structures could not merely control structural responses in terms of stimuli, but could include adaptations and feedback which can adjust stimuli continuously. The purpose of using smart structures is to make the structure more adaptive than conventional structures. An important factor is to minimize the life cycle cost. For instance, inappropriate initial design may lead to catastrophic disaster to buildings in an instant. Smart suspension of building structures can absorb energy of earth tremors instead of trying to resist the tremor forces. Once sensors detect structural changes, actuators could minimize vibration forces and reduce or eliminate damage.

Smart materials should be used where low maintenance cost is required. For example, when cracks occur inside a structure, embedded healing agent can detect and cure structural damage without any intervention whereas a conventional structure would be required to be observed and repaired by human. If a tremendous expenditure for maintaining a building is taken into consideration, using smart structures provides an attractive solution to attenuate the cost of maintenance, although the initial cost is high.

2.2 Smart Materials

Recently developed smart materials, such as piezoelectric materials, shape memory alloys, controllable fluids and elastomers have opened a new approach for structural control. Most smart materials that are able to act as actuators allow smart structures to adapt to their changing environment.

Table 2.1 shows smart materials in terms of stimulus/input and response/output. Smart materials can change their stiffness, shape, viscosity or other properties by means of variations in electrical field, magnetic field, or temperature. Each smart material has a broad range of parameters in terms of its function. In this study, the viewpoint of mechanical response with various stimuli is considered for applications to large scale marine structures.

Table 2.1: Categorising smart materials

Stimulus / Input	*Mechanical*	*Electrical*	*Optical*	*Magnetic*	*Heat*
Response / Output					
Mechanical	Auxetics Thixotropics	Piezoelectric Electrostrictive Piezo-resistive	Photostrictive	MR Fluid MR Elastomer	Shape Memory Alloy (SMA) SM Polymer (SMP)
Electrical	Piezoelectric Electrostrictive	Ferroelectrics	Photovoltaic		Thermoelectric Electrocaloric
Optical	Electrochromic			Magneto-optic	
Magnetic		Magnetoelectric Paramagnetic Diamagnetic	Magneto-optic		
Heat		Thermoelectric Electrocaloric		Magnetostrictive MagnetoCaloric	
Structural health monitoring		PZT Electrostrictive Piezo-resistive	Fibre optics	Magnetostrictive Sensor (MsS)	
Self healing and repairing	Micro-encapsulated chemicals				SMA SMP
Shape control (Actuator)	Auxetics Shear thickening fluids	ER material Piezoceramic fibre composite (PFC)		Magnetic shape memory alloy (MSMA)	SMA SMP
Vibration and noise control		PZT PVDF ER material		MR Fluid MR Elastomer	SMA SMP

2.2.1 Piezoelectric materials

Piezoelectric materials generate an electric field along their surface when subjected to a mechanical stress. On the other hand, piezoelectric materials show a shape change when an electrical field is applied. It can be compressed or expanded depending on the polarity of electrical field. PZT (lead zirconate titanate) and PVDF (polyvinyldene flouride) have been used either as an actuator or as a sensor. PVDF exhibits piezoelectricity several times greater than quartz. Unlike ceramics, where the crystal structure of the material creates the piezoelectric effect, in polymers the intertwined long-chain molecules attract and repel each other when an electric field is applied. Most piezoelectric actuators and sensors, either surface bonded or embedded in the host structures for the adaptive structure system, are based on either its extension or shear mechanism. Piezoelectric materials are rather rapid (msec - range) in the small deformation. Piezoceramics have a high structural stiffness, which can afford them a strong and voltage dependent actuation authority. Since high voltages correspond precisely to only tiny changes in the width of crystal, piezoceramics are used as common rail diesel fuel injection in a car (Randall *et al.* , 2005). Recently, intensive efforts have been focused on developing high performance piezo-actuators which are supposed to be applicable to vibration suppression of large structures such as marine and aerospace structures, actuating control surface of small-scale airplanes, morphing wing sections and so on (Buter & Breitbach, 2000).

The increase of high performance and flexibility of actuators has resulted in the increase of requirement of actuator as shape control. Shape control is determined by the required range of displacement and agility of the system. Studies on piezoceramic fibre composite (PFC) actuators have been carried out theoretically and experimentally. Due to being conformable, durable and more responsive than regular monolithic devices (Lloyd, 2004), PFCs exhibit the best application of piezoelectric materials. Many examples of applications are airplane wings to improve aerodynamic lift and reduce drag, rotor blades to increase hub lift and reduce vibrations due to imbalance and reflector surfaces to improve the antenna performance (Marc, 1998). Macro Fiber Composite actuator has been developed by NASA Langly Research Center (LaRC-MFC^{TM}), and it has been used for commercial purpose. MFC strain performance exceeds by up to 150% (Wilkie *et al.* , 2000).

Since piezoelectric materials do not need windings, they can be fixed to a structure and do not require electrical or mechanical commutation. However, there are several disadvantages to implement this sensitive type of material; in a way, the brittle nature of ceramic makes them vulnerable to accidental breakage during handling and bonding procedures. Piezoelectric fibre composite technology has also difficulties associated with processing during actuator manufacture and the high actuator voltage requirements (Yoshikawa *et al.* , 1999). Moreover, their small range (e.g. 0.2 % strain of PZT) of mechanical motion may not apply to large scale structures.

2.2.2 Shape memory alloys

Shape memory alloys (SMAs) are those that remember their geometry. SMAs produce a significant shear strain induced by temperature change; they are normally made in the shape of wires or foils. The length of an SMA wire or foil can be reduced when heated and can be brought back to its original geometry by cooling. These are owing to a temperature-dependent phase transformation from a low-symmetric to a highly symmetric crystallographic structure. The former, martensite, is more changeable at the lower temperature phase present in shape memory alloys whereas the latter, austenite, is stronger at the higher temperature phase. The nickel titanium alloy (e.g. Nitinol, for Nickel Titanium Naval Ordnance Laboratory) exhibits strain up to about 8% and will recover its original shape when it is heated above its activation temperature (Dittrich, 1998). Since various shapes of SMA can be used for different purposes, SMA wires can be embedded or attached to host structures as hybrid composites which have a combination of two or more reinforcement fibres or material. Due to the novelty of changing its elastic modulus, SMA could be a vibration absorber (Rustighi *et al.* , 2005), a shape controller (Oh *et al.* , 2001) and a device for self repairing (Peairs *et al.* , 2004). Among the major challenges of using SMA is the considerable dependence of the control schemes on the external temperatures.

SMAs have low bandwidth and are well suited mainly for slow actuation requirements. SMAs would be appropriate when a large displacement and slow response are required. However, SMAs have poor fatigue properties. While under the same loading conditions such as twisting, bending and compressing, SMA elements may survive for much less times than a steel component. Moreover, the slow response characteristic of SMA actuators is incompatible with high speed controller.

2.2.3 Controllable fluids

Controllable fluids can change their viscosity by external stimuli such as electric and magnetic forces with rheological behaviour. There are two commercial fluids known as electrorheological fluids (ERFs) and magnetorheological fluids (MRFs). ERFs are kinds of smart material with variable viscosity depending on varying electric field intensity. ERFs consist of some type of low viscosity insulating liquid, mixed with nonconductive particles usually in the range of 1-10μm diameter. When the electric field intensity reaches an outset value, ERF will change from liquid to a solid-like structure, exhibiting solid like characteristics as shown in Fig. 2.1. The change is almost instantaneous, within a few milliseconds or so. Reversely, when the electric field is removed, ERF will be changed from the solid-like structure back to liquid instantaneously. Yield stresses in shear for modern materials are of the order of 10 kPa for static loading, and 5 kPa for dynamic loading (Block & Kelly, 1988).

Due to advantages of these novel properties, ERFs have been used for tactile sensation to human interaction with computers for vehicular instrument control

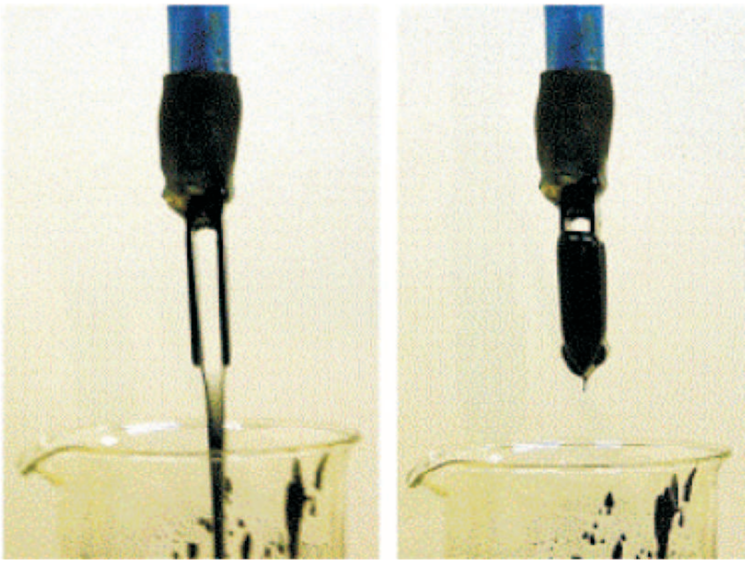

Figure 2.1: Electrorheological (ER) fluid (a) Non-activated (b) Activated (Weinberg *et al.* , 2005)

(Weinberg *et al.* , 2005). However, they require high voltages. The increase in electric field across the ERF from 0 to 2 kV is proportional to an increase of 25 - 50 % in equivalent viscous damping (Phani & Venkatraman, 2003). In addition, they require a very high dielectric constant to generate a large electomechanical coupling. Furthermore, they are vulnerable to contamination easily, therefore affecting the structural integrity of smart structural systems (Madden *et al.* , 2004).

Magnetorheogical fluids (MRFs) consist of micron sized magnetically permeable particles suspended in a non-magnetic medium. Properties of MRFs can be controlled by the application of a magnetic field. Although research into MRFs started at the end of the 1940's (Rabinow, 1948), only in recent years have their potential applications as semi-active dampers for vehicles, buildings and bridges been recognised (Carlson & Jolly, 2000; Ginder *et al.* , 2000; Jolly *et al.* , 1999). MRFs produce a strain under the change of a magnetic field by micron sized magnetisable particles dispersed in a carrier medium. Their viscosity changes with the application of an external magnetic field. MRFs could be used where controlled vibration and impact energy dissipations are required. MRFs are being developed for use in car suspensions (Carlson & Jolly, 2000), washing machines, building foundations and bridges. MRFs have been used for semi-active control devices and have the properties that can be controlled to optimally reduce the response of the large scale systems such as buildings and bridges (Ribakov & Gluck, 2002).

A selective controllable base isolation system with MR dampers has been developed to improve the seismic behavior of multistory building (Ribakov & Gluck, 2002) and to reduce pier drifts (Sahasrabudhe & Nagarajaiah, 2005) respectively. The rheological and magnetic properties of several commercial MR dampers are presented by Jolly *et al.* (1999). The full-sized MR seismic damper is shown in Fig. 2.2. The damper utilizes a particularly simple geometry where the outer cylindri-

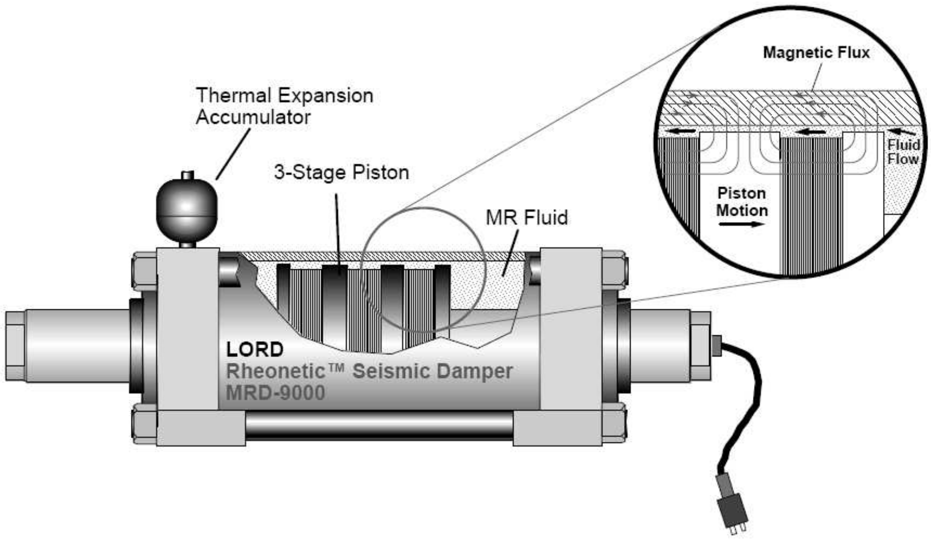

Figure 2.2: MR seismic damper (Jolly *et al.* , 1999)

cal housing is part of the magnetic circuit. The fluid orifice is the entire annular space between the piston outside diameter and the inside of the tubular damper housing. Movement of the piston makes the fluid to flow through this entire annular region. The damper is double ended, that is, the piston is supported by a shaft on both ends.

There are several differences between MR and ER fluids as described in Table 2.2. The increase of external magnetic field strength causes the increase of MR viscosity. The advantages of MRFs are that they are less affected by contaminant. Therefore, they can be adapted to structures in saline environments. MRFs are operated directly from low-voltage power supplies. Operational powers for MRFs span from 2 to 25 V while ERF requires high electrical fields from 2 kV to 5 kV. Due to the strong dipole interaction of the magnetic particles of the filler, MRFs have relatively high yield stress while ERFs have low yield stresses, of the order of only several kPa. Their temperature ranges from -50 to +150 °C, i.e. ranges that are generally common during manufacture and usage. On the other hand, ERFs are quite sensitive to the pollutants. Particularly moisture or especially water which adversely influences the strength of this material. Due to the suspended iron particles, problems with both ERFs and MRFs are clump, deposition, environmental contamination and sealing problems, which have so far prevented their wide application.

Table 2.2: Comparison of properties of typical MR and ER fluids (Carlson & Jolly, 2000; Housner *et al.* , 1997)

Properties	*MR Fluids*	*ER Fluids*
Max yield stress τ_y	50-100 kPa	2-5 kPa
Operational temperature range	-50-150°C	10-90°C
Stability	Not affected by most impurities	Cannot tolerate impurities
Response time	ms	ms
Density	3-4 g/cm^3	1-2 g/cm^3
Power supply (typical)	2-25 V 1-2 A (2-50 W)	2-5 kV 1-10 mA (2-50 W)

2.2.4 Controllerable elastomers

Electrorheological elastomers

The principle of electrorheological (ER) elastomers is similar to that of ER fluids. When elastomers, comprising natural or synthetic rubber, have polarizable particles dispersed in them, then they can undergo changes in properties while subjected to an electric field or a magnetic field. The applications include variable stiffness mounts, such as engine mounts, made from the composition.

ER elastomers have exhibited up to 380% strain when they are highly prestrained at 5 to 6kV (Pei *et al.* , 2004) as well as large elastic energy density. Due to excellent space saving characteristics, they could be used for multi-degrees of freedom robot legs (Pei *et al.* , 2004). A good example is ER elastomers as actuator, which can produce different resistive torque value or shear stress depending on the applied voltage and mode. Using these novel feature of ER elastomers, a small working robot with spring roll, as each of its six legs made of electro elastomer (Pei *et al.* , 2004), has been developed. These actuators exhibit large strain and have many advantages of lightweight, compact, powerful interfaces and operate effectively (Sherrit, 2005). However, due to the low elastic modulus, ER elastomers can not make massive power to actuate high stiffened structures. The strain depends on the elastic modulus of the polymer and the strain-electric field relationship of electro-rheological material is nonlinear at large strains.

Magnetorheological elastomers

Magnetorhelogical elastomers (MREs) are composed of tiny ferrous particles in chains and an elastomer such as synthetic rubber or natural rubber. In particular, the incorporation of filler particles is known to increase the stiffness of the material, change the strain history dependence of the stiffness and alter time-dependent aspects of material behaviour such as hysteresis and stress relaxation (Bergstrom, 1999). When liquid state rubber combined with ferrous particles is exposed to a steady magnetic field, the ferrous particles will form chain-like structures arranged along the magnetic field as shown in Fig. 2.3. The key difference between MREs and MRFs is that MRFs are liquid and used in viscosity controllable devices whereas MREs are solid and used for stiffness controllable devices (Zhou & Wang, 2005). The most noteworthy aspect is that the particle chains within the elastomer composite are intended to always operate in the pre-yield regime while MRFs typically operate in a post-yield continues shear or flow regime (Jolly *et al.* , 1996a). MREs are a durable material which can be operated in severe temperatures (-50°C to 150°C) with low voltage supplies.

These magnetic field sensitive materials with tunable elastic properties may find many applications in elastomer bearings and vibration absorbers. MREs can be used in applications where stiffness or resonance frequency change is needed (Jolly *et al.* , 1999). In recent years their potential capability has been increasingly recognised as semi active control devices in car suspensions. The Toyota central R&D laboratory has developed an engine mount (Shiga *et al.* , 1992) and Ford motor company have developed an automotive bushing (Watson, 1997) with MREs in order to improve passenger comfort.

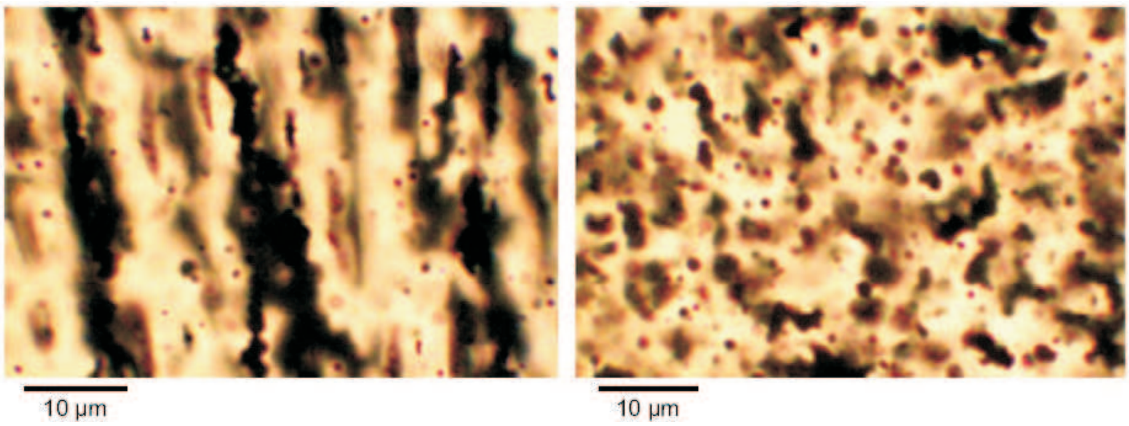

Figure 2.3: Aligned MRE particles under the magnetic field (left) and randomly dispersed MRE particles without magnetic filed (right) (Stepanov *et al.* , 2007)

2.3 Smart Material Control Systems

Apart from the use of better functional materials as sensors and actuators, an important part of a smart structure is to develop an optimized control system that could lead the actuators to perform required functions after sensing changes. Control systems could be active, semiactive or passive. The key difference between ″active″ and ″passive″ surely is related to the fact that for the former one needs to sense the response and stimulus and then have an algorithm that adjusts the response for certain stimuli that would otherwise have been undesirable whereas in the latter case there is no sensing law rather reliance placed solely on the intrinsic characteristics of the materials or structural system to adjust response ″automatically″ or ″naturally″ according to preordained / determined laws or characteristics.

An active control system is a mechanical system with the ability to alter its configuration, form or properties in response to changes in the environment rapidly. Active control systems can change output value of an object directly by adapting force actuators whereas the only way for passive system is isolating or attaching damping patch on vibrating sources. Active control systems have been applied to a wide variety of objects such as machines, structures and biological systems etc. The advance of processing technology in piezoelectric materials has also been benefiting their successful applications in the special requirement of structures. In active control systems, there are many smart structures integrated with the piezoelectric materials for the particular demand in accomplishing a variety of sophisticated mechanical tasks through a feedback systems such as active control of noise and vibration. Such systems are used to control the response of structures to internal or external excitation, such as vibration and noise control, shape control and structural health monitoring, where the safety or comfort level of the occupants is of concern. An active control system needs many requirements. Target structure must have structural integrity to carry the design loads. The process of actuation should not affect negatively the strength of structure. Unlike passive systems, active systems require consistent external power in order to responded to stimuli in real time. Due to the consistent power requirement of actuating control system and high initial cost, active vibration control system are less used than passive systems (Liu *et al.* , 2005).

A semi-active control system is a class of active control system for which the external energy requirements are orders of magnitude smaller than typical active control system (Zhang, 2001). Semi-active control devices are often considered as controllable passive devices (Housner *et al.* , 1997). Therefore it combines the advantages of active system and passive system, such as energy efficiency and low life cycle cost. Semi-active systems also need external power sources, but always on a constant basis. Therefore semi-active control system is applied to suspension control buildings and bridges against seismic force which is instant rather than constant (Ribakov & Gluck, 2002). A passive control system does not need an external power source and does not make any real-time changes in the system. In case of vibration field, the control manner of passive systems is just to impart energy developed in response to the motion of the structure (Housner *et al.* , 1997). Therefore, its control bandwidth is narrow and fixed at initial designed values. The term passive control is closely related to isolation. As a result, passive control system can be made by means of being cut out, shaped and formed into components for structures, using viscoelastic material in the structure, using vibration or impact damper, or using tuned mass dampers. The difference between passive and active control system is that passive control does not make any real-time changes in the system. Even though initial cost of passive system is relatively low, life cycle cost including maintenance and redesign could be high. Passive vibration isolation (Dong *et al.* , 2006), tuned mass damping (Setareh *et al.* , 2006) and self healing systems are examples of passive control system.

Comparisons of three control systems for smart structures are shown in Table 2.3. Comparing all systems, power sources should be provided in active and semi-active system to make any real time control whereas passive system does not require power sources. Control mechanism of the active system is adding and dissipating energy while semi-active system is using bounded input and output energy. Therefore, an active control system should be accompanied by auxiliary actuators whose scale is in proportion to the size of the structure like ship structure. However passive system just imparts energy from one to another properly. The active and semi-active systems have variable control bandwidth whereas passive system has fixed control bandwidth. Even though the initial cost of the active system is high, life cycle cost is low whereas the initial cost of passive system is relatively inexpensive but life cycle cost is high.

Table 2.3: Comparison of active, semi-active and passive systems

	Active system	*Semi − active system*	*Passive system*
Energy requirement	Large	Little	None
Control mechanism	Add and dissipate energy	Bounded input and output	Impart energy
Control bandwidth	Wide, Variable	Narrow, Variable	Narrow, Fixed
Design methodology	Embedding and bonding another actuator	Combination of active and passive systems	Cut out, Shaped, Formed into components for structures, Tuned mass, Viscoelastic material, Damper
Initial cost / Life cycle cost	High / Low	Medium / Low	Low / High
Applications	Active vibration and noise control	Tuned vibration absorber	Vibration and noise isolation
	Actuator (Shape controller)	Semi-active joint	Self healing
	Structural Health Monitoring		
Applicable smart materials	Piezoelectric, SMA	ME Fluid, MR Elastomer, ER Fluid, ER Elastomer, SMA	Self repairing material

Adaptive passive control system, an alternative to both passive and active system, is generally used to control plants whose parameters are unknown or uncertain (Housner *et al.* , 1997). An adaptive passive control is described by Bernhard *et al.* (1992) as a fourth classification of vibration control. Adaptive passive vibration control combines a tunable passive device with a tuning strategy such that optimal performance is guaranteed (Franchek *et al.* , 1996). Typical adaptive control applications reported includes temperature control, automobile cruise control, and ship steering control (Tao, 2004). If the amount of uncertainty is too large to be compensated by a fixed controller, or the structural parameters may have unpredictable variations so that gain scheduling may be inadequate, then in these cases an adaptive controller should be considered. Since the device of changing damping or stiffness operates in an on and off manner, the control does not require to switch rapidly. And it is well applicable to vibration isolation of rotating machines (Liu *et al.* , 2005) and adaptive tuned vibration absorber (TVA). It can be tuned to suppress the modal contribution to the vibration of a troublesome natural frequency of the host structure over a wide band of frequencies.

2.4 Marine Applications with Smart Structures

Ranging from automotive systems, optical systems, space mechanical machine, medical systems and infrastructures, smart-structures technology is a highly interdisciplinary field. Many applications have been explored by using different kinds of smart materials such as piezoeclectric, magnetorheological (MR), electrorheological (ER) materials and shape memory alloys (SMAs). Each smart material has its own features with respect to different purposes. Even same smart material which has a unique property could be adapted to different applications. For instance, SMAs are used either as a vibration absorber (Humbeeck & Kustov, 2005), a shape controller (Oh *et al.* , 2001) or a self repairing device (Peairs *et al.* , 2004). Piezoelectric materials are used as a sensor for structural health monitoring as well as an actuator for shape control.

2.4.1 Structural health monitoring

Light weight ships such as yachts, fishing boats and even naval vessels are increasingly using composite materials to take advantages of their excellent specific strength, stiffness properties and low electromagnetic signature. However, they have one of the greatest risks since damage can lead to catastrophic failures. Composite structures tend to fail by damages in distributive or interactive nature, which are easy to meet a number of failure modes different from steel structures. Agarwal & Broutman (1990) showed that the internal material failure can appear in many forms, i.e.

- Breaking of the fibres
- Micro-cracking of the matrix
- Separation of fibres from each other in a laminated composite (Debonding)
- Separation of laminae from each other in a laminated composite (Delamination)

Structural health monitoring (SHM) system has the ability to detect material failure and interpret adverse 'changes' in a structure in order to improve reliability and reduce life-cycle costs (Kessler *et al.* , 2002). The expected benefit of the SHM system in an FRP structure is the reduction of inspecting cost for large marine structures and improving structural reliability.

As the size of composite ships has been increased, there will be a need for developing an efficient monitoring method for defects in composite submerged structures in order to estimate life cycle of composite ship structures effectively. Even though there are many methods for non-destructive testing within the structures for small laboratory specimens such as X-radiographic detection and hydro-ultrasonics, these are not appropriate for in-service inspection of submerged ship's structure. Techniques based on static displacement response and static strain measurement which involve the measurement of actual displacement and strains are not an easy task on large scale structures (Tseng & Naidu, 2002). Moreover, damage detection in composites is more difficult than in metallic structures owing to the anisotropy of material (Kessler *et al.* , 2002).

Thus the optical fibre sensors have been used as a structure monitoring sensor whose advantages have led to several techniques. The applicability of using fiber-optic sensor has been examined (Kageya *et al.* , 1998). Stress concentrations or residual strains resulted from an impact damage can be detected by fibre optic sensors. Suresh *et al.* (2005) developed Fiber Bragg Grating (FBG) based shear force sensor. Dawood *et al.* (2007) demonstrated embeded FBG strain sensors within a foam core glass fibre reinforced plastic (GFRP) sandwich composite beam specimen. Baldwin *et al.* (2002) carried out monitoring of the UK Trimaran Research Vessel by using Digital Spatial Wavelength Domain Multiplexing (DSWDM) which can determine strain level as well as monitor frequency response of the ship due to wave slamming event. Herszberg *et al.* (2005) used FBG sensor and piezoelectric strain sensor for structural health monitoring for composite T-joint. The optical fibre sensor has potential advantages as a structure monitoring sensor such as applicability to dynamic measurement and is less affected by temperature. However, it has difficulty in detecting the displacement change with frequency less than 1Hz (Kageya *et al.* , 1998). In other words, high resolution data can be acquired, but it cannot travel long distance such as the hull structure of a large vessel.

Piezoelectric materials are the key materials for structural health monitoring. With these materials, ultra sonic wave techniques which have been used to interrogate structural integrity could be suitable for long-range inspection. Diamanti *et al.* (2005) demonstrated the potential of low-frequency ultra sonic waves being used for the inspection of monolithic and sandwich composite beams. Yang & Qiao (2005) carried out damage detection of composite structures by using the pulse-echo method. Kessler *et al.* (2002) performed quasi-isotropic graphite / epoxy test using piezoelectric actuators and sensors. Unlike waves on a planar surface, frequency dispersion occurs for surface waves propagating along a curved surface

(Überall, 1973). Sahin (2004) predicted severity and location of the damage by using as input the global (natural frequencies) and the local (strain or curvature mode shapes) dynamic behaviour of the structure.

Due to the significant difference between the acoustic impedance of each laminated skin, the dispersion effects at low frequencies and multi-curved shells should be considered simultaneously in composite ship structures. Since their range of mechanical motion is small, piezoelectric materials may not apply to large scale structures. Moreover, the brittle nature of ceramic makes them vulnerable to accidental breakage during handling and bonding procedures.

2.4.2 Self healing and repairing

Self healing can make the material safer, more reliable longer lasting and require less maintenance cost especially for a ship structure subjected by unexpected loading condition such as hydraulic slamming or underwater explosions. It is also useful to make up healing agent only for small amount of crack in initial stage. Self healing structures react to damage producing some action to restore it to its undamaged condition (Peairs *et al.* , 2004) followed by air curing of the released chemicals in the cracks, leading to regaining of mechanical properties of uncracked composite (Li *et al.* , 1998). Once the glass fibers break, the chemical agent is released into the cracks of the polymer matrix so that the cracks can be sealed and the composite can be rehealed. Significant crack arrest and life extension result when the in situ healing rate is faster than the crack growth rate (Brown *et al.* , 2005). However, using agent for self healing material could be only one shot affair rather than permanent measure for continual loads such as wave forces.

Shape memory alloys (SMAs) have been used as actuator in a self repairing joint. Layered SMA/PVDF films in flexible satellites were demonstrated as a self healing system with a SMA-driven bolted joint that senses change and tightens itself (Hyde & Agnes, 2000), which can reduce the maintenance cost of critical bolted joints. In case of SMA actuator for self repairing joint, it should be provided with high amount of power source as well as the time for heating and cooling to reach each state (i.e. martensite and ostenite). Thus, SMAs due to their slow response, low efficiency, unpredictable movement, have been only suitable for small-scale applications and high heated source is needed continuously.

2.4.3 Shape control

Smart structures featuring active shape control have the potential to extend the design point to a design area and significantly increase efficiency (Monner & Wierach, 2005). The fundamental structural task of a wing is transferring the loads between aerodynamic pressure and inertial forces. Adaptive wing can change the entire shape of the structures by using active control only requiring an electric current for movement (Hyde & Agnes, 2000). Buter & Breitbach (2000) introduced directly controlled helicopter blades by smart adaptive element such as piezoelectric or active fibres. Moreover, many experiments were carried out including various types of different kinds of space engineering, aerodynamic surfaces including airplane wing, twist-active rotor blades and missile fins which are compatible for high speed aerodynamics. Shape control actuators can unify various controls into a single control and transmit information effectively.

Three types of actuators for shape control including piezoceramic (PZT), electroelastomer and shape memory alloys (SMAs) are compared in Table 2.4. Electro elastomer exhibits high strain whereas piezoceramic displays low strain. Efficiency is the ratio of work generated to input energy consumed, which is almost same (90%) for piezoceramic and electro-elastomer while SMAs exhibit low efficiency. Young's modulus determines the actuator's passive ability to reject load changes, disturbances (Prendergast & McHugh, 2004). Young's modulus between piezocermaic and electro-elastomer is significantly different. Energy density is the ratio of energy generated in one actuator cycle per unit volume of actuator. SMAs exhibits very high energy density (15 J/Kg), whereas piezoceramic shows very low energy density (0.013 J/Kg). Despite their advantages of being ductile and gen-

Table 2.4: Parameters of three smart materials as actuators (Dittrich, 1998; Hodgson *et al.* , 2004; Madden *et al.* , 2004; Sodano, 2003; Wilkie *et al.* , 2000)

	PZT	VHB	$NiTiNol$
Actuation Principle	Piezoceramic	Electro elastomer	Shape Memory Alloys
Strain(%)	0.2	380	8
Efficiency(%)	90 (max) $<$ 50 (typical)	90 (max) 25 (typical)	$<$ 5
Young's modulus (GPa)	63	0.003	30 (Martensite) 90 (Austenite)
Energy density (J/Kg)	0.013	3.4×10^6	15
$T_{max}(°C)$	-20 to 200	-10 to 90	-100 to 200
Relative speed	Fast	Medium Fast	Slow

erating high strain (e.g. 100% of Shape Memory Polymer), many drawbacks also exist such as slow response, low efficiency, and unpredictable movement. They are only suitable for small-scale applications (Prendergast & McHugh, 2004), with a high heated source being needed continuously.

For marine applications, robust control is most difficult, especially for low speed submerged vehicles such as AUVs. These low speed vehicles need maneuvering capabilities such as hovering, small-radius turning, rising, sinking and precision station keeping. In order to overcome such limitations, many studies for low speed controller carried out based on biorobotics. This determines the goal of the biorobotics program, namely bridging the gap between nature and engineering by improving the performance of the latter as compared with the former (Bandyopadhyay, 2005). Therefore, shape control of structures could have different possible marine applications by using piezoelectric materials for precision adjustments of structures which requires more biological and less mechanical systems in submersible vehicles. Controllable pitch propellers are good example for low speed submersible vehicle, which could operate under a range of flow conditions (Madden *et al.* , 2004). These vehicles could benefit from the added efficiency maneuverability and the potentially low noise emissions afforded by variable shape propellers (Bandyopadhyay, 2002). However, it is difficult to adapt smart material to shells having complex geometry. High stiffened propellers, high required voltages to be applied for effective actuation: this is not always practicable. Moreover, encapsulation from salinity should also be considered.

High speed small and light submersible vehicle needs precise control while travelling to the target. Based on the recent developments such as missile fins (Barrett, 1994), adaptive blade twists (Buter & Breitbach, 2000) and double plated smart wings (Oh *et al.* , 2001), smart fins could be used to precise tolerances of high speed submersible vehicle. Small adjustment of high stiffness fin enables to actuate twist and bend and to save the space required for servomotors, force transmission devices and dynamic system. As a result, submersible smart fin could be adapted at any position of vehicle’s structure and could maximize the maneuvering capability. However, massive density of deep water and nonlinear vortices occurring from tips need to be considered.

For electrorheological materials, the strain depends on the elastic modulus of the polymer and the strain-electric field relationship is nonlinear at large strains. When it comes to the marine applications, considerable amount of power may be required in order to get a large amount of torque. In addition, they require a very high dielectric constant to generate a large electomechnical coupling. Moreover they are easily vulnerable to contamination, therefore affecting the structural integrity of smart structural systems.

2.4.4 Vibration and noise control

Attempts at reduction of vibration and noise in structures, have always been an important issue in mechanics ranging from small devices to large scale structures.

Patch type of piezoelectric materials have been broadly used as sensors and actuators using anti-oscillations in reduction of radiated noise (Hyde & Agnes, 2000; Lee, 2000; Monner & Wierach, 2005). This idea might be useful to ship compartments where radiated noise should be decreased for crew on board or naval mine countermeasure ship. Recent achievements made in designing and application of SMAs include high-damping elements, utilizing pseudoelastic hystersis, transient damping effects in the two-phase and damping capacity of the martensitic phase (Humbeeck & Kustov, 2005). SMA wires have been applied to active damping of flexural vibrations of a cantilever beam (Baz *et al.* , 1990a; Choi & Cheong, 1996). Due to the slow response of temperature, a tuned vibration absorber (TVA) has been established vibration control device, which can be used to suppress a troublesome resonance or to attenuate the vibration of foundations or joints for ship structures at a particular forcing frequency.

An MRE tuned vibration absorber (TVA) system can be developed with minimal engineering design changes to meet marine application handling over rough sea condition, sensitive electronic shock isolation for improved resistance to shock and impact damage. The MRE TVA device can modify mechanical systems' response to external disturbances through energizing an internal electromagnet so that unexpected vibratory loads can be dissipated through the activation of the MRE material via a closed loop control system. The MRE TVA system is argued to be fail-safe because the system will continue to manage device as a passive isolator in the event of a power system failure. It is shown that the MRE TVA absorbs achieved vibrating force from oscillating rigid mass and the relative frequency change is up to 47% with 60dB absorption of frequency response (Deng *et al.* , 2006).

An example learnt from application in audible frequency ranges is shown by Blom & Kari (2008). Fig. 2.4 shows the MRE isolator on an elastic base structure consisting of MRE bushing attached to an iron shell. It was shown that the transmitted energy flow into the base structure is significantly reduced. In addition, the MRE isolator not only suppresses vibration force but it also shunts resonant peaks in audible frequency ranges. Overall, these schematic ideas will help to reduce ra-

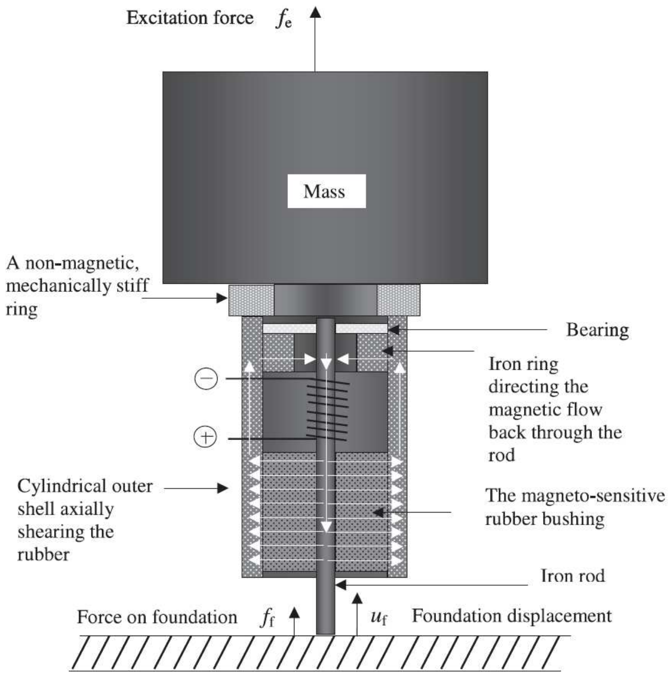

Figure 2.4: MRE isolator (Blom & Kari, 2008)

diated noise from the submerged structure such as naval ship's hull or submarine underwater, which can obtain the best possible counter-detection posture relative to enemy submarines.

2.5 Current Knowledge of MREs

2.5.1 Theoretical and numerical predictions of mechanical properties of MREs

Jolly *et al.* (1996b) shows the simple dipole model of particle energy interaction. In particular, it is seen that MR material stress is quadratically related to particle magnetization. This model takes into account the gradual saturation of the permeable particles as applied field increases. The preyield modulus G of the particle network is simply stress divided by strain,

$$G \cong \frac{4\phi M_p^2}{\mu_1 \mu_0 h^3}, \qquad \epsilon < 0.1 \tag{2.1}$$

where M_p is the average particle polarization and this is also the dipole moment magnitude per unit particle volume:

$$M_p = \frac{3/2\alpha^3 B + (1-\alpha^3)M_s}{1 + 3/2\phi\alpha^3}. \tag{2.2}$$

For tuned vibration absorber (TVA) employing MR elastomers, the fractional change in natural frequency can be calculated in terms of the fractional change in the modulus. Deng & Gong (2008) predicted frequency shift of one degree of freedom system for an adaptive tuned vibration absorber (ATVA) as bellows

$$\Delta f = \frac{1}{2\pi}\sqrt{\frac{G_0 \times A}{m \times h}}\left(\sqrt{1 + \frac{4\phi\mu_1\mu_0 M_s^2(\frac{R}{d})^3}{G_0}} - 1\right). \tag{2.3}$$

Dorfmann & Ogden (2003) have also summarized a system of constitutive equations for an isotropic magneto-sensitive Cauchy-elastic solid within the framework of the electromechanical and thermomechanical theories. The theory has been applied to the model problem of axial shear of a circular cylindrical tube in the presence of a radial magnetic field. They have shown theoretically, that the existence of a magnetic field makes the shear response of the MRE.

Structural FE analysis is used to predicted the stress-strain relationship for MR elastomers (Davis, 1998). An FE analysis with a typical mesh for the unit cell is used to find out optimal volume fraction of the iron particles as shown in Fig. 2.5. In this model the iron particles are considered as rigid spherical shells in a continuous matrix. The rubber matrix is described in terms of the principal extension ratios (λ_i), which are the ratios of the current length (deformed) to original (non-deformed) length in the principal directions. It was shown that the optimal particle volume fraction for the largest fractional change is about 27%. As a result, numerical model can be useful to ensure nonlinear macro scale behaviour MRE.

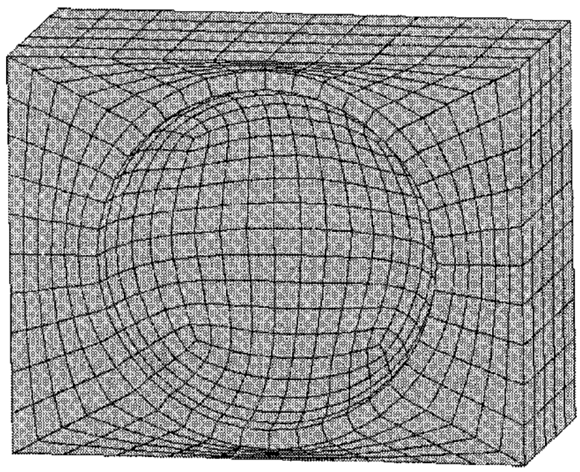

Figure 2.5: FEA mesh for unit cell of MRE (Davis, 1998)

2.5.2 Experimental study on MRE behaviour

The effort to increase the MR performance has been revealed by using different combinations of materials or various kinds of experimental schemes. The properties of MRE are affected by the volume fraction of the magnetic particles in the elastomer and the relative size and alignment of the particles after curing MRE under a magnetic field.

Jolly *et al.* (1999) showed that the maximum percentage of change in modulus is being observed in the vicinity of 1-2% strain. Performance of MRE can be enhanced by using different combinations of materials or through varied experimental and practical schemes. It has been also reported that cyclic loading conditions with different strain amplitudes manifest a dependence of the viscoelastic storage modulus with the maximum stiffness change being up to more than twice in the audible frequency range (Blom & Kari, 2005). It is shown that when the initial elastic modulus is small, up to 100% increase of the modulus has been observed at small 1-4% deformations and the loss factor of aligned MRE is tunable with magnetic flux density depending on frequency range (Varga *et al.* , 2006).

Lokander & Stenberg (2003) carried out the shear property tests using two different types of iron particles in order to find out substantial effect of MREs. It was shown that MREs with large irregular particles have a large MR effect although the particles are not aligned within the material. However the rheological properties of the matrix material do not influence the MR effect. Abramchuk *et al.* (2007) showed anisotrophic hehaviour of MRE by varying the direction of the applied magnetic field and the columnar structure of the particles. It has revealed that if the arrangements of the particles are parallel to the direction of the uniform magnetic field and to the applied force, the elastic modulus of the elastomers increases significantly with a magnetic field. Varga *et al.* (2006) reported that the most significant effect was found if the applied field is parallel to the particle alignment and to the mechanical stress.

Kallio (2005) has measured elastic/shear modulus and damping ratio/loss factor values by applying compressive loading with and without applied magnetic field. It was shown that MREs can change material damping depending on magnetic field strength. Stepanov *et al.* (2007) investigated viscoelastic behaviour of highly elastic magnetic elastomers by three different experimental techniques of elongation, static and dynamic shears.

2.5.3 MRE configured adaptive sandwich structure

MREs have been used to carry out vibration analysis to observe vibration responses in real time and vibration suppression capabilities of three layered MR adaptive sandwich beam structures (Sun *et al.* , 2003; Yalcintas & Dai, 2004). The development of MRE based adaptive structure was initiated only very recently. Zhou & Wang (2005) carried out theoretical study on MRE embedded smart sandwich beams with non-conductive skins based on higher order sandwich beam theory. Demchuk & Kuz'min (2002) measured the elastic modulus and loss factor using clamped vibrating sandwich beam.

2.5.4 MRE applications

Elastomers with field responsive rheology hold promise in enabling simple variable stiffness devices (Carlson & Jolly, 2000). Although MRE shows good performance for vibration minimisations, there are few applications appearing in the literature for controllable elastomers. The stiffness of the bushing is adjusted based on the state of the automobile's power train to reduce suspension deflection and improve passenger comfort.

Ford motor company has patented an automotive bushing employing a magnetorheological elastomer (Stewart *et al.* , 1998; Watson, 1997). MRE application for automotive bushing has been developed as shown in Fig. 2.6. Cross-section of an MRE bushing shows the wire coil that produces a magnetic field, the mild steel (or low-carbon steel) and magnetic circuit that delivers the field, and the MR elastomer material that responds to the field. The magnetic flux path is shown schematically by round arrow. Such tuneable components could for example minimize the effect of suspension resonances excited by torque variation caused by worn brake rotors by shifting the resonance away from the excitation frequency. Many suspension applications involve relatively large deflections at low frequencies (below 100 Hz) (Kallio, 2005). Toyota Central R&D Laboratory has also developed silicone gels containing Fe particles for tuneable engine mounts (Shiga *et al.* , 2003).

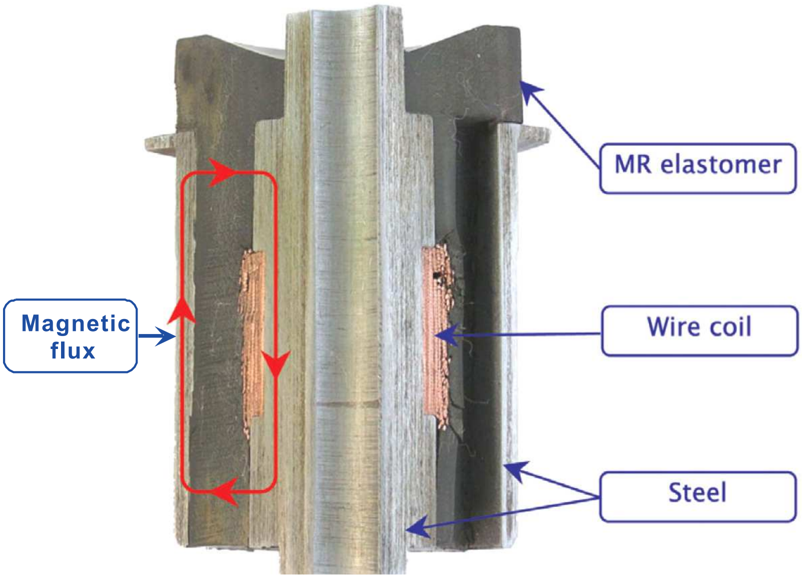

Figure 2.6: Variable stiffness bushing using MRE (Ginder *et al.* , 2000)

Kallio (2005) investigated the possibility of using magnetorheological elastomers as tunable spring elements as shown in Fig. 2.7. The coil device consisted of a bottom steel core and a moving top cover with a central steel plate to direct the load on the sample. A thin copper strip was coiled around the bottom core forming an energizing coil. When the sample was placed inside the bottom core and the top cover was closed, the coil current produced a magnetic field through the sample. It was shown that the damping properties of the MRE spring elements can be tuned using moderate flux densities. The effect of applied magnetic field on the damping properties is more pronounced at low frequencies and decreases with increasing testing frequency. As a result, MREs are applicable as tunable spring elements for

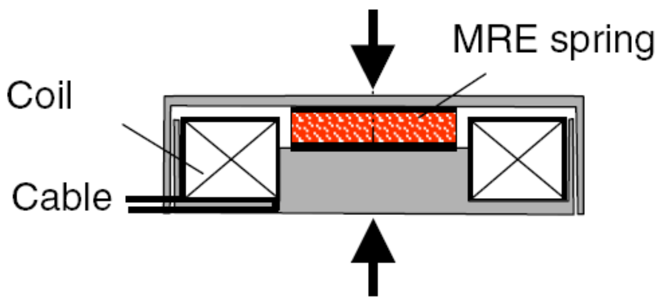

Figure 2.7: MRE spring under compressive load (Kallio, 2005)

active vibration control.

2.5.5 Summary

Within the context of this works key limitations in the current literature are as follows,

- The majority of the literature regarding MRE performance mainly considers the effects by changing material combinations. However, the effect of porosity and magnetisation on the iron particles in terms of various curing time under a magnetic field has not been considered, which could also enhance the performance of MRE materials. Therefore, new fabrication methods to predict air bubble effect and iron magnetisation without changing material components need to be considered.
- In conjunction with the experiments, enhanced theoretical prediction and the macro scale finite element analysis are needed to understand the behaviour of MRE because treatment of material uncertainty is more difficult issue in the tests.
- As far as MRE core configured sandwich structures, there has also been a limit of applying a magnetic field through a beam's height. The effect of boundary condition and localised magnetic field effect for damping have yet been discovered. As a result, new forced vibration test rig needs to be developed to apply a magnetic field through the height of the beam exactly and measure frequency response in terms of different boundary condition and various magnetic fields.
- Higher order sandwich beam theory needs to be enhanced to estimate the natural frequencies and modal damping of the MRE configured sandwich beam.
- Finally, potential applications regarding to the MRE vibration absorber for large ship structures are needed.

2.6 Summary and Conclusions

In this chapter a critical review of the different features and behaviours of smart materials and structures has been presented with the aim of establishing the most suitable smart materials that could be incorporated into the large scale marine structures. The following conclusions from this chapter should be outlined.

- Piezoelectric materials could be used for structural health monitoring, shape control and vibration control. Since their range of mechanical motion is relatively very small and the brittle nature of ceramic makes them vulnerable to accidental breakage during handling and bonding procedures, piezoelectric materials may not apply to large scale structures. Thus, piezoelectric fibre composite technology has also difficulties of processing during actuator manufacture and the high actuator voltage requirements.

- Due to a significant shear strain induced by temperature, SMAs have been used for shape control, vibration control and self reparing. However, SMAs have poor fatigue properties even if they have large energy density. Moreover, the slow response and low efficiecy characteristic of SMA is incompatible with variable environment for ship structures.

- From a view point of vibration and noise problems, there are disadvantages to implementing smart materials for large marine applications. MREs operate in the preyield regime and suppress force for large vibrational amplitude with small amount of energy. Therefore, an MRE TVA devices can be developed with minimal engineering design changes to meet other potential applications such as suspension elements for high speed boats to enhance ride quality and handling over rough sea condition and sensitive vibration and noise isolation for improved resistance to shock and impact damage.

Overall, the review presented in this chapter has clearly outlined the lack of use of smart materials for large scale marine application. However, the strong strain amplitude dependence of the MR effect could be the most suitable for vibration and noise insulation with minimal energy input. Such applications demonstrate that there are potentials for the use of MR materials in marine structures and therefore the study regarding to MRE is worthy of further investigations. The review also indicates the fact that there is a lack in current knowledge with respect to study of MRE. New works need therefore to be carried out in order to make up for the current weakness of the identified study. This should be linked with the realisation of further theoretical study and new experimental works in order to enhance the knowledge on the dynamic behaviour of MREs.

Chapter 3

Methodology and Approach of Thesis

As we have learned from the previous chapter, smart materials have shown many versatilities. As far as vibration problem is concerned for large structures, MRE is an appropriate material to attenuate vibrational energy. Fig.3.1 summarises the different aspects that need to be considered and highlights in italics the novelty and contribution to the knowledge base. The general overview of methodology and approach provided in this figure is explained in more detail following this figure. This study mainly consists of three parts - material behaviour, structural characterisation and potential application based on the comprehensive studies.

As indicated in the literary review, the majority of methods, regarding fabricating MRE, focus on material combinations to improve the performance. However, one must know that the material characteristics can be changed depending on different curing stage under a magnetic field. Development of fabrication method is required to be able to enhance the performance without changing material components. The magnetization effect on iron particles needs to be considered in terms of various curing stages under a magnetic field. The curing process with permanent magnet may be necessarily to cure MRE specimens in room temperature. On the other hand, the rheological property of elastomer material is also a crucial fact to determine MRE performance. The effect of pores which occur at the mixing stage needs to be considered. To confirm this porous effect comparison of specimens manufactured with and without vacuuming process is also required. Once specimens are made, the alignment of iron particles and microscaled pores distributed

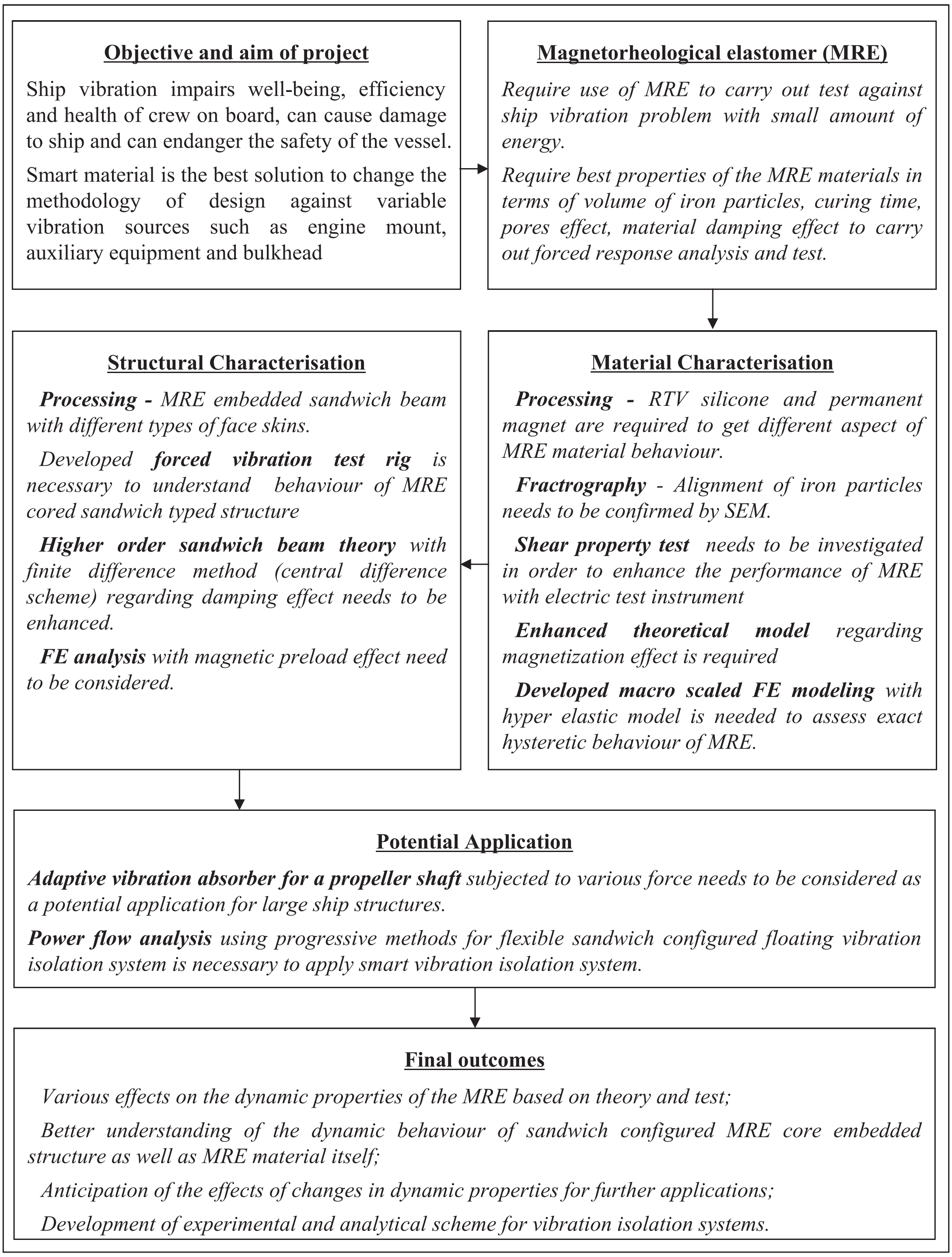

Figure 3.1: Methodologies and approaches of the thesis

in MRE need to be identified by a scanning electron microscope (SEM). Experimental work is necessary to compare property change of MRE material with various magnetic fields. It needs to be kept in mind that elastomeric behaviour of the MRE materials requires the knowledge of their complex dynamic moduli in small strain ranges. From dynamic shear property test, complex modulus of MRE core (i.e., shear modulus and damping ratio) can be determined. In addition, FE modelling approach is required to analyse elastomeric behaviours with rheological elastomer and iron particles. New macro scaled modeling aided by ABAQUS enables one to understand the porous effects and the characterisation of micron sized iron particles of MRE. To be able to carry out macro scaled analysis random distribution of individual particle elements evenly in hyper elastic behaving elements is required. This analysis will help to gain a better understanding on how rheological behaviour affects the property of MRE and will provide guidance for further fabrication with controlling pores.

Investigation on structural characterisation followed by material characterisation is needed to understand vibration characteristics of an MRE cored sandwich beam in terms of different boundary conditions, amplitude of force and various distributions of magnetic fields. A forced vibration test rig could consist of permanent magnets to provide consistent magnetic field in the vertical direction of the sandwich beam. In order to determine strain dependency the amplitude of force produced by the shaker needs to be controlled by an amplifier to provide different shear strain at the interfaces between core and face skins of sandwich beam. To estimate the natural vibration characteristics of a sandwich beam with stiff skins and soft core material like elastomers, the homogeneous solution including natural frequencies and corresponding modes need to be obtained. Then, the change of natural frequencies, mode shapes and damping would be obtained. Finally, the superposition of a series of natural modes would result in the net response to vibration.

Based on the analytical solution for sandwich structures, potential applications need to be presented. Theoretical power flow analysis using progressive methods for sandwich configured floating raft vibration isolation system based on vibration characteristics of different kinds of sandwich beam raft and base structures are presented. Higher order sandwich beam theory needs to be combined with power flow analysis when modelling sandwich beams with thin stiff face sheets and thick transversely flexible core to anticipate power transmitted to the base structure including viscoelastic material properties and their frequency dependencies. Experimental application needs to be carried out to ascertain the potential ability of MRE to absorb vibrations of propeller shafts when subjected to various vibration sources such as main engine, nonlinear hydraulic force and shaft misalignment. To be able to analyse this, simplified experimental works need to be carried out. A closed-loop electromagnet could be fitted around the cylindrical steel casing so that when required, a magnetic force could be applied to act on the MRE's physical properties to suppress the structural response of the long steel shaft with on and off control. A dynamic load needs to be provided by a shaker and the response signal needs to be measured by an accelerometer. Finally, enhancing the knowledge of MRE material is essential to improve understanding of the dynamic behaviour of smart sandwich structures.

Based on the methodology, chapter 4 describes the shear property of MRE based on static and dynamic shear property test.

Chapter 5 describes the comprehensive investigation on shear property of MRE including theoretical study and macro scale finite element analysis.

In chapter 6, based on the test on shear property of MRE, the result of forced vibration tests for MRE core configured sandwich beam are presented.

In chapter 7, analysis of the vibration characteristics aided by FEA solution and steady state analysis based on higher order sandwich beam theory of MRE cored sandwich beams are presented.

In chapter 8, the potential application of MRE as a vibration absorber for a propeller shaft is shown.

In chapter 9, numerical calculations for smart sandwich floating raft vibration isolation system are presented, without involving MRE core.

In the last part of this thesis, an overall discussion, conclusion and the achievements of the research study are presented. In addition, recommendations for further work on the subject are presented.

Chapter 4

Shear Property of MRE

4.1 Introduction

This chapter investigates the dynamic shear properties of MRE materials. A model accounting for the magnetisation effect on shear properties of MRE materials with respect to various curing times under a magnetic field is proposed. Since the rheological property of elastomer and magnetism of particles are critical factors to decide MR performance, the selection of particular types of elastomer and iron powders needs to be considered properly.

4.2 Material Selection

Different types of fillings and iron powders make for different properties of MRE. Many aspects (i.e.: type of elastomer, size and volume fraction of iron powder) which would directly affect the properties of MRE are presented in the literature (Blom & Kari, 2005; Deng *et al.* , 2006; Hu *et al.* , 2005; Kallio, 2005; Kallio *et al.* , 2007; Lokander, 2004; Lokander & Stenberg, 2003; Michaud-Cunningham, 2005; Shen *et al.* , 2004; Varga *et al.* , 2006).

Types of Matrices

Table 4.1 shows natural and synthetic elastomers used as a matrix material in the literature (Abramchuk *et al.* , 2007; Blom & Kari, 2005; Deng *et al.* , 2006; Hu *et al.* , 2005; Kallio, 2005; Lokander, 2004; Lokander & Stenberg, 2003; Michaud-

Cunningham, 2005; Varga *et al.* , 2006). The selection of the matrix influences the overall MR effect. For instance, the MR effect is smaller in the case of a hard matrix as compared to a softer matrix and carbonyl iron (Lokander, 2004). Natural rubber has been used with a mix of polybutadiene (Buna CB55) (Lokander & Stenberg, 2003) and thermoplastic elastomers. Therefore, the process of vulcanizing at high temperature is required for natural rubber though not for synthetic materials. As a consequence the process of fabrication for synthetic polymer is less complex than that of MR elastomer made of natural rubber. Consequently, room temperature vulcanizing (RTV) silicone materials such as RTV silicone 106 (Michaud-Cunningham, 2005), 704 silicone (Deng *et al.* , 2006) and Elastosil 604 (Varga *et al.* , 2006) have widely been used. Recently, hybrid type of elastomers

Table 4.1: Types of materials used as nonmagnetic elastomer matrix

Type	*Product*	*References*
Natural rubber		Blom & Kari (2005); Shen *et al.* (2004)
Polybutadien	Buna CB55	Lokander (2004)
Polyurethane	CC-950 Limestone	Shen *et al.* (2004)
RTV Silicone rubber	704	Deng *et al.* (2006); Hu *et al.* (2005)
	Elastosil M4644, M4601	Kallio (2005); Kallio *et al.* (2007)
	Elastosil 604A, 604B	Abramchuk *et al.* (2007); Varga *et al.* (2006)
	Elastosil R 101/25	Blom & Kari (2005)
	GE RED RTV 106	Michaud-Cunningham (2005)
Hybrid rubber		Blom & Kari (2005); Hu *et al.* (2005); Lokander (2004)

such as combinations of natural rubber and synthetic rubber have been investigated by Hu *et al.* (2005), Lokander (2004) and Blom & Kari (2005). Due to the field dependent rheological response of these elastomer composites, MRE with Elastosil M4644 (Wacker Co.) has shown its damping effect depending on variable magnetic field (Kallio, 2005). The moulded samples of these silicones do not shrink during curing. The stability and chemical neutrality of the system enables also the adhesive bonding to metals (Kallio, 2005). This silicone also shows medium shore A hardness (approximately 40), high tear strength, outstanding resistance to casting resins, particularly polyurethanes and epoxies, for very long service life of the moulds (Wackers Co.). Therefore, the nonmagnetic matrix elastomers used in this chapter are Elastosil M4644 (Wacker Co.).

Types of iron particles

The iron particles in MRE are typically micron sized particles of iron and iron based alloy. Table 4.2 shows different types of iron powders used as filler in MRE. Pure iron with irregular shape has been used in order to incorporate large amounts of oxygen into the elastomer (Lokander, 2004). It has been shown that MRE with large irregular particles has a large MR effect compared to nonaligned MRE (Lokander & Stenberg, 2003). Carbonyl iron, spherical iron particles with 3-10μm in diameter, is the particle type that has been widely used in MRE. This exhibits high saturation magnetisation and high stiffness change. Consequently, carbonyl iron particles (CIP CC, BASF Co.) have been used in this study.

4.3 The Shear Test Rig and Specimen Design

The shear property test rig, designed specifically for this work, consists of an electromagnet, an aluminum block to support a shear grip and electric test instrument (Instron ElectroPuls) as shown in Fig. 4.1(a). The ElectoPuls machine, operated by an electric current, has a 60 mm stroke and $\pm$ 1000 N dynamic load capacity in high frequency ranges. The diameter of the electro magnetic pole is 70 mm which is big enough to produce a magnetic field in the normal direction of specimen (20$\times$10

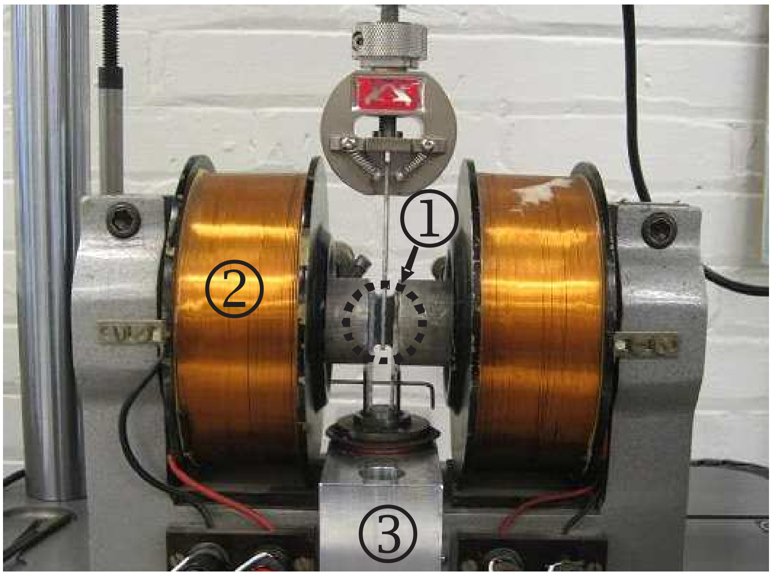

(a) Measurement instrument (1. shear test grip, 2. electromagnet, 3. aluminum block)

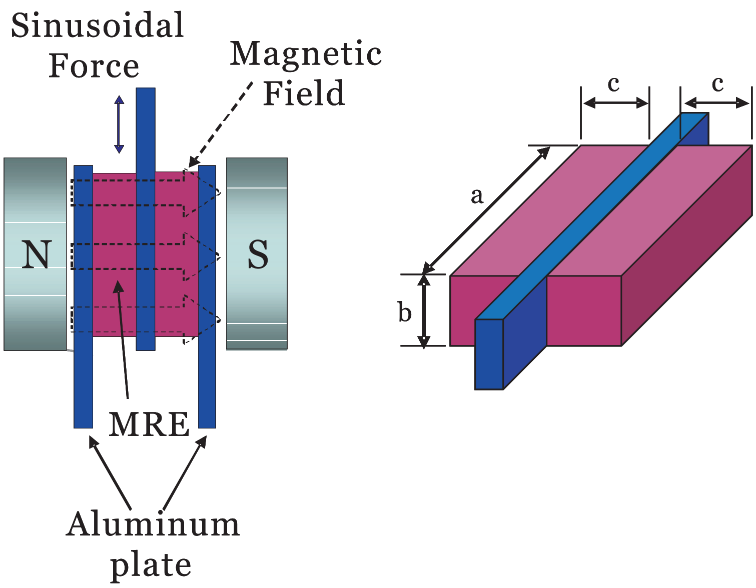

(b) Zoomed of the shear test grip

Figure 4.1: Dynamic property test setup with electromagnet

Table 4.2: Types of iron powders used as filler material of MRE

Type	*Product*	*Size* (μm)	*References*
Pure iron	ACS300	<60	Blom & Kari (2005); Lokander (2004)
	ACS100.29	<180	Lokander (2004)
	AT40.29	200	Lokander (2004)
Carbonyl ($Fe_2(C0)_9$) iron	BASF	2.5	Varga *et al.* (2006)
	BASF CIP-CC	3-10	Abramchuk *et al.* (2007); Deng *et al.* (2006)
	FTF-4	3-5	Hu *et al.* (2005); Wang *et al.* (2006)
	ISP R-1430	<6	Michaud-Cunningham (2005)
	ISP R-2521	5	Watson (1997)
	ISP S-3700	3-5	Ginder *et al.* (2002); Kallio (2005); Zhou (2003)

mm^2). The aluminum block is bolted to the base of the test machine, as illustrated in Fig. 4.1(a). The dimension of each specimen is 20×10×3 mm^3, which is fitted within the closed-loop electromagnet. The electromagnet is connected to an electric power supply and produces up to about 0.5 Tesla of magnetic field strength. When a sinusoidal oscillating displacement is applied, the magnetic field strength travels from one pole to the other as shown in Fig. 4.1(b). Then the load cell measures transmitted force from the specimen. The measured voltage signals are transfered to the high speed data logger where they are refined by a Butterworth low pass filter provided by Matlab.

The shear modulus (G′) can be calculated knowing the amplitude of sinusoidal displacement (ΔL) and transferred load (ΔF) as follows (Baccaredda *et al.* , 1967),

$$G' = \frac{\Delta F}{\Delta L}\frac{h}{4ab} \tag{4.1}$$

where a, b and h are length, thickness and width of two specimen ($h = 2c$) respectively. If the material being evaluated is purely elastic, the phase difference between the stress and the strain sine waves is $0°$. If the material is purely viscous, the phase difference is $90°$. However, most real-world materials, including

Figure 4.2: Degassing with vacuuming chamber

polymers, are viscoelastic and exhibit a phase angle that lies somewhere between $0°$ and $90°$. Since MRE is viscoelastic, this phase difference, together with the amplitudes of the stress and strain waves, can be used to determine a variety of fundamental material parameters such as storage modulus, loss modulus, transition temperature, creep and stress relaxation. By knowing the values of dynamic shear modulus (G') and loss angle (tan δ), the dynamic shear loss modulus (G'') can be determined through the following relationship,

$$G'' = tan\delta \cdot G'. \tag{4.2}$$

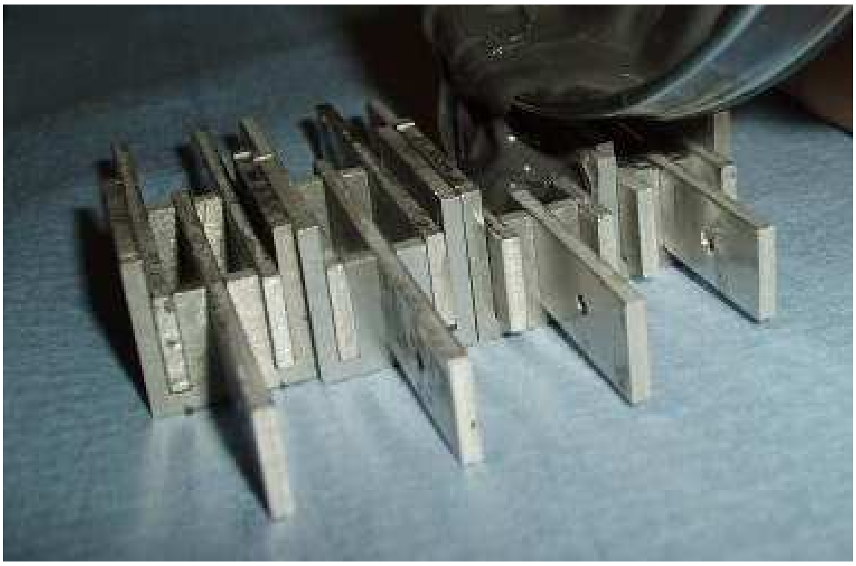

Figure 4.3: Pouring MRE to the prepared moulds to be cured under magnetic field with different time

4.4 Preparation of Shear Test Sample

RTV silicone including catalyst and 3-5 micron sized iron powder particles are used. The iron powders are dispersed in RTV silicone with respect to different volume fractions. The RTV silicone and the iron powders are mixed for 10 minutes to achieve even dispersion with the mixer. Due to the catalyst which accelerates the rate of chemical reactions, there is a tendency for bubble formation in the mixture. In order to increase the integrity of MRE material, pores are pulled out in a vacuum chamber which is connected to air pressure pump. Vacuuming is processed until gas evaporation is finished as shown in Fig. 4.2.

In order to investigate the MR effect of four different curing times, identical materials must be manufactured at the same time. Thus, the mixture is poured into four prepared aluminum moulds as can be seen in Fig. 4.3. In order to make the specimen precise and to take it off from the mould easily, each aluminum mould consists of base mould, two side pieces, three long plates and lids to cover the mould. The curing process is conducted under a permanent magnet at room temperature with different curing times.

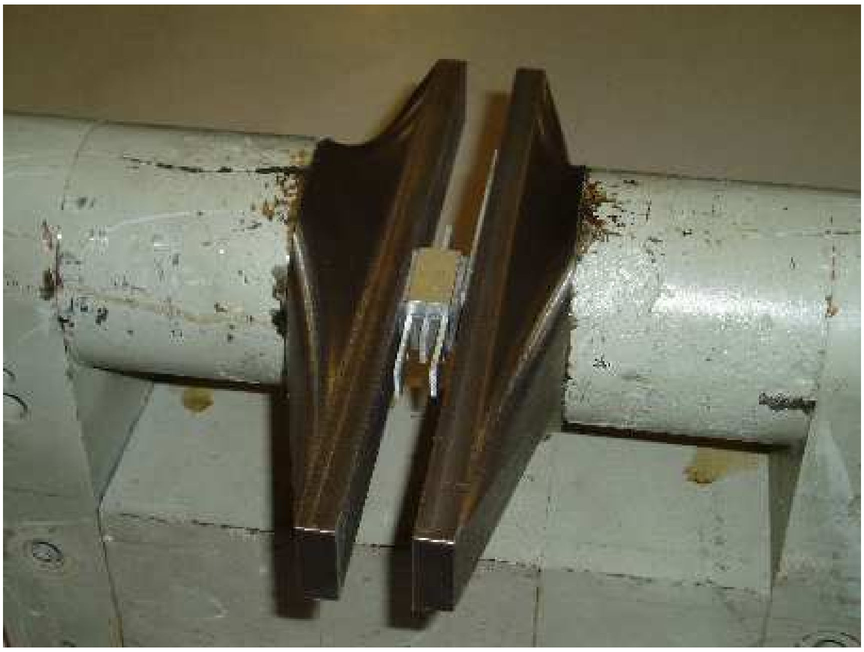

Figure 4.4: Curing specimen placed between two magnetic guiders attached permanent magnet to get magnetization effect

Fig. 4.4 shows two long magnetic guiders made of cast iron fitted at the end of each permanent magnetic pole in order to distribute the magnetic field evenly and to reduce the air gap between the two magnetic poles. The surface area of the magnetic guider transferring 0.3T of the magnetic field is 230×20 mm^2 which can cure a number of specimens at the same time. This curing process is conducted for a variety of time intervals in order to assess its effect on properties.

Table 4.3 shows the curing time of RTV silicone provided by Wacker Co. (Wacker-Silicones, 2005) in terms of different temperature ranges. Therefore, the iron particles are suspended before RTV silicone is fully cured and then, the iron particles are locked in their position when the curing process of silicone is completed. In this study, several specimens are prepared with respect to the different curing times: 1hr, 2hrs, 4hrs, 24hrs, 48hrs, 72hrs and 96hrs under the same magnetic field and room temperatures.

Table 4.3: The curing times of RTV silicone (Elastosil M4644) corresponding to a layer thickness of 1 cm (Wacker-Silicones, 2005)

Curing temperature	*Curing time*
$23°C$	15 hrs
$35°C$	4 hrs
$60°C$	2 hrs
$70°C$	30 min
$100°C$	15 min
$150°C$	5 min

4.5 Microscopy

The purpose of the microscopy is to understand the alignment behaviour of iron particles in terms of various curing times under a magnetic field. For this investigation, 30 vol% of aligned MRE specimens are examined. Two specimens are fabricated as described in the previous section. Aligned MRE before cured (1hr) and that after cured (24hrs) under a magnetic field are prepared. In order to investigate the distributions of particles and the difference in alignment of iron particles, specimens are cut parallel to the direction of alignment of particles. The surfaces of the fabricated MRE samples are examined using a scanning electron microscope (SEM). What we envisage seeing in the microscopy is how different alignment of MREs can achieve better performance, which has not been found in literature.

4.6 Experimental Results

4.6.1 Fractrographic / microscopy examination

The alignment of iron particles suspended in elastomer with respect to the different curing times without and under a magnetic field can be seen in Fig. 4.5. The alignment of 3-10 μm sized iron particles within dotted line is achieved at 0.3T magnetic field the during curing process. Once the iron particles are aligned and locked in the elastomer, their position does not change in the curing process. Interestingly noting that there are no significant changes in the alignment of particles even if the curing time is excessively different. This indicates that alignment occurs fairly early in the curing process. However, the magnetisation effect should be investigated by other tests in order to find out differences of property which can not be seen in microscopy only.

4.6.2 Test results and analysis

Effect of curing time

In order to investigate the magnetisation effect on iron particles in MRE, dynamic shear property test with different curing stages under a magnetic fields is carried out. Fig. 4.6 shows the shear modulus changes, difference between shear modulus under magnetic field and the zero-field shear modulus, with respect to the different curing times, e.g. 1hr, 2hrs, 4hrs and 24hrs, and for varying volume of iron particles (i.e. 20, 25, 30 and 35vol%). As the curing time under magnetic field increases, shear modulus change increases. The highest shear modulus change is shown to be for 24hrs cured MRE. From Fig. 4.6 it is clear that there is a general trend of increasing modulus with increasing cure time. However, a similarly consistent trend in increase in modulus with a larger volume fraction of iron particles is not present. Peak values of modulus, for all samples cured for up to 24 hours, are always observed in sample with 30% volume fraction of iron particles.

Fig. 4.7a and b show the effect on shear modulus and damping changes for varying times of curing, e.g. no curing, 24hrs, 48hrs, 72hrs and 96hrs (at levels much higher than shown in Fig. 4.6) and at different frequencies (up to 30Hz). The ordinates in both cases refer to the ratio of the stiffness / damping value in each case as a proportion of the respective values under no magnetic field. From Fig. 4.7a it is evident that, apart from small variations especially in the 1 to 5 Hz range, shear modulus change is fairly constant at all frequencies. It is also clear that samples cured for 24 hrs and 48 hrs exhibit higher stiffness than samples cured for longer periods. As expected, samples with no curing show the lowest values. Damping change is shown to be independent of frequency ranges except

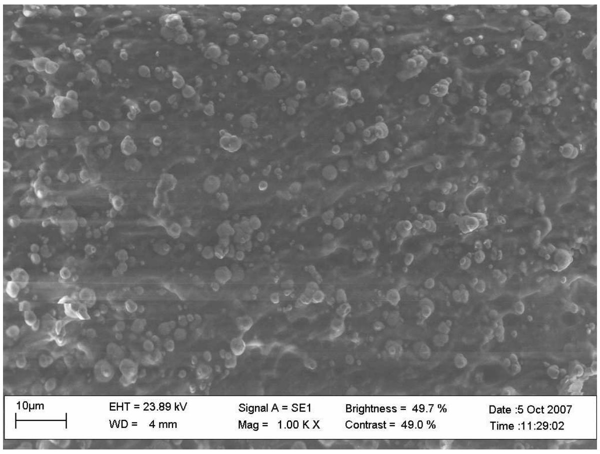

(a) Cured MRE without magnetic field

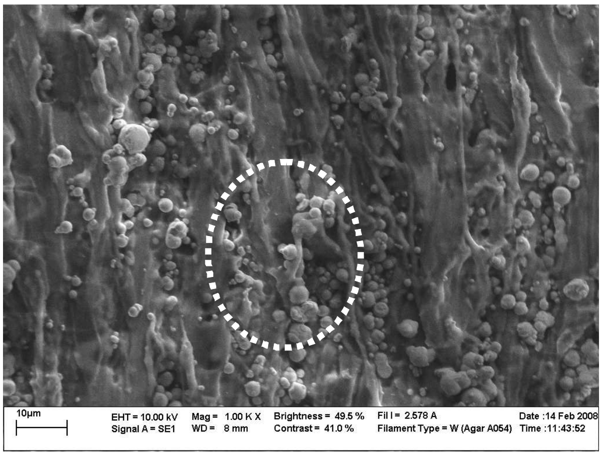

(b) 1hr cured MRE

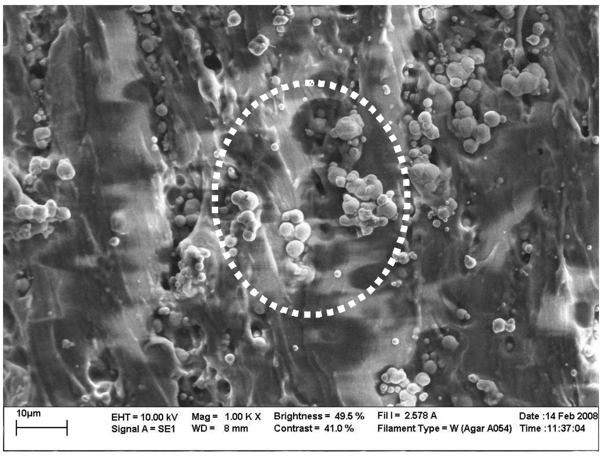

(c) 24hrs cured MRE

Figure 4.5: SEM images of MRE with different curing time under the magnetic field (Iron particles within dotted line area)

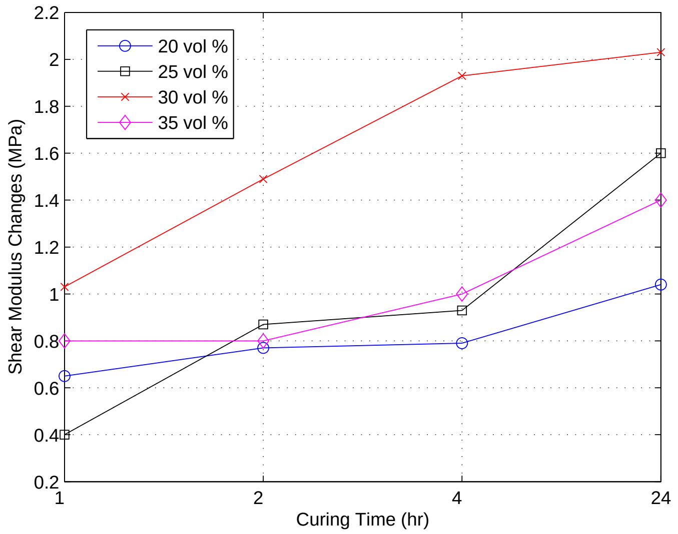

(a) Absolute change

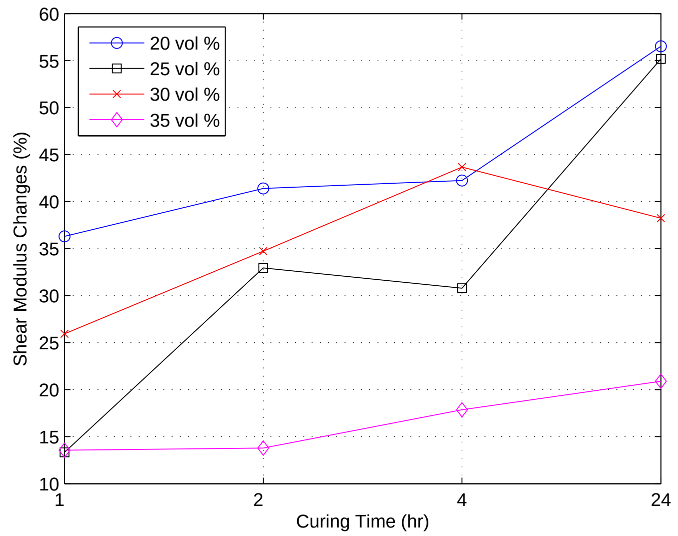

(b) Relative change

Figure 4.6: Shear modulus change of MRE in terms of curing time under magnetic field. This data corresponds to the 0.3% strain at 10Hz and 0.3T

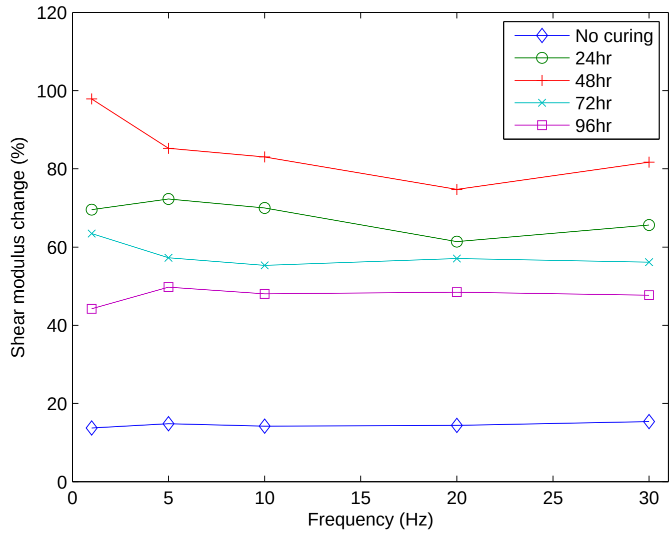

(a) Shear property changes

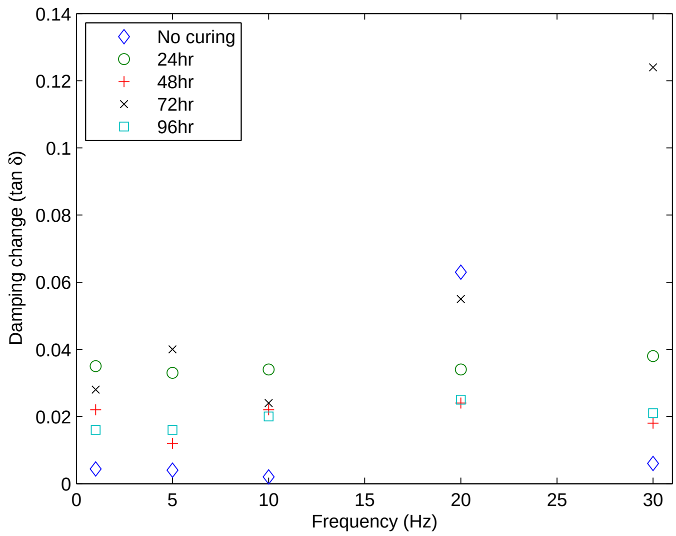

(b) Damping changes

Figure 4.7: Shear modulus change and damping in terms of frequency ranges. This data corresponds to 27 vol% of iron particles and the 0.1% strain at 0.47 T

the samples cured for 24 hrs, 48 hrs and 96 hrs, see Fig. 4.7b. Error bound may occur due to the limit number of samples.

Effect of volume change

The shear modulus changes in relation to various volume fractions of iron particles (i.e. 20, 25, 27, 30, 35 and 40vol%) are shown in Fig. 4.8. All specimens are cured for 24hrs under a magnetic field. The maximum absolute shear modulus change of 30 vol% MRE is about 1.8 MPa as shown in Fig. 4.8a, whereas the relative shear modulus change of 27 vol% MRE is about 55% as shown in Fig. 4.8b. These results show good agreement with the results of Davis (1998).

Effect of pores

Once RTV silicone is mixed with a catalyst, there is likelihood of the occurrence of macro or micro scaled pores. In order to determine the effects of such pores, two samples are compared, one of MRE with pores and the other of a vacuumed MRE with pores removed. The comparisons are shown in Fig. 4.9. Both specimens are cured at room temperature without magnetic field. It is evident from the trends that removing the pores does have a significant impact on both shear modulus and tanδ values. As seen before, the shear modulus in both instances remains largely frequency independent. The tanδ value though, as expected, shows variance with frequency.

This indicates that pores make the non-magnetic matrix softer and allow iron particles to have more dipole moment while the silicone medium allows those to have less dipole moment. The results also show that the change of shear property is independent of frequency ranges.

Effect of strain ranges

Dynamic shear property tests are carried out with different shear strain ranges from 0.3% to 10%. Fig. 4.10 shows that the shear modulus change is likely to be

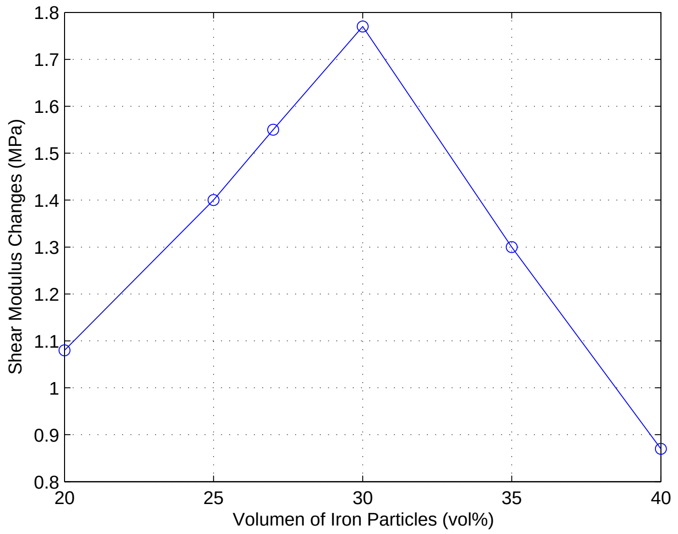

(a) Absolute change

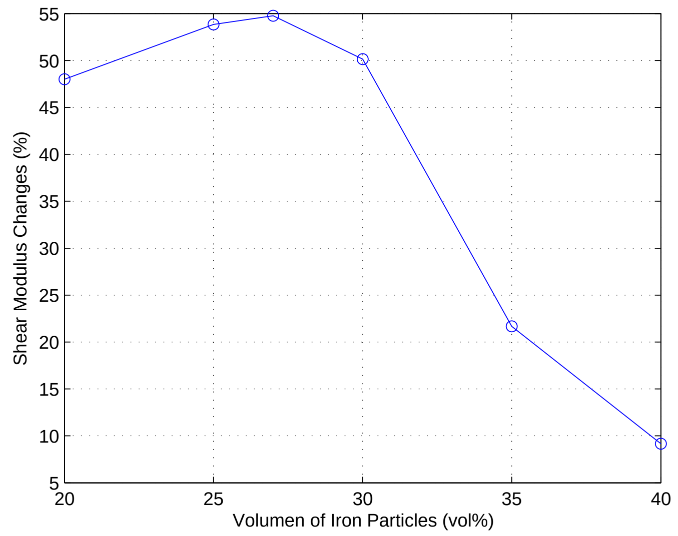

(b) Relative change

Figure 4.8: Shear modulus change in terms of volume change. This data corresponds to the 0.3% strain at 1Hz and 0.3T; 24hrs curing time.

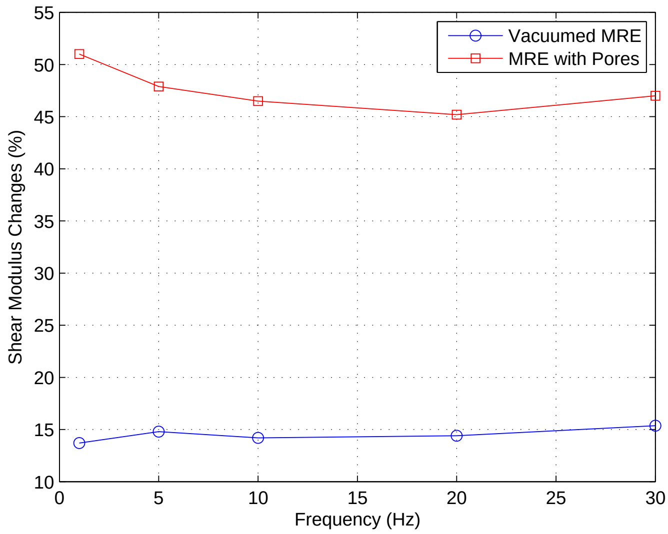

(a) Shear modulus changes

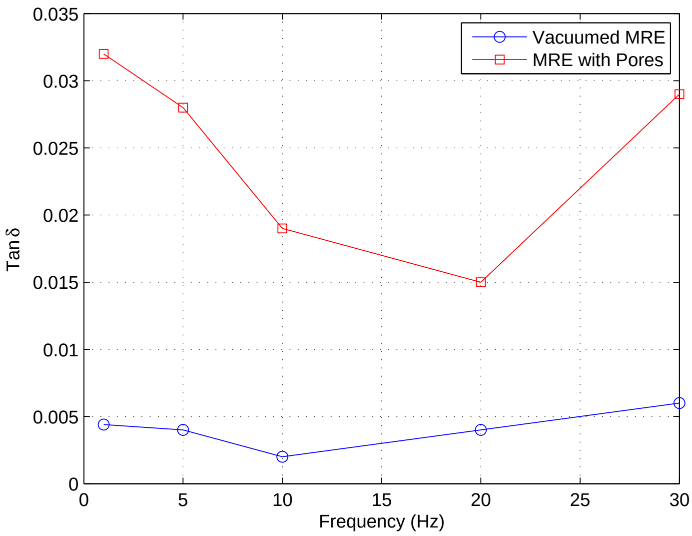

(b) Damping changes

Figure 4.9: Shear modulus change of MRE in terms of pores effect. This data corresponds to the 1% strain under 0.47T of magnetic field

high as the applied strain becomes small, i.e. the Fletcher-Gent effect (Fletcher & Gent, 1953). The yielding is significant as shown by a pronounced drop off in the rheological effect (Fig. 4.10a) and an increase in field dependent energy dissipation (Fig. 4.10b). It is worth noting that the change in loss factor is also dependent on strain ranges. The loss modulus change shows a maximum value in the region of about 10% strain where the storage modulus decreases. Since shear properties of MRE change dominantly in small strain ranges, MRE is shown as being suitable as a core material in sandwich beam to achieve adjustable stiffness.

Hysteresis of MRE

Fig. 4.11 shows material hysteresis curves for the specimen. In Fig. 4.11a, the hysteresis curve indicates that MRE cured at room temperature is shown with small amount of stiffness changes as well as damping. Large damping effects can be seen as the magnetic field increases, for 48 hrs curing MRE as shown in Fig. 4.11b. This is because aligned MRE shows high stiffness change as well as damping effect caused by high frictional forces among particles.

4.7 Conclusion

Dynamic MRE performances in terms of curing time, strain range and porous effect under different magnetic field strength are investigated. It is shown that MRE samples cured for 24 hrs and 48 hrs under magnetic field exhibit higher stiffness than samples cured for longer periods. Large hysteresis effect of MRE indicates that cured sample under magnetic field shows improved damping effect than sample cured room temperature only. It is worth noting that the change in loss factor is also dependent on strain ranges. The overall performance (stiffness and damping changes) of porous MRE is found to be better than that of denser MRE, since the magnetic forces create larger displacements within the matrix of MRE with pores. However the porous effect may result in poor integrity of material. With a controlled introduction of pores during manufacture, elastomers with a good MR

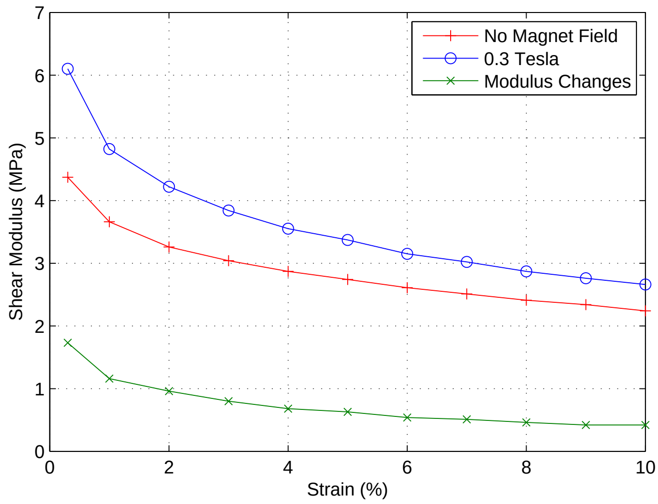

(a) Shear modulus changes

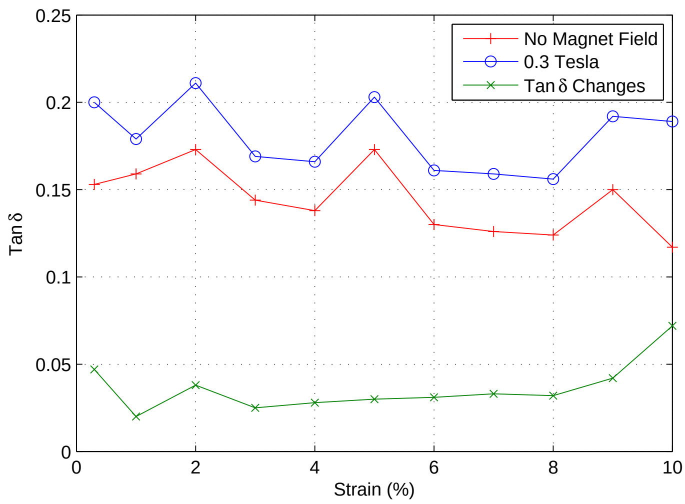

(b) Damping changes (tan δ)

Figure 4.10: Shear modulus change of 27 vol% of MRE in terms of different strain ranges. This data corresponds to the 24hrs cured MRE at 30Hz

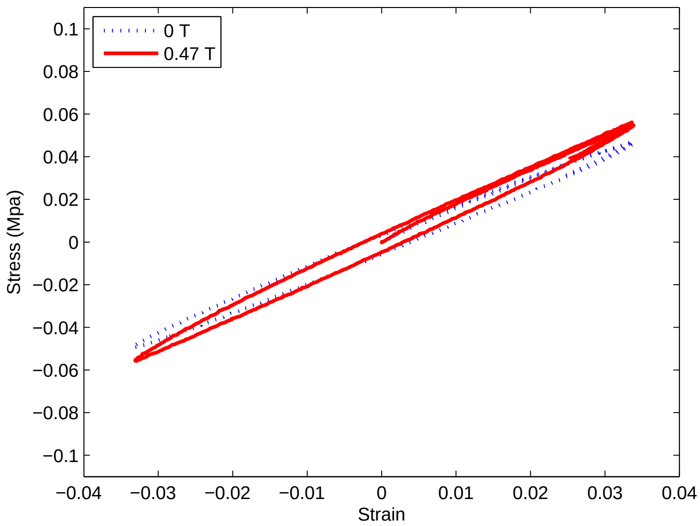

(a) MRE cured at room temperature only

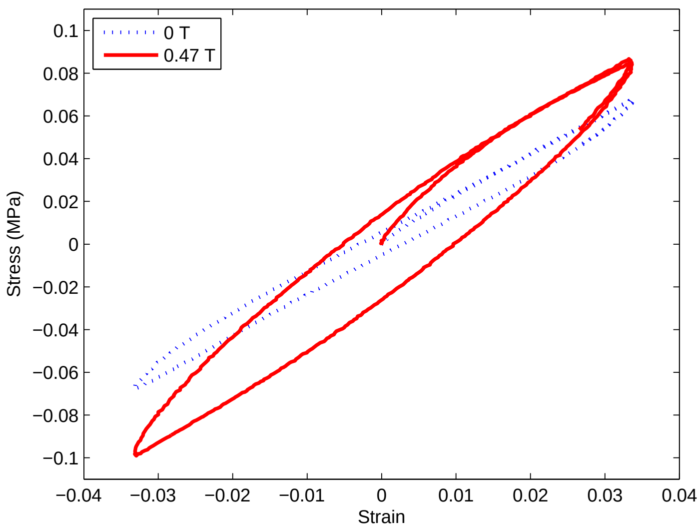

(b) MRE cured under magnetic field for 48 hrs

Figure 4.11: Shear modulus change of 27 vol% of MRE in terms of different curing time. The set up amplitude is 0.2 mm and the strain rate is 1.0 mm/min.

effect may be developed.

This leads to the conclusion that despite the same combination of iron particles and elastomers, the characteristics of MRE can be different owing to variations in the curing time and volume fraction of pores.

Chapter 5

Theoretical and Numerical Assessment of Shear Property for MRE

5.1 Introduction

The test results from the previous chapter need to be better understood by theoretical and numerical predictions. To this end, theoretical model with magnetisation effect on iron particles is presented to obtain proper curing time. In addition to this, macro scale modelling skill for rubber like nonlinear behaving materials by adopting FEA analysis suggest the optimum volume of pores and size of iron particles to enhance the performance of MREs.

5.2 Theoretical Formulation of the MRE in terms of Magnetization

A theoretical study is conducted to better understand magnetisation effect on MRE. The overall magnetic energy density (energy per unit volume) for an MRE elastomer can be expressed as follows,

$$U_{MRE} = U_{host} + U_{mag} \tag{5.1}$$

where U_{host} and U_{mag} represent the strain energy density of the host elastomer and that of magnetically induced elastomer. The strain energy density U_{host} of the host elastomer can be expressed using the Ogden strain potential (Davis, 1998) as,

$$U_{host} = \sum_{x=1}^{3} \frac{2\nu_x}{\alpha_x^2}(\lambda_1^{\alpha_x} + \lambda_2^{\alpha_x} + \lambda_3^{\alpha_x} - 3) \tag{5.2}$$

where λ_x (x=1, 2, 3) represents the principal extension ratio and ν_x and α_x are uni-axial stress-strain parameters. For an incompressible material the principal extensions are $\lambda_1\lambda_2\lambda_3 = 1$. The nominal stress in the elastomer can be defined as follows,

$$\sigma_{host} = \left(\frac{\partial U_{host}}{\partial \lambda_x}\right). \tag{5.3}$$

The magnetically induced energy density of the elastomer (U_{mag}) is given as (Abramchuk *et al.* , 2007),

$$U_{mag} = \mu_0 M(H) \cdot H \tag{5.4}$$

where $M(H)$ denotes the magnetisation curve, μ_0 the magnetic permeability of a vacuum ($4\pi \times 10^{-7}$ H/m) and H stands for the magnetic field strength. The total shear modulus of MRE (G) can be described as follows (Varga *et al.* , 2006),

$$G = G_{host} + G_{mag}, \tag{5.5}$$

where G_{host} is the shear modulus of host elastomer by the following alternative expression in the small strain ranges (Abramchuk *et al.* , 2007)

$$G_{host} = \frac{1}{3} \lim_{\lambda_x \to 1} \left(\frac{\partial^2 U_{host}}{\partial \lambda_x^2} \right), \tag{5.6}$$

and G_{mag} is the magnetically induced modulus.

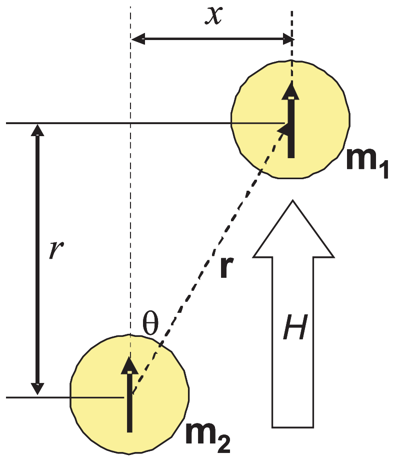

Figure 5.1: Magnetic interaction caused by dipole moments (Jolly *et al.* , 1996b)

The magnetic interaction caused by the dipole moments is shown in Fig. 5.1. For iron particles, Rosensweig (1985) introduced the interaction energy of these two point dipoles as,

$$W = \frac{1}{4\pi\mu_0\mu_1} \left[\frac{\mathbf{m}_1 \cdot \mathbf{m}_2}{r^3} - \frac{3}{r^5} (\mathbf{m}_1 \cdot \mathbf{r})(\mathbf{m}_2 \cdot \mathbf{r}) \right], \tag{5.7}$$

where μ_1 is the relative permeability of MRE and r is the distance between the particles. When the two iron particles are aligned along the magnetic field direction and contacted with each other (r $\cong$ 0), W can be expressed by,

$$W = \frac{\mathbf{m}_1 \cdot \mathbf{m}_2}{4\pi\mu_0\mu_1 r^3}. \tag{5.8}$$

For a dipole *i*, the dipole moment of spherical shape of each iron particle $\mathbf{m}_i$ can be expressed as (Davis, 1998)

$$\mathbf{m}_i = \frac{4\pi}{3} R_i^3 M_p \mathbf{e}_z, \tag{5.9}$$

where R_i is the radius of each particle, M_p is the average particle polarization and $\mathbf{e}_z$ is a unit vector in z direction, that is, the magnetization points along the applied magnetic field everywhere. Then, the total energy density can be evaluated and the stress induced by the application of a magnetic field can be derived by taking the derivative of inter-particle energy density in terms of the shear strain. The magnetically pre-yield shear modulus G_{mag} of the particle can then be expressed as (Jolly *et al.* , 1999),

$$G_{mag} \cong \frac{4\phi M_p^2}{\mu_1 \mu_0 h^3}, \qquad \epsilon < 0.1 \tag{5.10}$$

where h is defined as r/R which is the gap between particles in a chain where r is the distance between the origin of each particle and R is the radius of each particle respectively. When the iron particles are aligned and locked into the nonmagnetic medium during cross-linking, the distance between each particle becomes small. The magnetisation-time curve can be expressed as (Ausanio *et al.* , 2002),

$$M_p(t) = M_i + (M_r - M_i)(1 - e^{-t/\tau}) \tag{5.11}$$

where τ is the time constant varied by temperature, M_i and M_r are the values of the induced and regime magnetisations in Eq. 5.11, respectively. When the term of magnetisation is included, the total shear modulus can be expressed as,

$$G \cong G_{host}(1 + \beta t^2) + \frac{4\phi[M_i + (M_r - M_i)(1 - e^{-t/\tau})]^2}{\mu_1 \mu_0 h^3} \tag{5.12}$$

where β is a curve fitting constant corresponding to the initial shear property of MRE. This constant can be decided by magnetisation of MRE in terms of curing time under a magnetic field based on experiment.

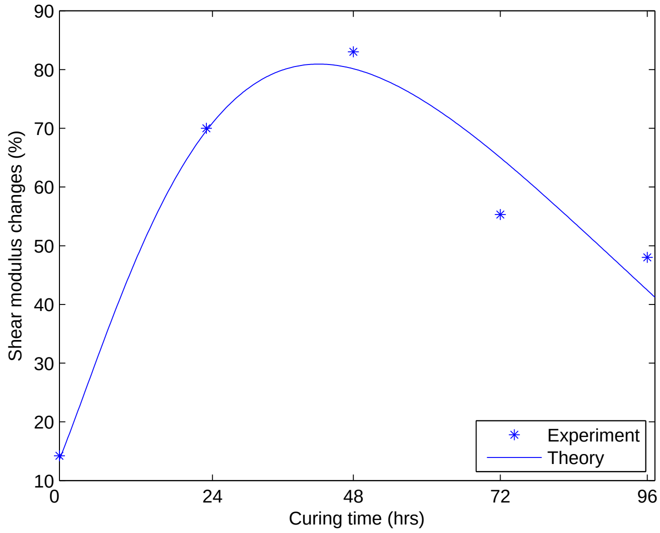

Figure 5.2: Comparison of shear property changes between theory and test results in terms of curing time. Corresponding frequency for the experiments is 10Hz and α is 4.3e-12 for the theoretical prediction, 27 vol% of MRE

The comparison of shear property changes between the theoretical prediction (Eq. 5.12) and the test results in terms of curing time under magnetic field is shown in Fig. 5.2. The theoretical prediction of shear modulus change shows good agreement with experimental results until the maximum value of shear modulus changes. The figure reveals the trend, in both theoretical prediction and empirical values, of increasing change in modulus until a curing time of 48 hours before decreasing with further cure under magnetisation.

5.3 Numerical Analysis

5.3.1 Finite element discretization

From previous test results, it was shown that the characteristics of MRE are dependent on curing time, volume fraction of iron particles and pore distribution. The purpose of the numerical analysis is to understand how the volume fraction of the pores and how the size of iron particles affect to MRE behaviour. Therefore, a quasi-static micro-scale analysis was carried out using finite element (FE) software, ABAQUS/Explicit (ABAQUS, 2007).

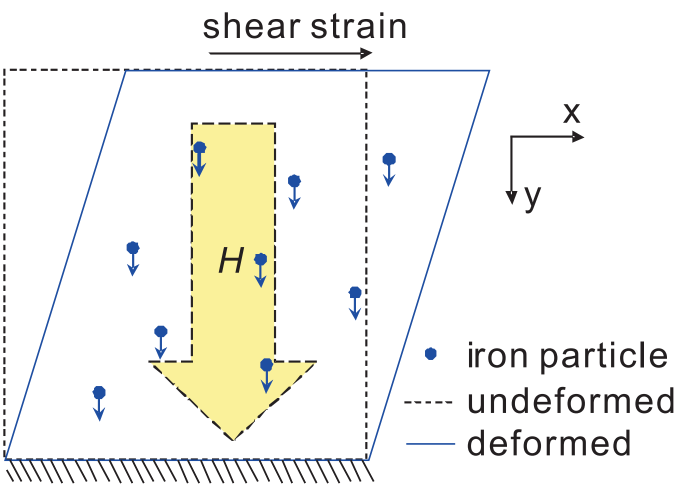

Figure 5.3: Schematic model of MRE specimen

In order to do this, a simplified numerical model is used. Fig. 5.3 shows the schematic idea of the simplified model. The solid line represents deformed MRE after the shear strain is applied at the top of the undeformed MRE which is shown by the dotted line. For finite element meshes, a random number of elements of pores and iron particles is generated with the aid of Matlab. ABAQUS linear quadrilateral reduced integration elements, four node plain stress continuum elements (CPS4R), were used to mesh the model. The Hyperfoam model based on the experimental stress-strain data is inherent in elements. Curve fitting algorithm is used to fit a strain energy function to the input test data. Each span of square model is 1mm and thickness is 10μm. The two dimensional square model consists of 100 by 100 elements. For boundary conditions, nodes at bottom are fixed whereas other nodes are free. Shear strain is subjected by applying 1% change of displacement in x-direction to each node on top of the elements while inertial identical acceleration loads in y-direction are applied to the element of each iron particle.

Table 5.1: Material properties of iron particles and an unfilled elastomer

	$Young's\ Modulus$ $E(GPa)$	$Poisson's\ ratio$	$Density$ (kg/m^3)
Iron particles	210	0.3	7500
Unfilled Elastomer (ABAQUS)			
$Uniaxial\ test\ data$		$Simple\ shear\ test\ data$	
$Stress\ (MPa)$	$Strain$	$Stress\ (MPa)$	$Strain$
-0.0217	-0.05	0.0107	0.08
-0.0367	-0.15	0.0373	0.16
-0.0433	-0.25	0.0533	0.24
-0.0504	-0.35	0.0853	0.32
-0.0604	-0.45	0.1280	0.40
-0.0759	-0.55	0.1653	0.48
-0.1083	-0.65	0.2080	0.56
-0.1933	-0.75	0.2560	0.64
-0.2896	-0.80	0.2987	0.72

Elements of carbonyl iron particles show elastic behaviour. The property of iron particles and elastomer comprising MRE are shown in Table 5.1. Based on uniaxial and simple shear test data of unfilled elastomer provided by ABAQUS, hyperelastic characteristic of elastomer elements were taken into account.

The generation and distribution of the elements is constructed on the following assumptions,

- The specimen is rectangular and the unit size of iron particles and the pores are uniform;
- The void elements are considered for the pores;
- An inertial acceleration (a/a_{sat}) applied to each iron particle element is regarded as a magnetic force, where (a_{sat}) is saturated acceleration;

- Owing to the preceding statement, the magnetic repulsion or attraction forces between two magnetic dipoles are not considered.

Parametric studies with respect to the volume fraction of pores and particle size are carried out. Different combinations between iron particles and pores distributed in MRE are compared. Numerical calculation with one fully dense (without pores) specimen and three different volume fraction of porous MRE specimens are performed. For porous MRE, the volume percentages of pores are 5%, 7%, and 9% respectively. Undeformed isometric views of meshes for MRE specimen are shown in Fig. 5.4. The 20vol% of iron particles are sorted in an ascending order of whole number of elements after the random numbers are generated. And then, the rest of volume fractions of pores are sorted in the same manner. The generated numbers are then used for each FE model.

5.3.2 Results and discussions

Fig. 5.5 shows the stress distribution spectra of deformed MRE elements under a magnetic field. The light gray corresponds to a low value of the stress while the dark gray represents a high value of the stress. The void elements in white represent the pores. Inertia acceleration is applied on each iron particle element while 1% shear strain is subjected on the top of the specimen. Most of maximum stresses arise in the vicinity of the top and the bottom faces of the elements. As the volume fraction of the pores increases, larger element distortion and a higher stress variability is seen. This indicates that the change of stress is slightly higher for the elastomer containing a larger volume fraction of pores. This is attributed to the shear stiffness being initially low caused by pores contained within MRE.

The results of the shear strain-stress in terms of volume fraction of pores are shown in Fig. 5.6. As the fraction of pores increases, the shear modulus of the element decreases. Linear behaviour of the curves is noticed when there is no inertial acceleration on the particles, see Fig. 5.6a. Compared to the results when no magnetic field is applied, the curves under a saturated magnetic field show

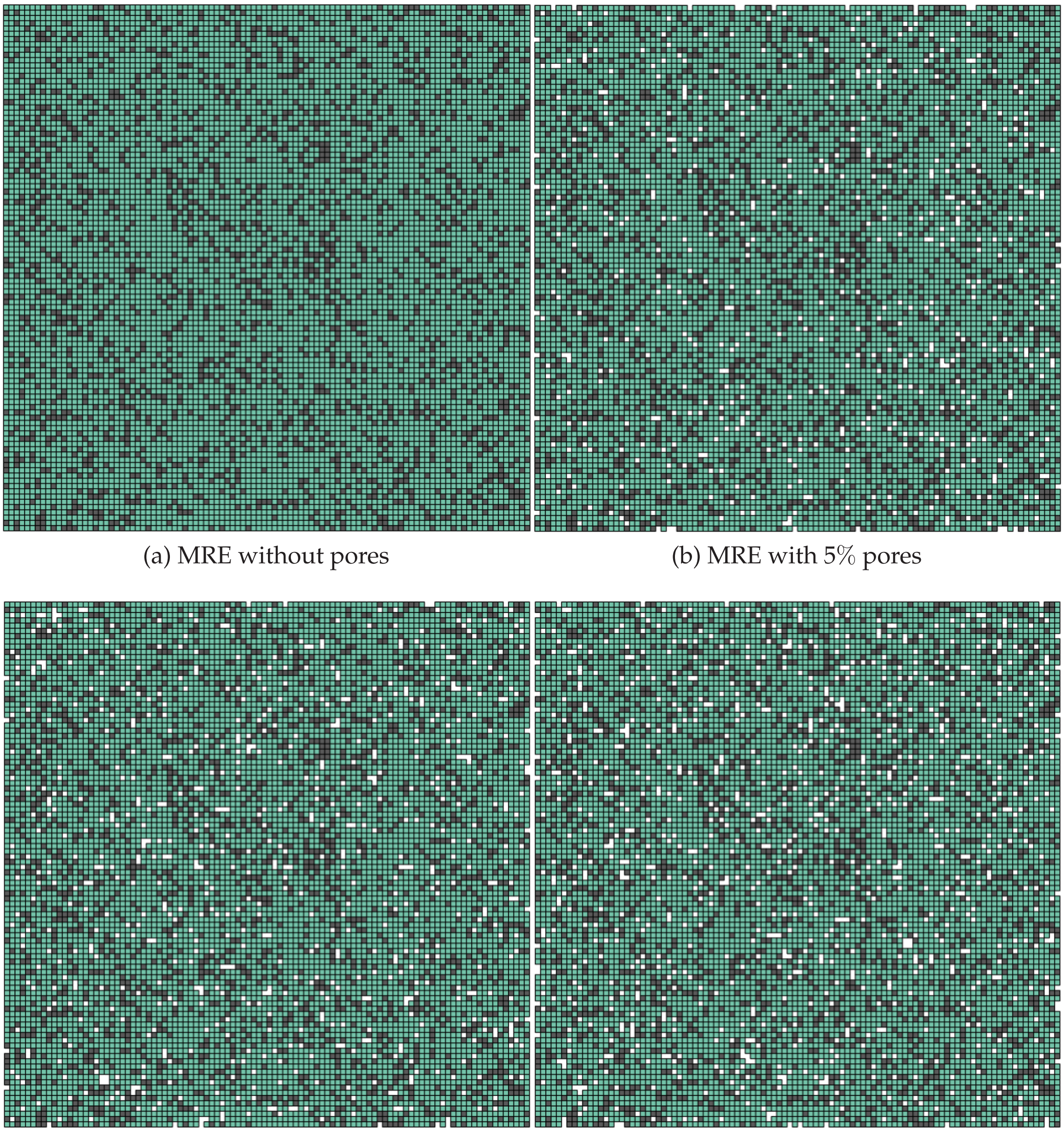

(a) MRE without pores

(b) MRE with 5% pores

(c) MRE with 7% pores

(d) MRE with 9% pores

Figure 5.4: Micro-scaled undeformed MRE specimen (Green: elastomer, Black: iron particles, White: pores)

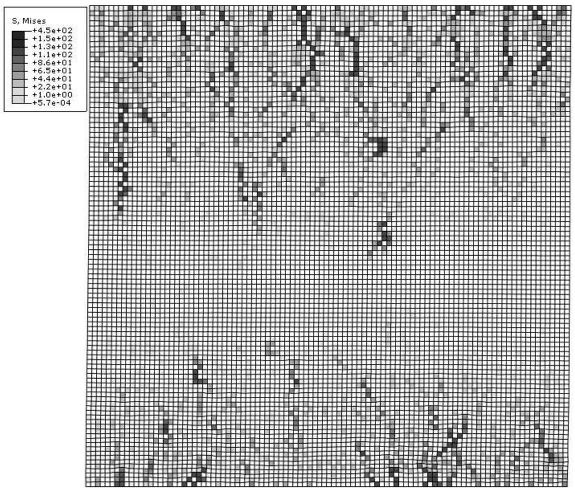

(a) MRE without pores

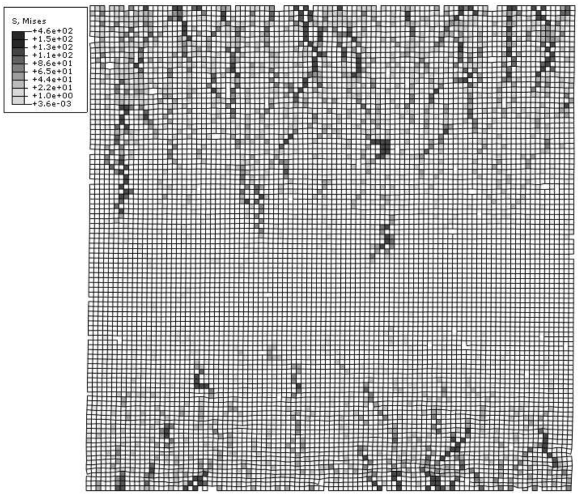

(b) MRE with 5% pores

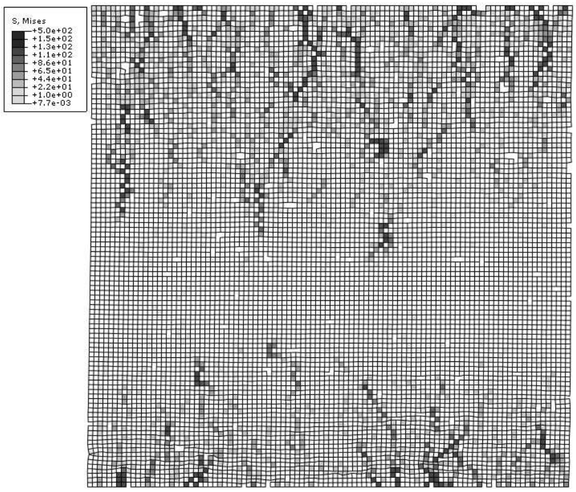

(c) MRE with 7% pores

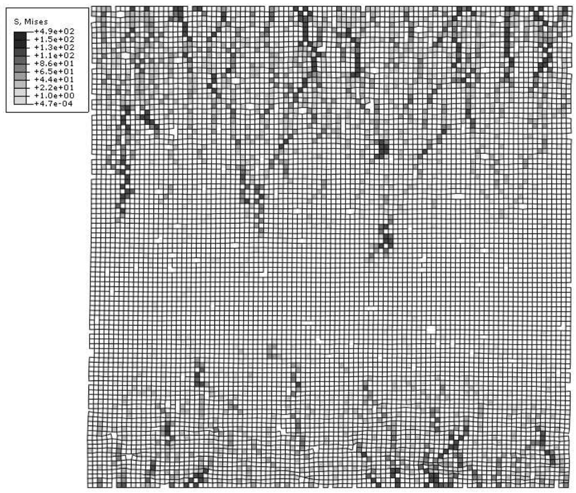

(d) MRE with 9% pores

Figure 5.5: Stress distributions of micro-scaled deformed MRE specimen at magnetic saturation when 1% strain is applied (White: pores)

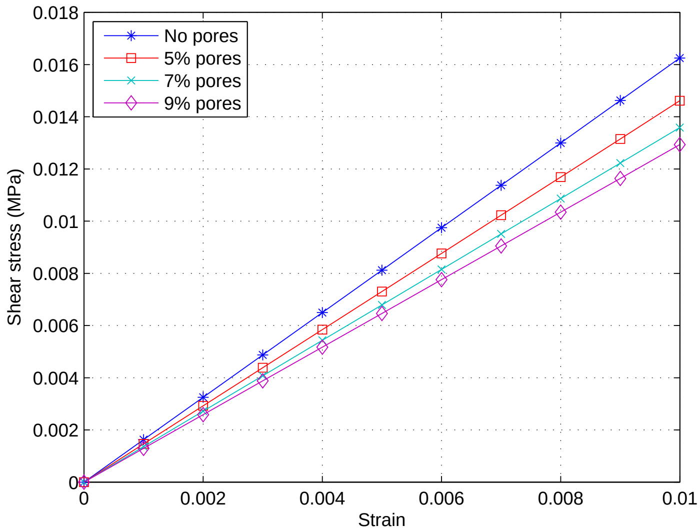

(a) No magnetic field

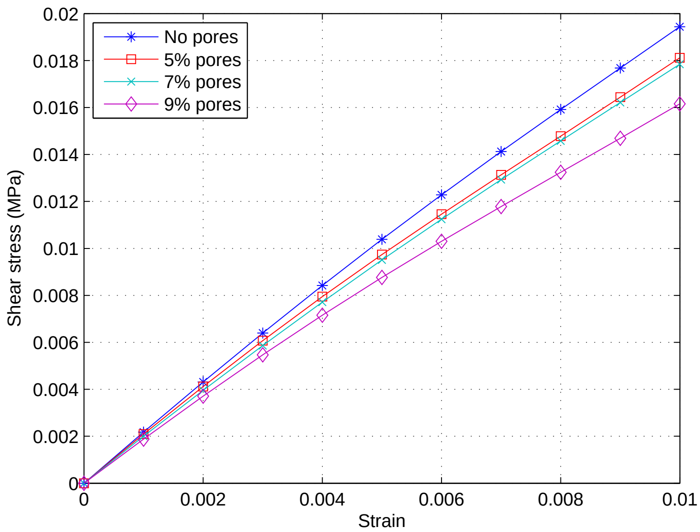

(b) Saturated magnetic field

Figure 5.6: Shear stress versus shear strain in terms of volume fraction of pores in MRE (a/a_{sat}=1)

more hysteretic behaviour, see Fig. 5.6b. This phenomenon appears to agree with the trends of the hysteretic behaviour in the experimental results shown in Fig. 4.11. More hysteretic behaviour occurs at 9 vol% porous elements. This is due to the damping effect from interfaces among elastomeric elements and iron particles when large inertial forces generated owing to the applied magnetic field.

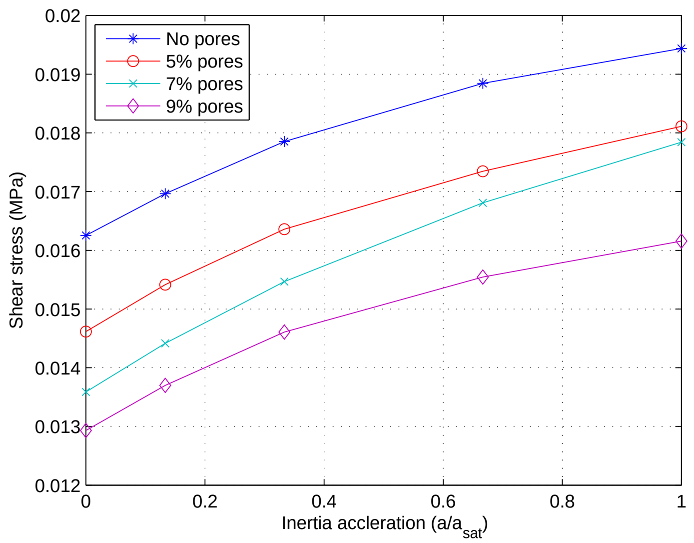

(a) Absolute changes

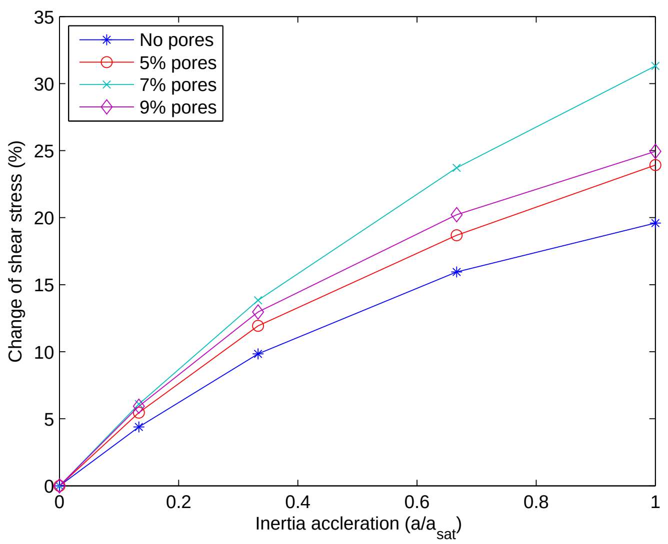

(b) Relative changes

Figure 5.7: Shear stress versus magnetic field corresponding 0.01 strain

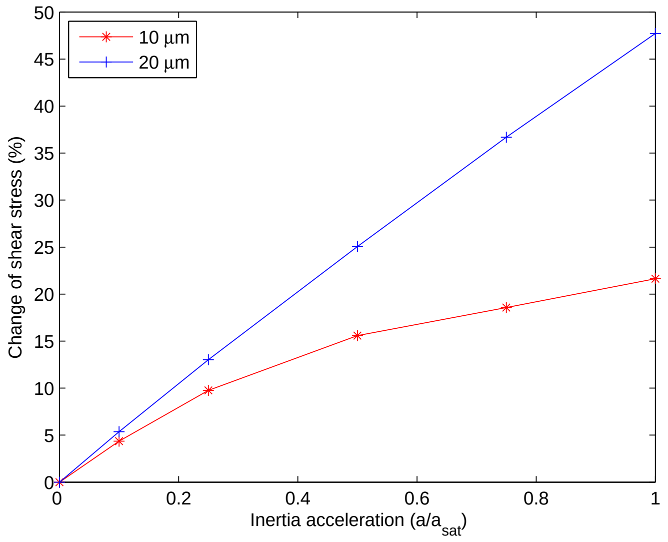

Figure 5.8: Shear force change in terms of size of the iron particles (1% strain)

The variation of shear force with respect to magnetic field can be seen in Fig. 5.7. A non-dimensional inertial acceleration is applied to each iron particle. As the volume of pores increases, the stiffness was found to decrease, see Fig. 5.7a. The relative change was the greatest for porous elements with initial low stiffness values, see Fig. 5.7b. A significant effect of the shear property changes is shown at 7 vol% of MRE. For more porous MRE, the overall deformation increases since the inertia forces produced allows large displacements within the MRE matrix.

MRE performance may show different behaviour in terms of the size of iron particles. FE analysis with different size of iron particles elements is carried out; 10μm and 20μm iron particles are meshed. The volume fraction of iron particles used in both models is 20 vol%. Boundary conditions and load applied to iron particles are same as previous models. The results are also seen in Fig. 5.8. When the magnetic field increases, the stiffness of MRE with 20μm iron particles are higher than that with 10μm. As can be seen in these figures, MRE element with large sized particles elements shows a large MR effect. This numerical result is supported by the experimental result of Lokander & Stenberg (2003). However hysteretic behaviour is seen at small sized iron particles rather than at large sized iron particles.

This indicates that small iron particles may induce more energy dissipation within elastomer than large iron particles.

Overall, it is worth noting that new approach of macro-scale FEA analysis can assess the property of non-linear behaving MR elastomers, which can not be achieved without repeatable tests.

5.4 Conclusion

The enhanced theoretical model with magnetisation effect on iron particles is presented to achieve proper curing time. In parallel to this, the new macro scale modelling skill for rubber like nonlinear behaving materials by adopting FEA analysis is presented to obtain the optimum volume of pores and size of iron particles to enhance the performance of MREs.

Good agreement between the experimental results and the theoretical prediction including the magnetisation effect on MRE is found. From macro scaled numerical simulations, change of shear modulus is found to increase with an increase in the volume fraction of pores. Numerical results also show that the size of iron particles within MRE materials influences MR performance: as the size of iron particles decreases, lower stiffness and higher hysteretic behaviour is observed.

This leads to the conclusion that despite the same combination of iron particles and elastomers, the characteristics of MRE can be different owing to variations in the size of iron particles, curing time and volume fraction of pores.

Chapter 6

Forced Vibration Test for MRE Embedded Sandwich Beam

6.1 Introduction

Experimental, theoretical and numerical studies on MRE have been carried out in previous chapters in order to enhance the MRE material performance only. Since MREs can be adapted to smart structures as a part of adjustable materials, it is essential to take into account tests for the MRE configured structure. Due to the sparse knowledge on the dynamic structral behaviours of MRE cofigured structures, forced vibration tests for MRE cored sandwich beam are investigated.

6.2 MRE Cored Sandwich Beam

MR material has been used to carry out vibration analysis to observe vibration responses in real time and vibration suppression capabilities of three layered MR adaptive sandwich beams (Sun *et al.* , 2003; Yalcintas & Dai, 2004). It was shown that the vibration minimization capabilities of MR adaptive structures are significant. The development of MRE based adaptive structure was initiated only very recently. Zhou & Wang (2005) carried out theoretical study on MRE embedded smart sandwich beams with non-conductive skins based on higher order sandwich panel theory. However, the damping effect of the sandwich beam has not been investigated. Demchuk & Kuz'min (2002) measured the elastic modulus and loss factor using clamped vibrating sandwich beam.

Key limitations in the current literature are as follows,

- A relatively thick layer of MRE core embedded in a sandwich beam has not been considered so far.
- There has been a limit of applying a magnetic field through a beam's height.
- Boundary effect has not been considered.
- Localised magnetic field effect has not been considered.

The aim of this study therefore is to address these limitations and to investigate the damping effect of an MRE adapted sandwich beam in terms of various combination of magnetic field strength. To this end, a forced vibration test rig has been developed, which allows application of a magnetic field through the height of the beam.

6.3 Preparation of The Specimens and Experimental Setup

The experimental study is carried out to illustrate the control capabilities of MRE adaptive sandwich structures in real time, and to assess the dependence of frequency response and the damping upon a magnetic field.

The MRE core specimens are made of room temperature vulcanizing (RTV) silicone (Elastosil M4644, Wacker Co.) including catalyst and 3-5 micron sized iron powder particles (CIP CC, BASF). The amount of iron particles is 30 vol %. The first step is to mix iron powders with RTV silicone for 10 minutes to achieve even dispersion and then air bubbles are pulled out in a vacuum chamber as described in Chapter 4. After pouring the mixture into an aluminium mould, the curing process is conducted between two permanent magnetic poles for 24 hours in order to increase MRE performance as shown in Fig. 6.1. Two magnetic distributors attached to both ends of permanent magnet are made of a cast iron in order to

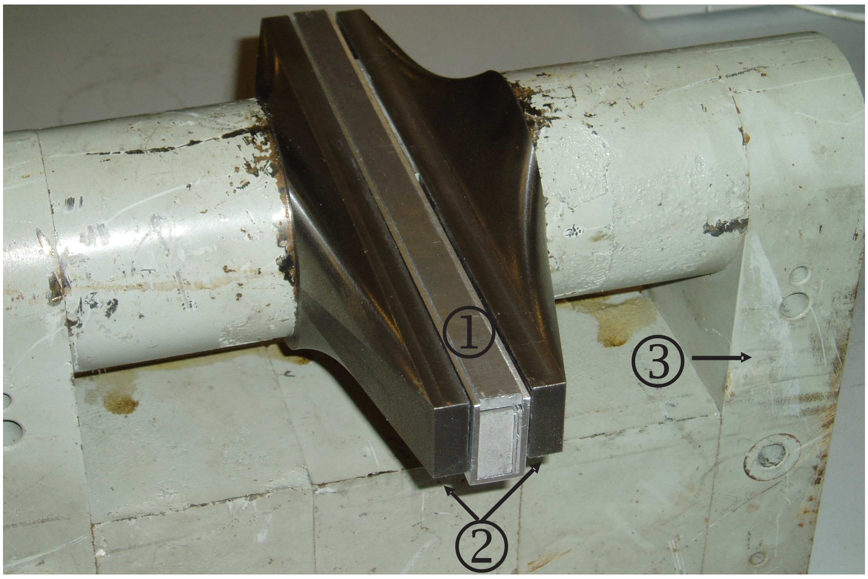

Figure 6.1: Curing process under magnetic field with a permanent magnet (1. aluminium mould, 2. magnetic distributors, 3. permanent magnet)

distribute magnetic field strength along the length of the beam evenly. A measured magnetic field strength along the surface of the distributor is 0.3 Tesla. Finally, the cured MRE core is bonded to two steel skins with the aid of epoxy glue (Araldite 2015).

(a) Sandwich beam dimensions for simply supported condition

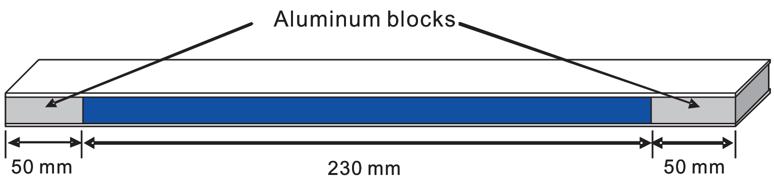

(b) Sandwich beam dimensions for clamped condition

Figure 6.2: The dimension of MRE configured sandwich beam

Figure 6.2 shows the dimension of MRE core and two aluminum skins. The MRE core is strongly bonded to two skins with the aid of epoxy glue (Araldite

Table 6.1: Properties of materials consisting sandwich beam

Material	Density (g/cm^3)	Shear Modulus (MPa)	Elastic Modulus (GPa)	Material Damping (η)
Steel skins	7.8	-	210	-
Aluminium skins	2.5	-	60	-
MRE core				
(0 Tesla)	3.1	2.5	-	0.13
(0.3 Tesla)		4.7	-	0.17

2015). For the clamped beam, each skin is extended 50 mm in length and two aluminum blocks are embedded at both ends.

Table 6.1 lists the properties of the steel skins and MRE core. The shear moduli of MRE are measured at 0.1% strain statically using electric testing instrument (Instron ElectroPlus E1000) with and without presence of electromagnetic field respectively (Choi *et al.* , 2008).

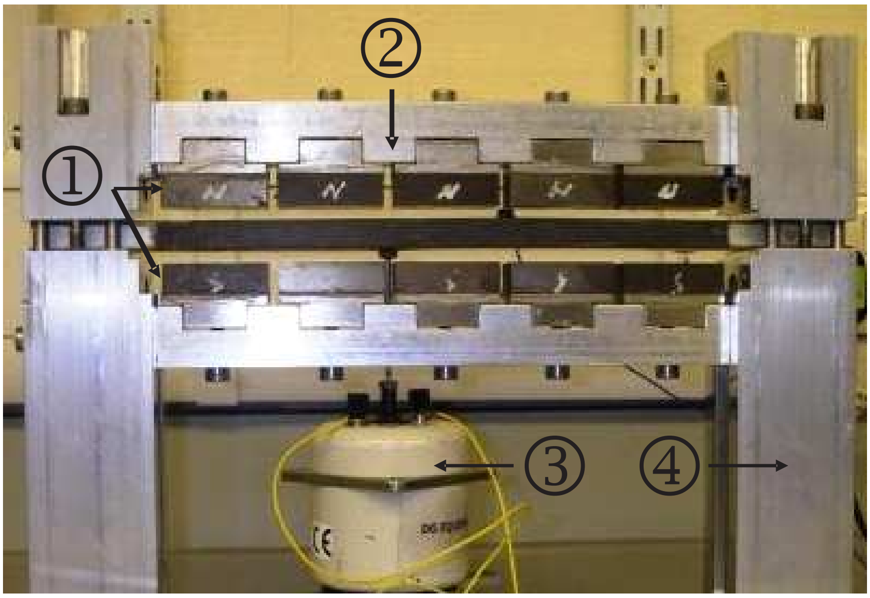

Figure 6.3: Forced vibration test rig (1. permanent magnets, 2. aluminium back plate, 3. shaker, 4. aluminium frame)

The forced vibration test rig consists of ten pieces of permanent magnets (N35 Block Magnet, MMG Magnet Ltd.) as shown in Fig. 6.3. Each magnet is bonded to the nonmagnetic stainless steel block for 24 hours. Stainless blocks are bolted to the aluminium back plates in order to mount and remove easily for experimental purpose. The size of each magnet is 42.0×24.0×12.5 mm^3 in order to maintain enough magnetic field strength. A 4 mm air gap between each magnet which allows a stinger of shaker to pass through and fix to the surface of the sandwich beam without any other contact. The frame is made of aluminium to prevent dissipation of magnetic field strength. Two aluminium back plates are mounted to the guided rails which allow back plates to adjust air gap between two sides of magnets by bolting. The default air gap between each side of magnet faces is 10 mm of which magnetic field strength is measured to be about 0.3 Tesla.

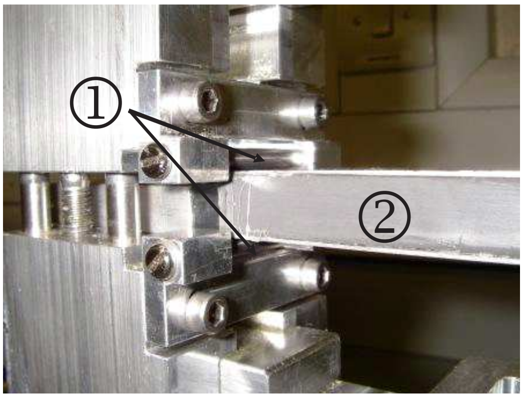

(a) Hinged support

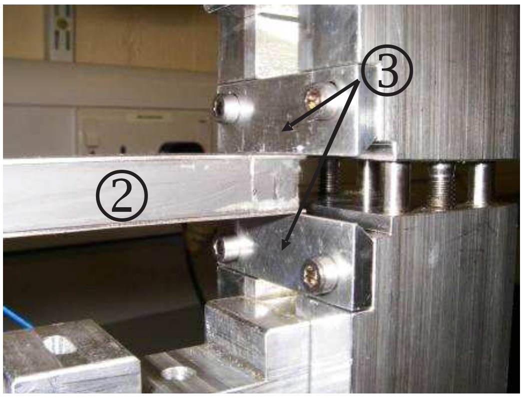

(b) Wedged support

Figure 6.4: Simply supported boundary with MRE embedded sandwich beam fitted in the vibration test rig (1. bearing pin, 2. sandwich beam, 3. wedge)

Fig. 6.4 shows the boundary conditions in the test rig. For an idealised simply supported beam, difficulties may arise in satisfying all of the requirements under experimental conditions. The following requirements for simply supported boundary conditions were satisfied in the design (Yalcintas & Dai, 2004): (1) the transverse displacement was zero at each end; (2) the moment was zero at each end; (3) axial force of the beam is zero and therefore the longitudinal displacement was free of constraint. In order to satisfy these condition, one end of beam is supported by hinged bearing pin (Fig. 6.4a) while the other end was supported by wedge shaped chamfer (Fig. 6.4b). The vertical displacement of the rolling pins was fixed while the longitudinal displacement was free. The pins could rotate freely, which satisfied the second requirement. This reduced a coupling effect from the vibration response caused by extra structures such as aluminium frame.

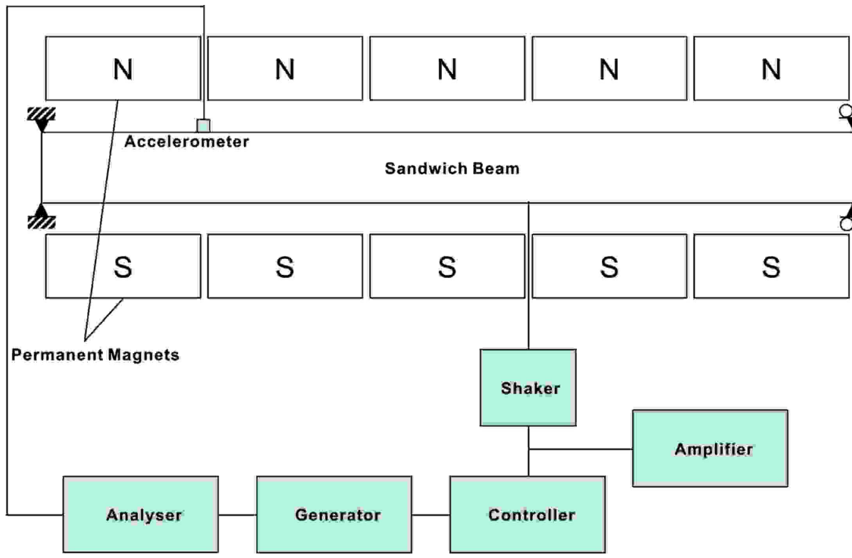

Figure 6.5: Forced vibration test diagram

Fig.6.5 shows forced vibration test diagram consisting of a test rig, a shaker (Ling Dynamics Systems V101), a PZT accelerometer (PCB352C22), a signal generator (Data Physics Quattro), a controller, an analyser and an amplifier. When the shaker applies the input force to the structure, the PZT accelerometer measures structural response. A signal generator produces a swept sine wave range from 0 to 1000 Hz in 1 Hz increments. A force signal received from the signal generator is varied by varying current. The PZT accelerometer is used to measure the vibrational acceleration at a single point. The stinger of the shaker is bonded to the bottom surface of the beam at a location of 138 mm ($3L/5$) from the left end of the beam while the accelerometer is attached to the top surface of the beam at a location of 46 mm ($L/5$) from the left end of the beam.

6.4 Results and Discussion

6.4.1 Sandwich beam with different thickness of skins

The purpose of this section is to compare frequency responses of beams with different skin thicknesses. The beams are vibrated under the action of a magnetic field along the entire beam length. Figure 6.6 shows the frequency response for the beam with 0.5 mm steel skins and 0.9 mm steel skins, respectively. Seven resonant peaks appear for the beam with 0.5 mm skins whereas five resonant peaks appear for that with 0.9 mm skins. The fundamental frequencies are also shifted to lower frequency ranges in the presence of magnetic field; this is due to the magnetic preload which is assumed to be at a low frequency (Yin *et al.* , 2006). As a consequence, magnetic preload seems to make the sandwich beam more flexible, and then the frequency response curve shifts to the left at lower frequency ranges. Compared to thick skins, the amplitude of resonant peak for the thin skinned sample is initially low, and therefore the changes of resonant peaks are relatively small. The frequency change of sandwich beam with 0.5 mm skins is smaller than that with 0.9 mm skins. The results also indicate that energy dissipation of the sandwich beam with thick skins is obviously due to large damping changes of MRE core as the magnetic field increased. This is because sandwich beam with thick steel skins induces more magnetic field than that with thin steel skins under the same magnetic field strength.

6.4.2 The effect with different boundary conditions of sandwich beam

The boundary condition effects with simply supported and clamped beam are observed to find differences in frequency changes and damping. Fig. 6.7 shows the comparison of frequency response of MRE embedded sandwich beam with different boundary conditions. The frequency change of clamped beam in Fig. 6.7 (b) is much bigger than that of simply supported beam in Fig. 6.7 (a). However, most of resonance peaks decrease at overall frequency ranges for simply supported beam

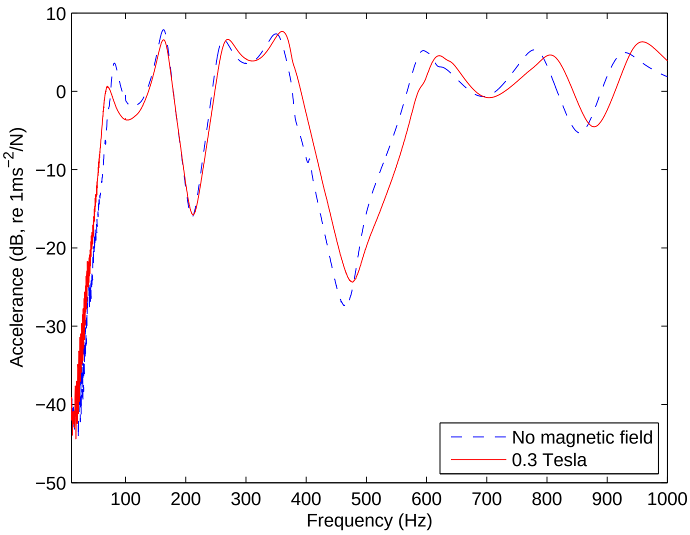

(a) 0.5 mm

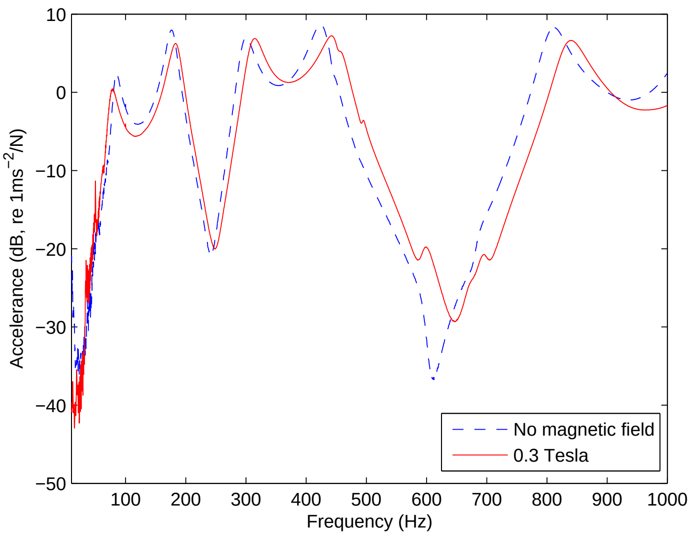

(b) 0.9 mm

Figure 6.6: Comparison of frequency change of MRE embedded sandwich beam with different thickness of the steel skins

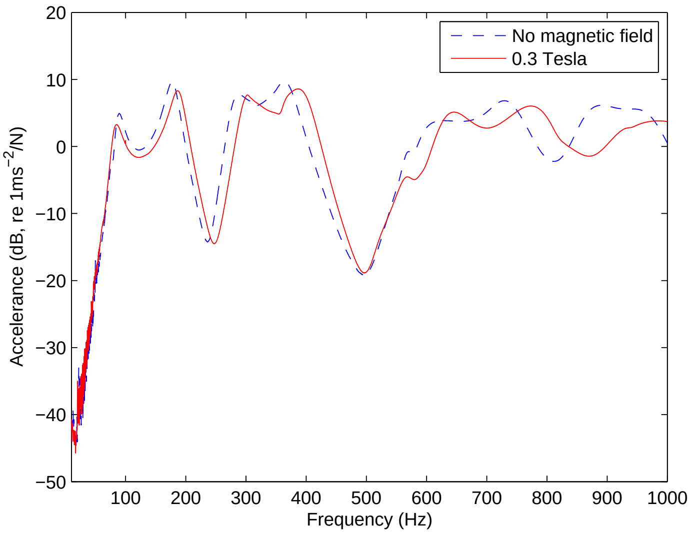

(a) Simply supported

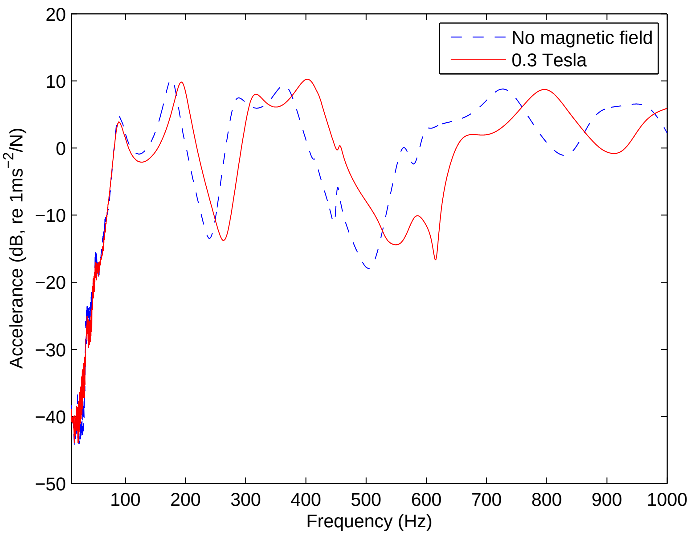

(b) Clamped

Figure 6.7: Comparison of frequency response of MRE embedded sandwich beam, aluminium skins, with different boundary condition

when the magnetic fields are applied to the structures. Conversely, the change of peak amplitude for the clamped beam is much less than that for simply supported beam. The results indicate that energy dissipation of simply supported beam are obvious because energy dissipation is caused by flexibility from the interface of the core and the aluminum skins. The fundamental frequencies are shifted to lower frequency in the presence of magnetic field, which is due to the magnetic preload effect at lower frequency ranges. Since the force are applied at nodal point, small peak response appears at mode 5.

6.4.3 The effect of different air gaps

Another aspect is the effect of magnetic field strength by adjusting air gap between two permanent magnetic faces. The strength of magnetic field changes from 0.3 to 0.35 Tesla by varying of air gap from 10 to 5 mm. The comparison of frequency

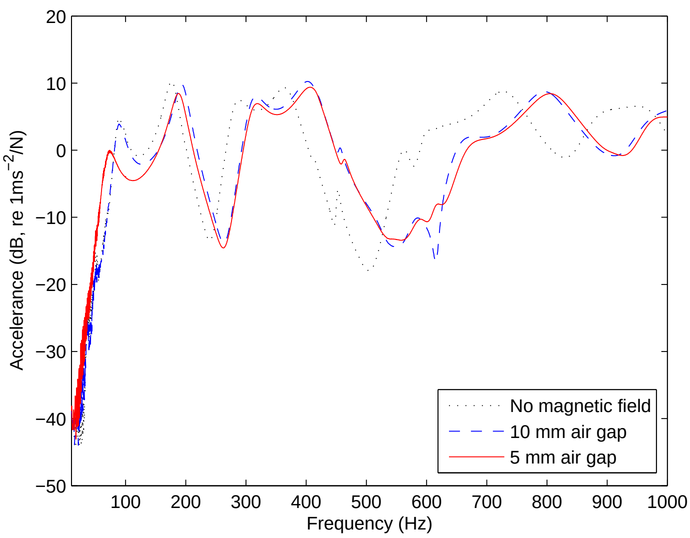

Figure 6.8: Comparison of frequency response of clamped aluminium MRE embedded sandwich beam with different air gap

response of clamped MRE embedded sandwich beam, aluminium skins, with different air gap are shown in Fig. 6.8. The first resonance frequency of 5mm air gap is shifted to lower frequency about 37% while that of 10mm air gap is not changed.

The damping ratio is determined by using half power bandwidth method for each mode given as

$$\xi = \frac{\omega_{+} - \omega_{-}}{\omega_n}, \tag{6.1}$$

where ω_{+} and ω_{-} are the corresponding frequencies to the 2dB reduction, ω_n is the resonance frequency. The damping ratio of the first mode of 5 mm air gap is 0.15 while that of 10 mm air gap is 0.08. From the second mode to higher mode, the damping ratio of 5 mm air gap is higher than that of 10 mm air gap. The results show that the magnetic field affects frequency changes as well as damping effect. At low frequency ranges, the magnetic preload effect is more obvious when the air gap between beam and magnets is 5 mm.

6.4.4 The effect of different forces applying

Since material behavior of rubber-like MRE materials is nonlinear, it causes different value of vibrational energy dissipation. Thus, the effect of applying force amplitude to observe damping effect is investigated. The range of the force amplitude ratio (f / f_{ref}) is applied from 1 to 10, where f and f_{ref} are the applying force and the reference force applied up to now, respectively. Fig. 6.9 shows comparison of frequency changes for clamped beam, aluminium skins, with 5mm air gap in terms of three different force amplitudes. With applying magnetic field, the fundamental frequency changes of each amplitude ratio (f / f_{ref}) at 1, 5 and 10 is 23%, 32% and 37% to the lower frequency ranges respectively. From the second to higher modes, resonant frequencies changes shift to the higher frequency ranges.

Fig. 6.10 shows the change of damping ratio in terms of various force amplitudes. Obvious damping changes are shown at first mode. Large damping change can be seen when the force amplitude ratio (f / f_{ref}) is 10. From second mode to higher mode, damping values drop down quickly and even lower than that of without magnetic field when the force amplitude ratio is 1. From the amplitude

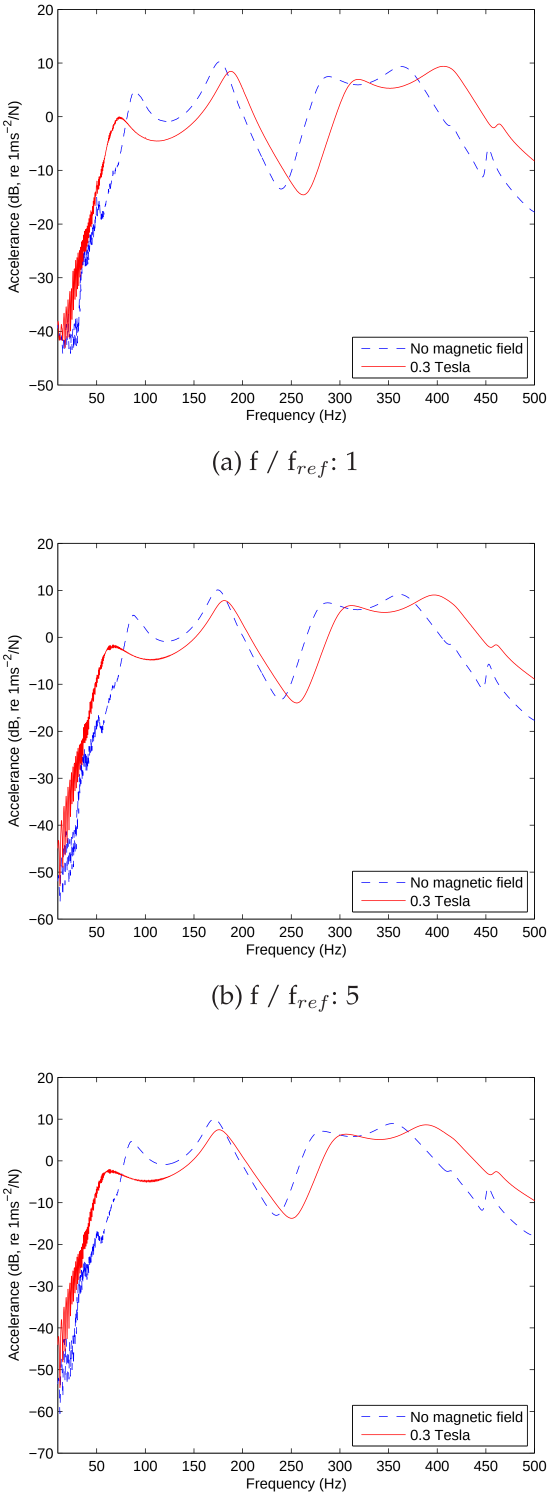

(a) f / f_{ref}: 1

(b) f / f_{ref}: 5

(c) f / f_{ref}: 10

Figure 6.9: Comparison of frequency response of clamped aluminum MRE embedded sandwich beam with different amplitude of input force (5 mm air gap)

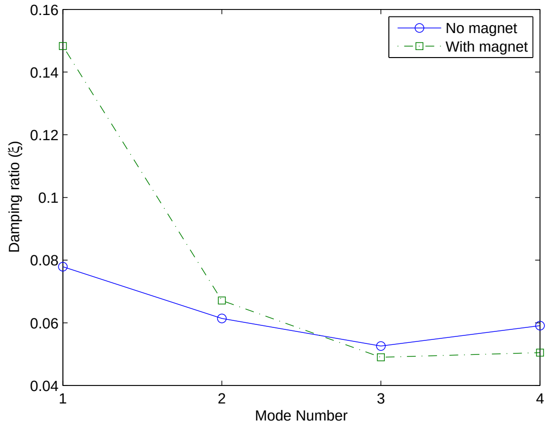

(a) f / f_{ref}: 1

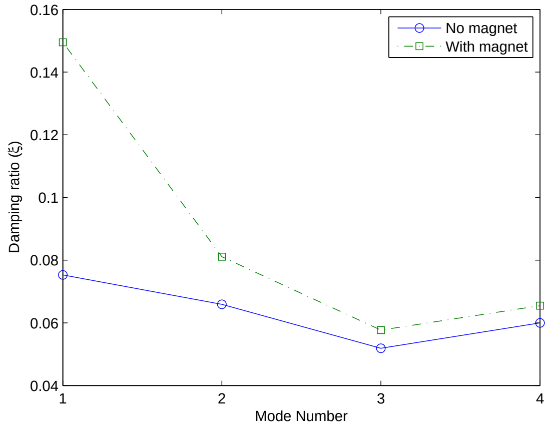

(b) f / f_{ref}: 5

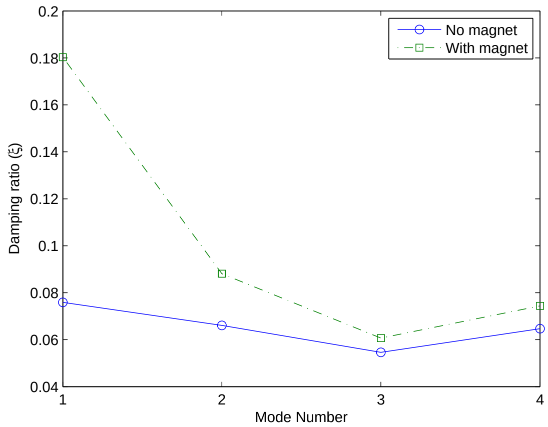

(c) f / f_{ref}: 10

Figure 6.10: Comparison of damping ratio of clamped aluminum MRE embedded sandwich beam with different amplitude of input force (5 mm air gap)

ratio of 5 to higher, when magnetic fields are applied damping effect is higher than that of without magnetic field.

The results confirm that when the amplitude of forced oscillation increases energy dissipation for the fundamental frequency increases. It seems that the magnetic force affects not only change of property of core material but also change of magnetic preload effect of the beam structure. These phenomena occur when the magnetic force is strong enough, which induce large shear stress at the interfaces between MRE core and aluminum skins.

6.4.5 Localised magnetic field effect

To better understand dynamic behaviour of MRE adapted beam overall frequency ranges, the localised magnetic field effect is considered with various combination of permanent magnets. In order to find out many resonant peaks up to 1000 Hz, a less stiffened sandwich beam with 0.5 mm steel and aluminum skins is used. Comparisons of frequency response of sandwich beam among various arrangement of magnetic fields are carried out. The force amplitude ratio (f / f_{ref}) used in these tests is 1.

Localised magnetic field effect on sandwich beam with steel skin

Fig. 6.11 shows a comparison of frequency response of simply supported steel-MRE sandwich beams between two and three pairs of magnetic fields, where 'M' stands for a pair of magnetic fields applied while 'O' stands for a pair of void area, that is, 'MMMMM' and 'OOOOO' represent magnetic fields and without magnetic field applied along the beam length, respectively. Because of magnetic preload, the resonant peaks of both cases decrease at first mode and frequency shifts to lower frequency ranges. Both frequency response curves show vibration amplitude reduction at 6th and 7th mode. The more peak reductions are shown at the case of two pairs of magnets in particularly. However the more resonant peaks increase at 8th mode.

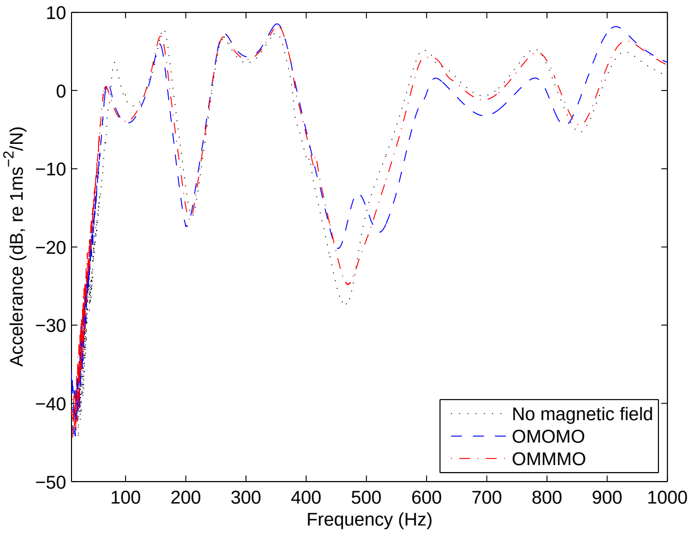

Figure 6.11: A comparison of FRF between two and three pairs of magnetic fields, simply supported beam

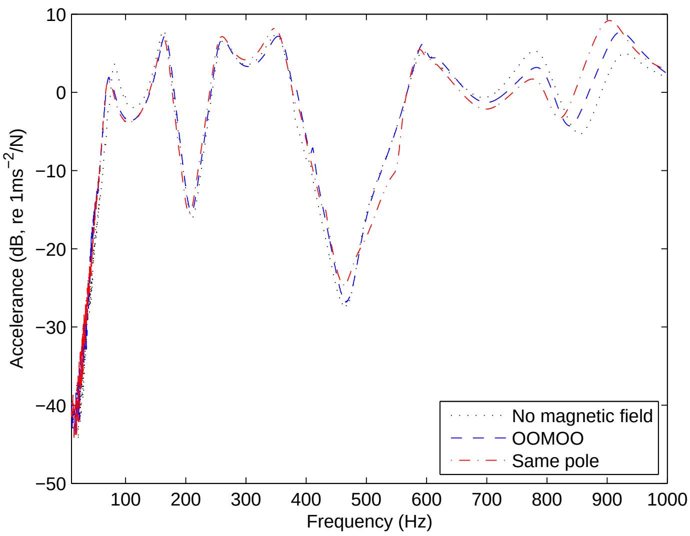

Figure 6.12: A comparison of FRF between one pair of different and same polarity of magnetic fields, simply supported beam

Fig. 6.12 shows the case of one pair of magnets in the middle and corresponding same polarity of magnetic fields. A magnetic preload affects less frequency changes compared to the case of two and three pairs of magnets. Also frequency changes of the rest of modes are not significant with one pair of magnets. Damping is shown at 7th mode with 3.4 dB reduction in the presence of magnetic field with same polarity. However, both peaks increase at 8th mode obviously. This indicates that vibration amplitude in particular mode can be controlled with even small area of magnetic field.

Damping effect of sandwich beam with aluminum skin

Fig. 6.13 shows the comparison of the damping change under a localised magnetic field with different arrangement such as three pairs of magnets fitted in the middle (OMMMO) and evenly distributed (MOMOM) for simply supported and clamped aluminum-MRE embedded sandwich beam. Change in damping ratio for the former case is more significant than that for the latter case. The magnetic preload effect for simply supported beam is much more than that for clamped beam. The results show that large damping effect happens when the magnetic fields are applied in the middle rather than the near of the boundaries.

Fig. 6.14a shows the damping change with two pairs of magnets mounted evenly along the beam (OMOMO) and same polarity for the clamped beam. Due to the limit number of permanent magnets only two pair of magnets are mounted in this test. Compared to the fully embedded magnets along the beam's length, the effect of damping changes are less significant. However, the dynamic behaviour of responses show difference between same and different polarity. When the magnets are mounted with same polarity, the damping effect is significant even if same number of magnets are used. Fig. 6.14b shows the comparison of damping change with two pairs of magnets mounted at both ends (MOOOM) and same polarity for the clamped beam. Higher damping change can be seen in the case of OMOMO at first two modes. These effects are no longer obvious when magnetic field are applied near of the boundaries.

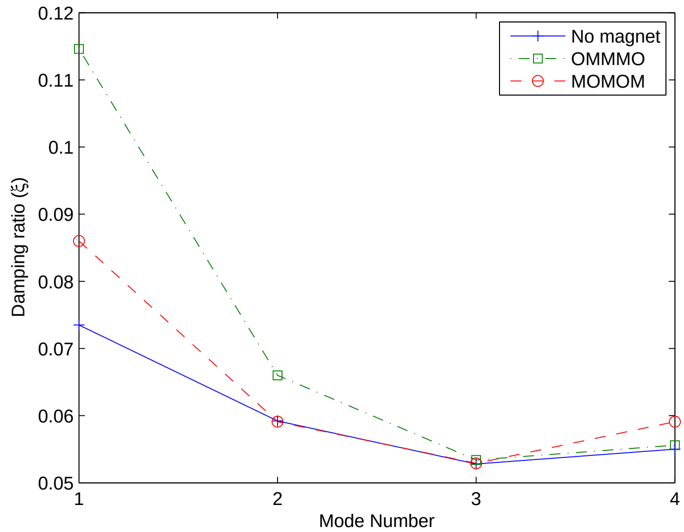

(a) Simply supported

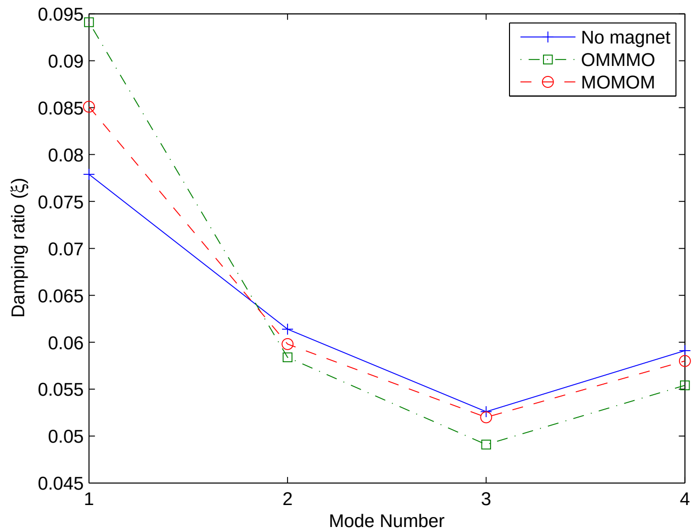

(b) Clamped beam

Figure 6.13: Comparison of frequency response of aluminum MRE embedded sandwich beam for different boundary conditions with three pair of different location of magnets

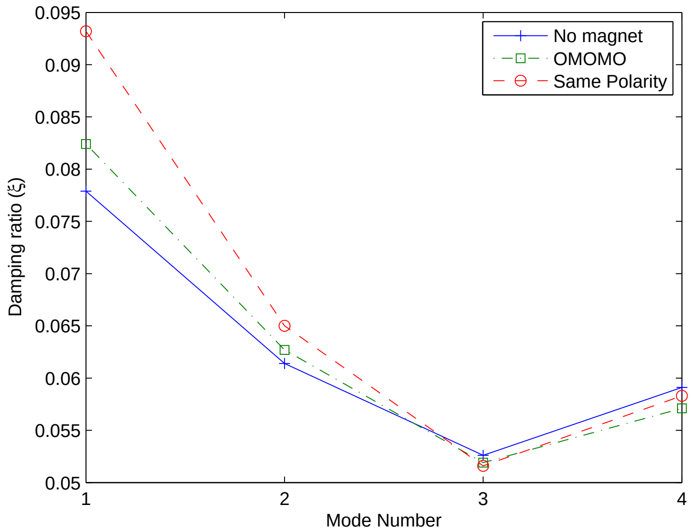

(a) OMOMO

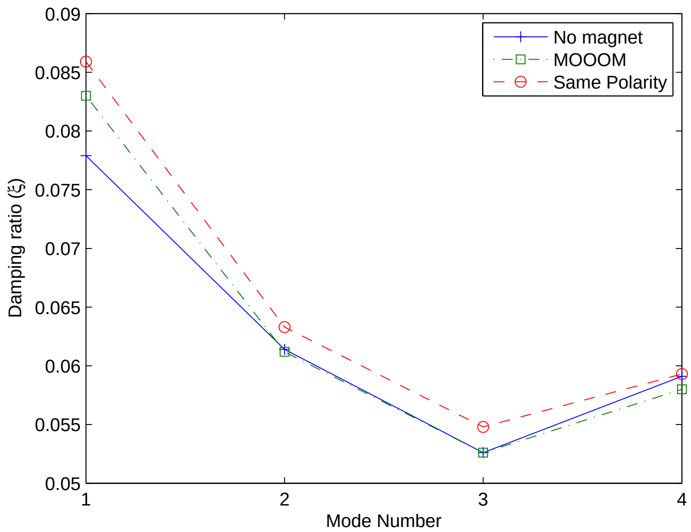

(b) MOOOM

Figure 6.14: Comparison of frequency response of clamped MRE embedded sandwich beam with same pole effect with two pairs of magnets, aluminium skin

6.5 Conclusions

New developed forced vibration test rig enables to carry out comprehensive experimental forced vibrational tests of MRE embedded sandwich beam with various aspects such as different magnetic field strength, various oscillations of force amplitudes, boundary conditions and damping effects under localised magnetic fields.

The results lead to the following conclusions.

- Frequency changes of clamped beam are more effective than those of simply supported beam. However, more damping effect was observed when beam is simply supported and when the air gap is reduced.
- Since the sandwich beam with thick steel skins induces more magnetic field than that with thin steel skins, more energy dissipation may occur with thick skins under the same magnetic field strength
- The change of damping values increases in proportion to the increase of the external force amplitude, the magnetic field strength and the number of permanent magnets.
- The damping changes are effective when magnetic fields are applied in the middle rather than near boundaries.
- The magnetic field with same polarity is shown to lead to different behaviour of dynamic characterisation of the beam compared with the case of magnetic field with different polarity.

Overall, MRE adaptive sandwich beams can be used where vibrational isolation and damping is needed. These results could be used to derive guidelines for potential applications for various shapes of MRE configured sandwich structures.

Chapter 7

Numerical Analysis of Smart Sandwich Beams Embedded with Magnetorheological Elastomer Cores

7.1 Introduction

Comprehensive experimental forced vibrational analyses of MRE embedded sandwich beam have been investigated in Chapter 6. Theoretical methods are needed to predict the dynamic response of smart sandwich beams, taking into account the viscoelastic properties of MRE cores. To achieve this, an analytical model based on Frostig's high order sandwich panel theory (HSAPT) is enhanced in order to include the damping of viscoelastic material properties and their frequency dependencies. The numerical analyses are then used to predict the dynamic characteristics of MRE embedded sandwich beam in terms of different boundary conditions and to localised magnetic effect.

7.2 Theoretical Formulation

To estimate the natural vibration characteristics of a sandwich beam, the homogeneous solution including natural frequencies and corresponding modes needs to be obtained. Then the variation of mode shapes and natural frequencies with free-free, cantilevered and clamped beam at both ends can be deduced.

There are many possible approaches to predict vibration behaviour of a sandwich beam, including classical sandwich theory, elastic foundation models and various higher order theories (Frostig & Baruch, 1994; Shenoi *et al.* , 2005). Since a shear-induced effect caused by the flexibility of the core needs to be modelled, a HSAPT appears to be most appropriate (Frostig, 1992; Frostig & Baruch, 1994; Nayak *et al.* , 2005).

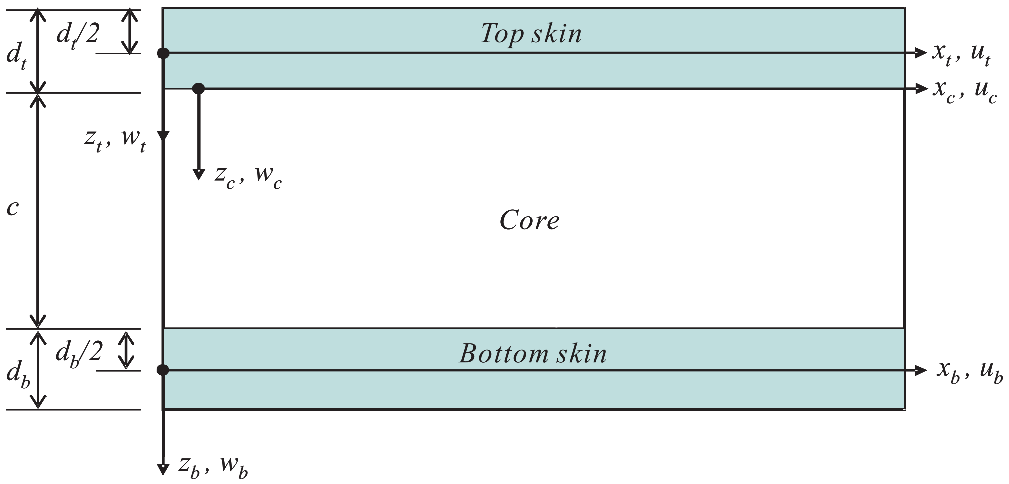

Figure 7.1: Geometry of sandwich beam (Frostig, 1992)

The geometry of a typical sandwich beam is illustrated in Fig. 7.1. In HSAPT, the skins of the sandwich beam are modelled as ordinary beams, without shear strains, that follow Euler-Bernoulli assumptions and are subjected to small deformations. The transversely flexible core layer is considered to be a two dimensional elastic medium with small deformations where its thickness may change under loading, and its cross section does not remain planar. The longitudinal (in-plane) stresses in the core can be neglected owing to the low flexural stiffness of the core material. The interface layers between the skins and the core are assumed to be bonded perfectly and to provide continuity of the deformations at the interfaces. Variational principles are found to constitute the key of many of the most useful techniques in fields of dynamics and continuum mechanics (Vinson, 1975). The governing equations describing the free vibrations of sandwich beams by Frostig (1992) have been adapted. The governing equations can be expressed via the variational calculus of Hamilton's principle, which requires that

$$\int_{t_1}^{t_2} \delta(T-U)dt = 0 \tag{7.1}$$

where T is the kinetic energy, U is the strain energy and δ is the variation operator.

The variation of the strain energy in terms of stresses and strains is

$$\begin{aligned}\delta U &= \int_{v_{top}} \sigma_{xx}^t \delta\epsilon_{xx}^t dv + \int_{v_{bot}} \sigma_{xx}^b \delta\epsilon_{xx}^b dv + \int_{v_{core}} \tau_c \delta\gamma_c dv \\ &\quad + \int_{v_{core}} \sigma_{zz}^c \delta\epsilon_{zz}^c dv \end{aligned}\tag{7.2}$$

where σ_{xx}^t, σ_{xx}^b and ϵ_{xx}^t, ϵ_{xx}^b are longitudinal normal stresses and strains in the top and the bottom skins respectively, τ_c and γ_c are the shear stress and strain in the core, σ_{zz}^c and ϵ_{zz}^c are the vertical normal stresses and strain in the core, v_{top}, v_{bot} and v_{core} are the volumes of the top and bottom skins and the core respectively, and dv denotes the volume of a differential segment. The relationship between the shear strain of the core and spatial derivative of the vertical and the longitudinal displacement is defined as

$$\gamma_c = u_{c,z} + w_{c,x}. \tag{7.3}$$

The variation of the kinetic energy is

$$\begin{aligned}\delta T &= \int_0^L m_t(\dot{u}_t\delta\dot{u}_t + \dot{w}_t\delta\dot{w}_t)dx \\ &\quad + \int_0^L m_b(\dot{u}_b\delta\dot{u}_b + \dot{w}_b\delta\dot{w}_b)dx \\ &\quad + \int_{v_{core}} \rho_c(\dot{u}_c\delta\dot{u}_c + \dot{w}_c\delta\dot{w}_c)dv \end{aligned}\tag{7.4}$$

where m_t, m_b represent are the mass per unit length of the top and bottom faces, ρ_c the density of the core, $\dot{u}_t$, $\dot{w}_t$ and $\dot{u}_b$, $\dot{w}_b$ the velocities of top and bottom surfaces in the longitudinal and the vertical directions respectively, and $\dot{u}_c$, $\dot{w}_c$ represent the core velocities in the horizontal and the vertical directions. $\dot{()}$ denotes a derivative with respect to time, x is the longitudinal co-ordinate, L is the length of beam.

Integration by parts yield at time between t_1 and t_2,

$$\begin{aligned} \int_{t_1}^{t_2} \delta T dt \quad = \quad & -\int_{t_1}^{t_2} \Big[\int_0^L m_t(\ddot{u}_t \delta u_t + \ddot{w}_t \delta w_t) dx \\ & + \int_0^L m_b(\ddot{u}_b \delta u_b + \ddot{w}_b \delta w_b) dx \\ & + \int_{v_{core}} \rho_c(\ddot{u}_c \delta u_c + \ddot{w}_c \delta w_c) dv \Big] dt = 0 \end{aligned} \tag{7.5}$$

where $\ddot{()}$ denotes a second derivative with respect to time.

An MRE core can be considered as a soft core. Generally, the static displacement field through the height of the core is nonlinear in the vicinity of the concentrated loads and supports. However, when a beam is subjected to distributed loads a linear distribution can be used (Frostig & Baruch, 1994). Since this simplification is needed only for the inertial participation effects of core, the longitudinal and vertical accelerations of the core can be approximated by a linear interpolation from those of face skins are

$$\ddot{w}_c(x, z_c, t) \quad = \quad (\ddot{w}_b - \ddot{w}_t) z_c / c + \ddot{w}_t, \tag{7.6}$$

$$\ddot{u}_c(x, z_c, t) \quad = \quad (\ddot{u}_c^b - \ddot{u}_c^t) z_c / c + \ddot{u}_c^t \tag{7.7}$$

where both $\ddot{u}_c^b$ and $\ddot{u}_c^t$ are the longitudinal accelerations of the bottom and the top skin-core interfaces respectively.

From variational calculus, the governing equations based on Frostig's HSAPT are extended to include viscoelastic material properties in terms of each variation (δu_t, δu_b, δw_t, δw_b, $\delta \tau_c$). The equations can then be expressed as (Sokolinsky *et al.* , 2002);

$$\begin{aligned} &E^* A_t u_{t,xx} + b\tau_c - (m_t + m_c/3)\ddot{u}_t - (m_c/6)\ddot{u}_b \\ &\qquad +(m_c d_t/6)\ddot{w}_{t,x} - (m_c d_b/12)\ddot{w}_{b,x} = 0, \end{aligned} \tag{7.8}$$

$$\begin{aligned} &E^* A_b u_{b,xx} - b\tau_c - (m_b + m_c/3)\ddot{u}_b - (m_c/6)\ddot{u}_t \\ &\qquad -(m_c d_b/6)\ddot{w}_{b,x} + (m_c d_t/12)\ddot{w}_{t,x} = 0, \end{aligned} \tag{7.9}$$

$$\begin{aligned} &E^* I_t w_{t,xxxx} - ((c + d_t)b/2)\tau_{c,x} - (bE_c^*/c)(w_b - w_t) + (m_t + m_c/3)\ddot{w}_t \\ &\qquad +(m_c/6)\ddot{w}_b + (m_c d_t/6)\ddot{u}_{t,x} + (m_c d_t/12)\ddot{u}_{b,x} - (m_c d_t^2/12)\ddot{w}_{t,xx} \\ &\qquad\qquad +(m_c d_t d_b/24)\ddot{w}_{b,xx} = 0, \end{aligned} \tag{7.10}$$

$$\begin{aligned} &E^* I_b w_{b,xxxx} - ((c + d_b)b/2)\tau_{c,x} + (bE_c^*/c)(w_b - w_t) + (m_b + m_c/3)\ddot{w}_b \\ &\qquad +(m_c/6)\ddot{w}_t - (m_c d_b/6)\ddot{u}_{b,x} + (m_c d_b/12)\ddot{u}_{t,x} - (m_c d_b^2/12)\ddot{w}_{b,xx} \\ &\qquad\qquad +(m_c d_t d_b/24)\ddot{w}_{t,xx} = 0, \end{aligned} \tag{7.11}$$

$$\begin{aligned} &u_b - u_t - (c/G_c^*)\tau_c + ((c^3/12)/E_c^*)\tau_{c,xx} + ((c + d_t)/2)w_{t,x} \\ &\qquad +((c + d_b)/2)w_{b,x} = 0, \end{aligned} \tag{7.12}$$

where A_t, A_b represent the cross sectional areas of the top and bottom skins, I_t, I_b are second moments of inertia of the top and bottom skins, and E^*, E_c^* and G_c^* are the complex Young's moduli of skins and core and the complex shear modulus of the core where,

$$E^* = E' + iE'', \tag{7.13}$$

$$E_c^* = E_c' + iE_c'', \tag{7.14}$$

$$G_c^* = G_c' + iG_c'', \tag{7.15}$$

where E', E_c', G_c' represent the storage moduli and E'', E_c'', G_c'' are the loss moduli of the phase properties.

The boundary conditions for the top and bottom skins at the left (x=0) and right (x=L) edges of the sandwich beam, derived via the variational principles imposed on the strain energy (U) and the kinetic energy (T), are;

$$N^p_{xx}(x=0,L) = E^* A_p u_{p,x} = 0 \quad or \quad u_p = 0, \tag{7.16}$$

$$M^p_{xx}(x=0,L) = E^* I_p w_{p,xx} = 0 \quad or \quad w_{p,x} = 0. \tag{7.17}$$

Compatibility equations between skins and core are;

$$\begin{aligned} E^* I_t w_{t,xxx} - (d_t b/2)\tau_c + (m_c d_t/6)\ddot{u}_t + (m_c d_t/12)\ddot{u}_b \\ -(m_c d_t^2/12)\ddot{w}_{t,x} + (m_c d_t d_b/24)\ddot{w}_{b,x} = 0, \end{aligned} \tag{7.18}$$

$$\begin{aligned} E^* I_t w_{b,xxx} - (d_b b/2)\tau_c - (m_c d_b/12)\ddot{u}_t - (m_c d_b/6)\ddot{u}_b \\ -(m_c d_b^2/12)\ddot{w}_{b,x} + (m_c d_t d_b/24)\ddot{w}_{t,x} = 0, \end{aligned} \tag{7.19}$$

where N^p_{xx} and M^p_{xx} are the axial force and the bending moment capabilities of the skins.

The boundary conditions relevant to any point along the height(z) of the core are as follows,

$$\begin{aligned} \tau_c(x=0) = 0, \tau_c(x=L) = 0 \qquad or \\ w_c(x=0, z=z_c) = 0, \quad w_c(x=L, z=z_c) = 0. \end{aligned} \tag{7.20}$$

The general vibration equation of motion can be written as

$$[\mathbf{M}][\ddot{\Delta}] + [\mathbf{K}^*][\Delta] = 0 \tag{7.21}$$

where **[M]** is the mass matrix and **[K*]** is the complex stiffness matrix.

The displacement vector is

$$[\Delta]^T = [w_t \quad w_b \quad u_t \quad u_b \quad \tau_c] \tag{7.22}$$

where w_t, w_b and u_t, u_b are the displacements of top and bottom surfaces of the beam in the vertical and the horizontal directions, respectively.

To analyze free vibration, assuming harmonic behaviour in time, a general solution of the form, $[\Delta]$=$[\Lambda]$exp($i\omega t$) is considered where ω is the complex eigen frequency and t is the time. Thus the governing (Eq. 7.21) can be expressed as,

$$([\bar{\mathbf{K}}^*] - \lambda^*[\bar{\mathbf{M}}])[\Lambda] = 0 \tag{7.23}$$

where λ^* is a complex eigenvalue, $[\Lambda]$ is the matrix of eigenvectors and $[\bar{\mathbf{M}}]$ and $[\bar{\mathbf{K}}^*]$ are ordinary symmetric matrices of the mass and frequency dependent complex stiffness respectively, details of which are given in appendix A. The full solution of the free vibration problem is achieved with the appropriate boundary conditions. After obtaining the complex eigenvalues, the complex circular frequency Ω^* and the modal loss factor η_n of the sandwich beam can be calculated for each mode using Eq. 7.24.

$$\lambda_n^* = \lambda_n' + i\lambda_n'', \eta_n = \frac{\lambda_n''}{\lambda_n'} \tag{7.24}$$

where, $\lambda_n^{'}$ and $\lambda_n^{''}$ are real and imaginary eigen values respectively (Choi *et al.* , 2007). The transverse displacement of each skin $w_p(x,t)$, is

$$w_p(x,t) = \sum_{n=1}^{\infty} \psi_n^p(x) q_n^p(t) \tag{7.25}$$

$$F(t) = \rho F_0 e^{i\omega t}\delta(x - x_a) \tag{7.26}$$

where $\psi_n^p(x)$ are mass normalised mode shapes and $q_n^p(t)$ the time dependent coordinates respectively, (p denotes t(top) or b(bottom)), δ represents Dirac delta function. Substituting Eqs. (7.25) and (7.26) into Eq. 7.21 and dividing displacement in the frequency domain by force, the receptance function of each skin is given by (Choi *et al.* , 2009a)

$$\frac{w_p(x,\omega)}{F_0} = \sum_{n=1}^{\infty} \frac{sin(n\pi x_a/L)}{\Omega_n^2(1 + j\eta_n) - \omega^2} sin(n\pi x/L). \tag{7.27}$$

7.3 Numerical Results and Discussions

7.3.1 Validation of free vibration of sandwich beams for different boundary conditions

Simply supported sandwich beam

To validate higher order theory, free vibration analysis for a simply supported sandwich beam with PVC core is compared with that carried out by Jensen & Irgens (1999). The span of the sandwich beam is 300 mm and the width is 50 mm. The thickness of both face skins and soft foam core are 2 mm and 30 mm, respectively. Theoretical results are obtained by using Eq. 7.23 and the numerical results are obtained by using finite element software ABAQUS. The mechanical properties of steel skins and soft core (PVC) in sandwich beam are shown in Table 7.1. The Lanczos eigensolver provided by ABAQUS is used to compute the natural frequencies and corresponding mode shapes of the sandwich beam. The model consists of 2550 CPE8, 8 node biquadratic plain strain elements and 7985 nodes. The analytical results by using Frostig's higher-order approach beam theory are

Table 7.1: Properties of a sandwich beam with steel skins and a PVC core (Sokolinsky *et al.* , 2002)

	$Material$ $Name$	$Young's$ $Modulus$ $E(GPa)$	$Shear$ $Modulus$ $G(GPa)$	$Poisson's$ $ratio$	$Density$ (kg/m^3)
$Skins$	$Steel$	210	81	0.3	7900
$Core$	$PVC\ (H60)$	0.056	0.022	0.27	60

Table 7.2: Comparison of natural frequencies (Hz) of a simply supported sandwich beam

	$Antisymmetric\ modes$			$Symmetric\ modes$		
$Mode$	$Experiment$	$Prediction$		$Experiment$	$Prediction$	
	(Jensen & Irgens, 1999)	$ABAQUS$	$Higher\ order$	(Jensen & Irgens, 1999)	$ABAQUS$	$Higher\ order$
1	263	245	258	-	2640	2447
2	-	522	549	-	2658	2459
3	889	861	890	-	2690	2490
4	1289	1268	1300	-	2693	2583
5	1774	1767	1791	-	2848	2769
6	-	2349	2370	3358	3146	3079
7	-	3032	3043	-	3575	3530
8	3806	3769	3812	-	4011	4127
9	4621	4398	4682	-	4423	4867

compared with the results from experiments (Jensen & Irgens, 1999) and numerical results calculated as shown in Table 7.2. It is seen that the natural frequencies obtained using higher order theory agree well with experimental data except at higher frequencies (over 3000 Hz). Symmetric modes occur at higher frequencies.

Sandwich beams with different boundary conditions

Numerical calculations for sandwich beam at different boundary conditions are presented next. Finite difference method (FDM) is used to approximate the governing equations and to predict natural motions of sandwich beams with various boundary conditions. Using central difference scheme quantitative comparisons between the anticipations of the mode shapes were carried out with the experimental results (Jensen & Irgens, 1999) for the sandwich beam by Sokolinsky *et al.*

(2002).

The harmonic displacement of the sandwich beam with respect to the unknown function can be expressed as

$$u(x,t) = u(x)e^{i\omega t}, w(x,t) = w(x)e^{i\omega t} \tag{7.28}$$

Discretization of each variable in frequency domain can be expressed as follows;

$$w^p{}_{,xxxx} = \frac{w^p_{i+2} - 4w^p_{i+1} + 6w^p_i - 4w^p_{i-1} + w^p_{i-2}}{h^4}, \tag{7.29}$$

$$w^p{}_{,xx} = \frac{w^p_{i+1} - 2w^p_i - w^p_{i-1}}{h^2} \tag{7.30}$$

$$w^p{}_{,x} = \frac{w^p_{i+1} - w^p_{i-1}}{2h} \tag{7.31}$$

$$u^p{}_{,xx} = \frac{u^p_{i+1} - 2u^p_i - u^p_{i-1}}{h^2} \tag{7.32}$$

$$u^p{}_{,x} = \frac{u^p_{i+1} - u^p_{i-1}}{2h} \tag{7.33}$$

$$\tau_{,xx} = \frac{\tau_{i+1} - 2\tau_i - \tau_{i-1}}{h^2} \tag{7.34}$$

$$\tau_{,x} = \frac{\tau_{i+1} - \tau_{i-1}}{2h} \tag{7.35}$$

where, p denotes t(top) or b(bottom).

After substituting Eq. 7.29 to Eq. 7.35 into Eq. 7.12 and manipulating a discretized governing equation in terms of the corresponding variables can be obtained. The details are described in Appendix B.

A finite difference grid of 3 mm intervals was used to calculate Frosgtig's higher order theory numerically. For the boundary problem with second and fourth order of the derivative, fictitious points at each end have been used. In this calculation, the boundary conditions of both top and bottom skins are identical. As the grid density increases, larger and increasingly sparse mass and stiffness matrices are obtained.

Boundary conditions are described from Eq. 7.16 to Eq. 7.21. For a clamped sandwich beam, the shear force and displacement of the beam at each boundary is zero. For a free-free sandwich beam, the moment and the shear force at each boundary is zero. For a cantilever sandwich beam, one edge of the beam a clamped boundary condition is applied and a free boundary condition is applied on the other edge of the beam.

Table 7.3: Comparison of natural frequencies (Hz) a sandwich beam with different boundary conditions

$Mode$	$Free-free$		$Cantilever$		$Clamped$	
	$ABAQUS$	$Higher\ order$	$ABAQUS$	$Higher\ order$	$ABAQUS$	$Higher\ order$
1	514	511	128	125	283	282
2	759	785	398	394	590	599
3	1147	1144	704	701	941	978
4	1404	1486	1047	1010	1348	1334
5	1653	1681	1446	1481	1822	1877
6	1990	2090	1908	1939	2370	2393
7	2524	2593	2445	2490	2651	2612
8	2601	2606	2604	2609	2657	2616
9	2607	2612	2637	2637	2695	2620
10	2631	2675	2663	2666	2716	2711

Using higher order sandwich plate theory, numerical free vibration analysis results are compared with FEA solutions. Natural frequencies of the sandwich beam for each boundary condition are presented in Table 7.3. Numerical results from Frostig's higher order sandwich theory are found to match well with those of FEA solutions.

Fig. 7.2 and Fig. 7.3 show the bending mode shapes of cantilever and clamped

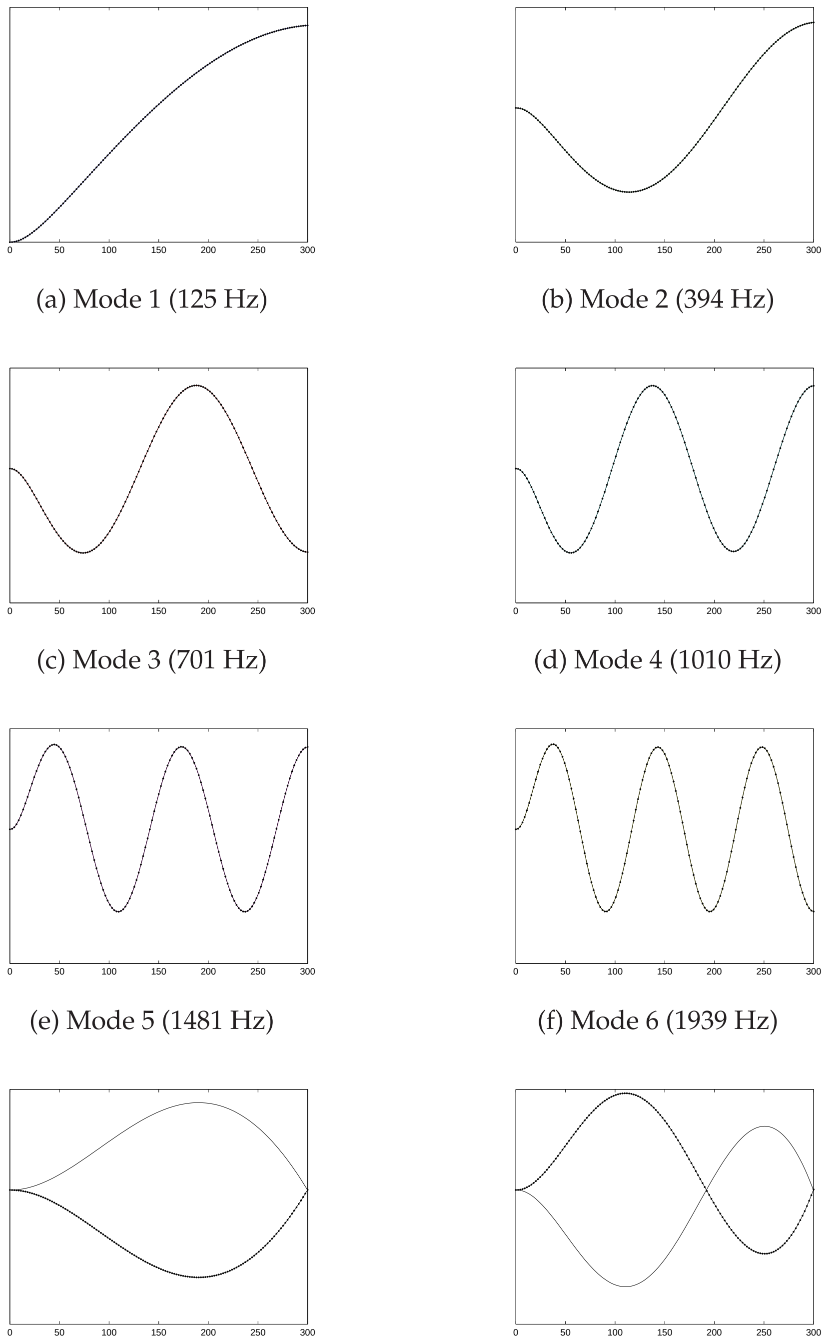

(a) Mode 1 (125 Hz)

(b) Mode 2 (394 Hz)

(c) Mode 3 (701 Hz)

(d) Mode 4 (1010 Hz)

(e) Mode 5 (1481 Hz)

(f) Mode 6 (1939 Hz)

(g) Mode 7 (2490 Hz)

(h) Mode 8 (2609 Hz)

Figure 7.2: Bending mode shape of the cantilever beam at top skin (solid line) and bottom skin (dotted line) (Abscissa - Beam span in mm and Ordinate - Normalised displacement)

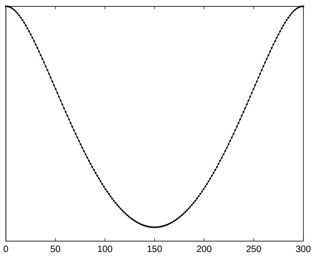

(a) Mode 1 (282 Hz)

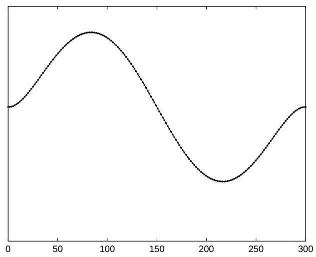

(b) Mode 2 (599 Hz)

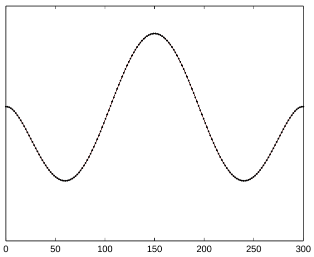

(c) Mode 3 (978 Hz)

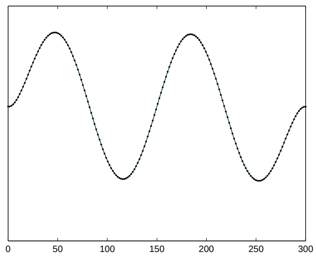

(d) Mode 4 (1334 Hz)

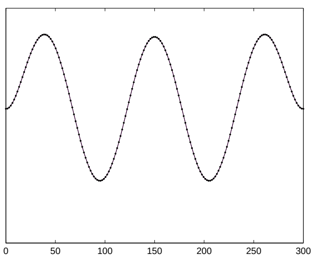

(e) Mode 5 (1877 Hz)

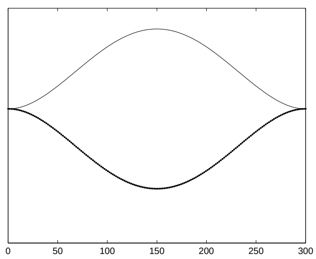

(f) Mode 6 (2393 Hz)

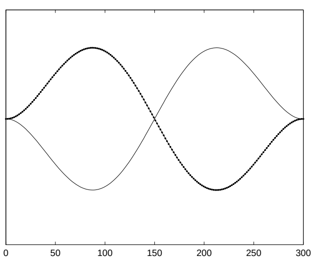

(g) Mode 7 (2612 Hz)

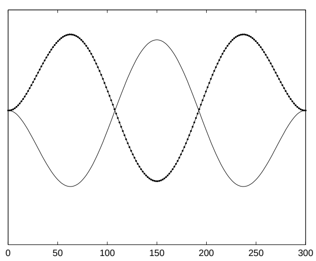

(h) Mode 8 (2616 Hz)

Figure 7.3: Bending mode shape of the clamped beam at top skin (solid line) and bottom skin (dotted line) (Abscissa - Beam span in mm and Ordinate - Normalised displacement)

sandwich beams, respectively. Most of vibration modes are similar to those of a homogeneous beam. That is to say, the top and bottom skins move in phase with each other in the antisymmetric mode. However, the symmetric modes occur at higher frequencies (after 2000 Hz) for both cantilevered and clamped beams.

7.3.2 The effect of MRE core on dynamic behaviour of the sandwich beam

A comparison of the transverse vibration frequency responses between the forced vibration test result and the theoretical prediction for simply supported sandwich beam using Eq. 7.27 is shown in Fig. 7.4. The dimension of the sandwich beam is the same as used in Chapter 6. Theoretical predictions of transfer accelerance are shown in Fig. 7.4a. For numerical simplicity, sinusoidal mode shape function is used to solve the eigen value problem, i.e: Eq. 7.27. The property of steel skins and MRE core are given in Table 6.1. As the magnetic field is applied, the frequency curve shifts to higher frequency ranges. Resonant peaks also decrease as the material damping increases in the presence of a magnetic field. Since the excitation and sensing points are exactly the same as the nodal points of the fifth mode, both resonant peaks of the fifth mode disappear.

The theoretical predictions show reasonable agreement with the the experimental results carried out in Chapter 6 except at higher frequencies (between 800 Hz and 900 Hz), see Fig. 7.4b. In the presence of a magnetic field, both theoretical and experimental curves shift to higher frequency ranges . However, the fundamental frequency shifts to the lower frequency ranges in the presence of a magnetic field in experimental results. This is due to the magnetic preload which is assumed to be at a low frequency (Yin *et al.* , 2006).

A comparison of the damping effect between theoretical prediction and experimental results are shown in Fig. 7.5. Modal damping from prediction of higher order theory shows a good agreement with experimental results, even if the damping ratio from the experiments deviates. In both theoretical and experimental results, higher damping is shown when a magnetic field is applied. Experimental

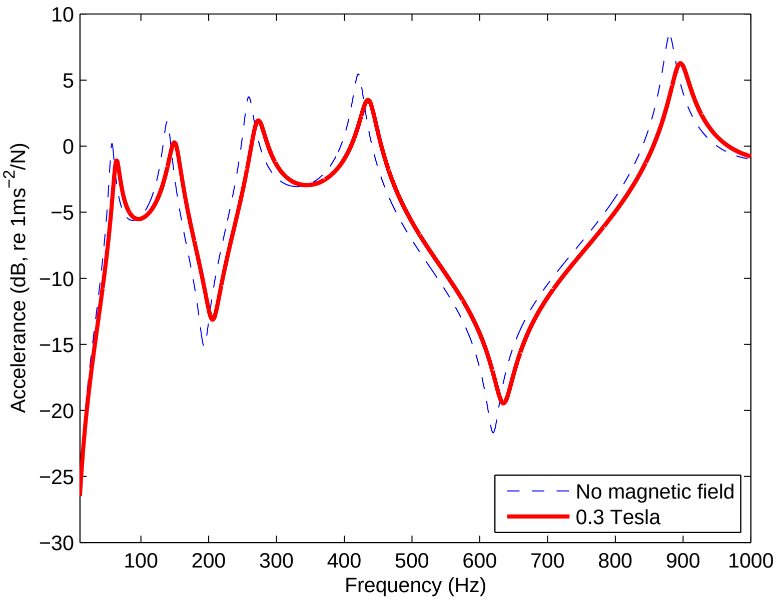

(a) Higher order theory

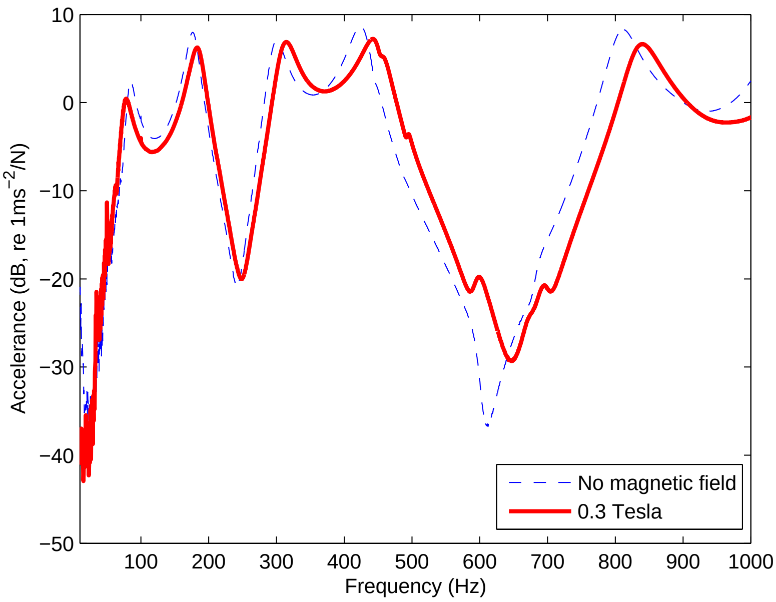

(b) Experimental results

Figure 7.4: Comparison of frequency responses of MRE embedded sandwich beam with 0.9 mm steel skins

modal loss factor is high at lower mode whereas damping ratios are low at higher modes. This phenomena is also predicted theoretically.

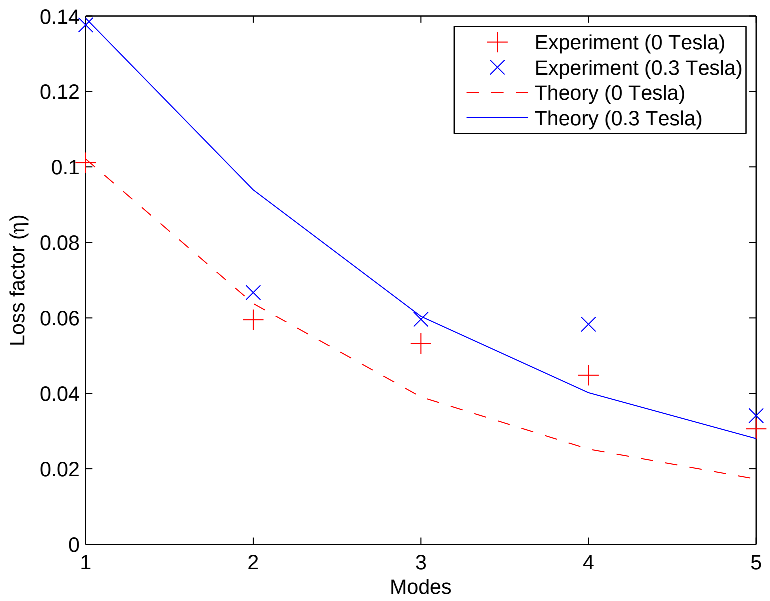

Figure 7.5: Comparison of damping effect

7.3.3 Damping changes with different topologies

In this section, theoretical sensitivity analysis to investigate the damping effects of configuration of material dimension on sandwich structures is presented. For the parametric study, the default dimensions of the MRE core and two different types of steel skins are $230 \times 20 \times 10$ mm^3 and $230 \times 20 \times 0.5$ mm^3. The properties of the skin and MRE are indicated in Table 6.1. Since the magnetic preload effect is very small (Zhou & Wang, 2006), the induced magnetic field in the steel skins is assumed to be zero in this theoretical analysis.

Fig. 7.6a shows the damping change in sandwich beams in terms of different skin thicknesses. Three sandwich beams with different thickness of skins are compared. The modal loss factor change decreases at higher mode numbers. There is a tendency for the change to be constant beyond a certain mode number. It is also clear that the damping change is higher for the thinner skinned sandwich beam.

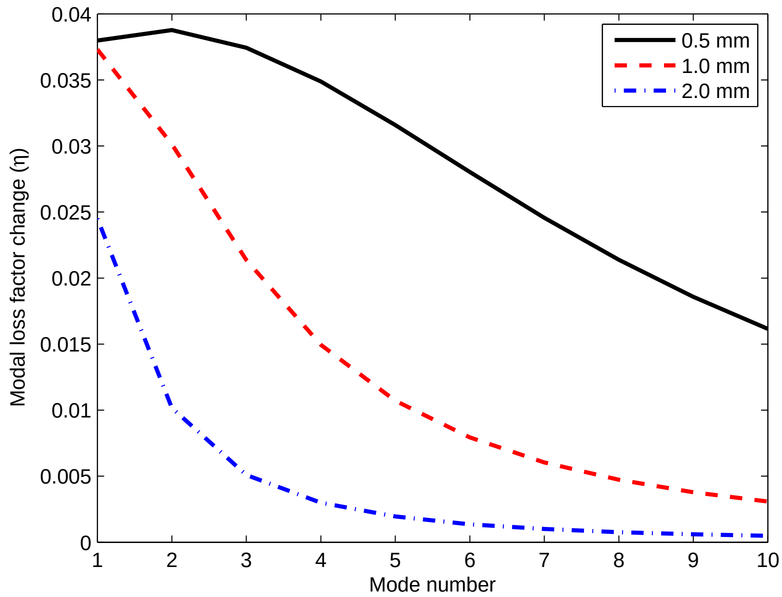

(a) Different thickness of skins (10 mm core)

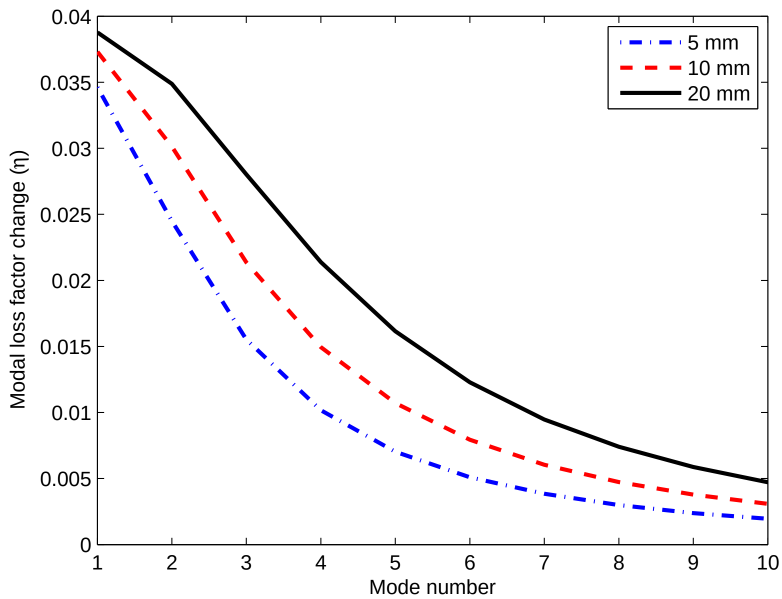

(b) Different thickness of cores (1 mm skin)

Figure 7.6: A comparison of damping in terms of different topologies

This is consistent with the larger effect of a relatively thicker core. Fig. 7.6b shows the damping change in sandwich beams for varying core thickness (5 mm, 10 mm and 20 mm). The three curves show similar patterns. Damping change decreases as the mode number increases. The highest damping change is shown for 20 mm core thickness. As the thickness of the core increases, the damping change increases. From these results, as long as the flexural stiffness and structural stability requirements are satisfied, relatively thicker cored sandwich beams exhibit greater damping effects.

7.3.4 MRE cored sandwich beam under localised magnetic field

Experimental comparison of frequency response of simply supported steel-MRE sandwich beams between two and three pairs of magnetic fields was shown in Fig. 6.11 in Chapter 6. In order to investigate the effect under various combination of magnetic fields, FE analysis for clamped aluminium-MRE sandwich beams with two and three pairs of magnetic fields are carried out. The dimension of MRE core and two aluminum skins are as shown in Fig. 6.2. The thickness of the aluminum skin is 0.5 mm. For numerical simplicity, the MRE core is divided into five equal sections. The properties of the aluminum skins and the MRE core are as given in Table 6.1. The shear modulus of MRE can vary under localised magnetic fields.

Fig. 7.7 shows the change of fundamental frequency, with reference to frequency without magnetic field (OOOOO), under a localised magnetic field with different arrangements including two and three pairs of permanent magnets fitted in the middle (OMOMO / OMMMO) and at the boundaries (MOOOM / MOMOM), in terms of various boundary conditions. For the case of MOMOM the maximum frequency change is about 18% in the clamped boundary condition and 22% in the simply supported boundary condition. Relatively small amount of frequency changes are shown for cantilever beam. It is interesting that the amount of frequency shift for a simply supported beam with two pairs of magnets at boundaries (MOOOM) shows bigger values (20%) than those (8%) with three pairs of

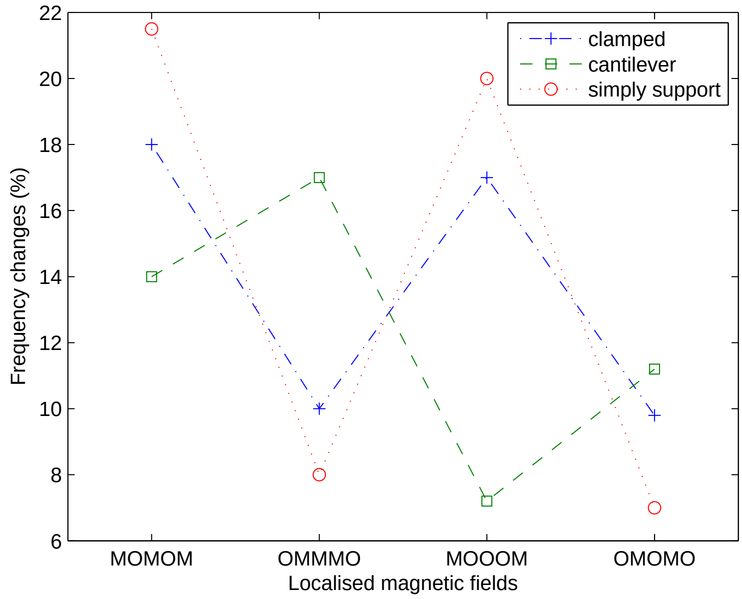

Figure 7.7: Fundamental frequency change of MRE cored sandwich beam under a localised magnetic field

magnets in the middle (OMMMO). In other cases, it is seen that the frequency change effects become smaller with the decrease of applied magnetic field area. However, significant difference of MR performance is observed, which depends on the locations of magnetic field applied even if the same amount of magnetic field area is applied. Moreover, the frequency changes in the cantilever beam at each case shows different behaviour compared to those in the simply supported and clamped boundary conditions.

Fig. 7.8 shows the frequency responses of a MRE configured clamped sandwich beam under a localised magnetic field. The solid line represents the result without magnetic field whereas the dotted lines represents that under a magnetic field. The frequency responses under two pairs of magnetic fields are shown in Fig. 7.8a. Interestingly, the amount of frequency shift at each mode between OMOMO and MOOOM are different. After the second resonant peak, the behaviour of frequency shift changes. The behaviours of frequency shifts under three pairs of magnetic fields can be seen in Fig. 7.8b. Similarly, the behaviour of the frequency shifts between MOMOM and OMMMO changes after the second resonant peak. This indicates that the localised magnetic field can change whole characteristics of MRE configured sandwich beams.

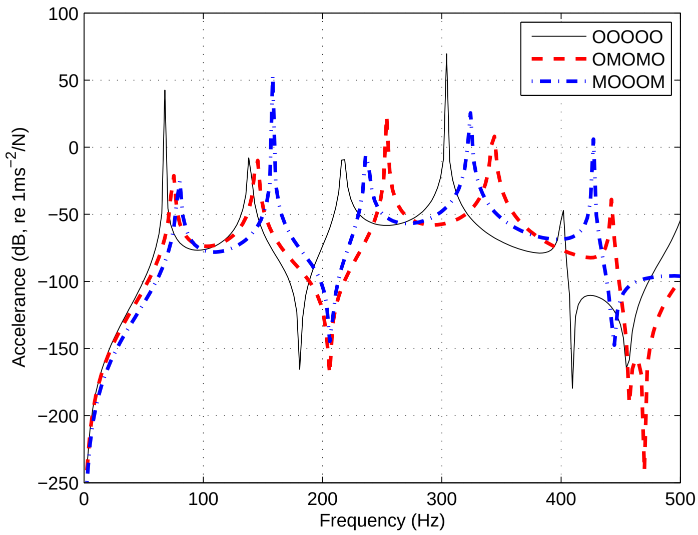

(a) Two pairs of magnetic fields

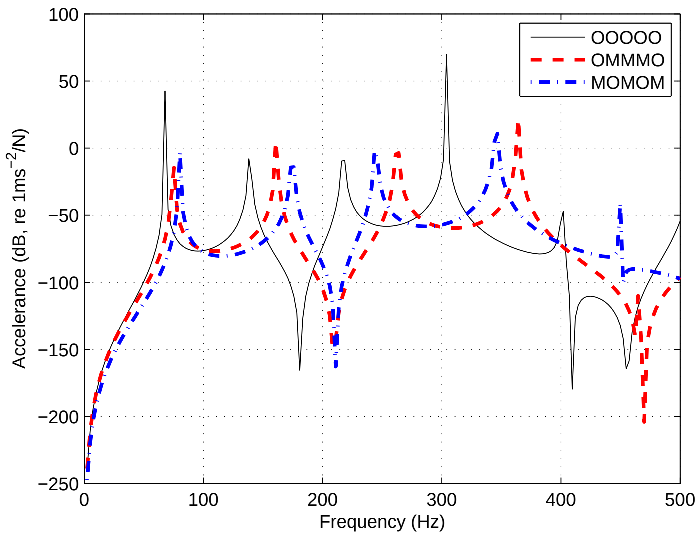

(b) Three pairs of magnetic fields

Figure 7.8: Comparison of frequency change of MRE embedded clamped sandwich beam under localised magnetic field

7.4 Conclusions

In this chapter, the vibration characteristics of MRE core sandwich beams were investigated to understand the pheonomenon of frequency and damping changes under a magnetic field, theoretically and numerically.

Higher order sandwich beam theory was adapted to include the damping properties of MRE. Validations for the analytical model show reasonable agreement with experimental and FEA results. Theoretical sensitivity analyses show damping effect in terms of different topologies. It is seen that relatively thicker cored sandwich beam exhibits more damping effect. FEA results revealed that different MR performance can be achieved which depends on the location of magnetic fields applied even with same amount of magnetic field area. These results indicate that the beneficial effect of localised magnetic field is dependent of area of magnetic field as well as location of magnetic field.

Based on this study, a MRE core embedded sandwich beam was shown to be able to achieve adjustable stiffness and damping, which could be applied to design a tunable vibration absorber.

Chapter 8

Applications of MRE as a Propeller Shaft Vibration Absorber

8.1 Introduction

Based on the experiment results and the numerical analyses from previous chapters, MRE core embedded sandwich beam are shown as being able to achieve adjustable stiffness and damping, which can be applied to design tunable vibration absorber. One of potential applications for vibration suppression / minimisation / mitigation is a ship's propeller shaft utilising MRE at its core.

A propeller converts rotational motion into thrust for propulsion of a vehicle, such as a ship or submarine. In a ship, this thrust is generated by an engine which is generally positioned some distance from the propeller. Thus, the propeller shaft has to be long in order to link with the engine to the propeller.

The propeller shaft is held in place by brackets and bearings. As the propeller rotates in a non-uniformly distributed wake near the stern of the ship, the propeller is subject to various loads. As a result, the shaft will vibrate. A vibrating propeller can cause damage to the stern tube bearings and to other parts of the hull and structure. Periodic or nonlinear vibration may cause the misalignment of the propeller shaft fitted in a strut as can be seen at Fig. 8.1. Misaligned shafts may wear a strut and break a bearing. As a result, the shaft must be replaced in severe cases.

So far, many efforts for reducing shaft vibration have been attempted. A pas-

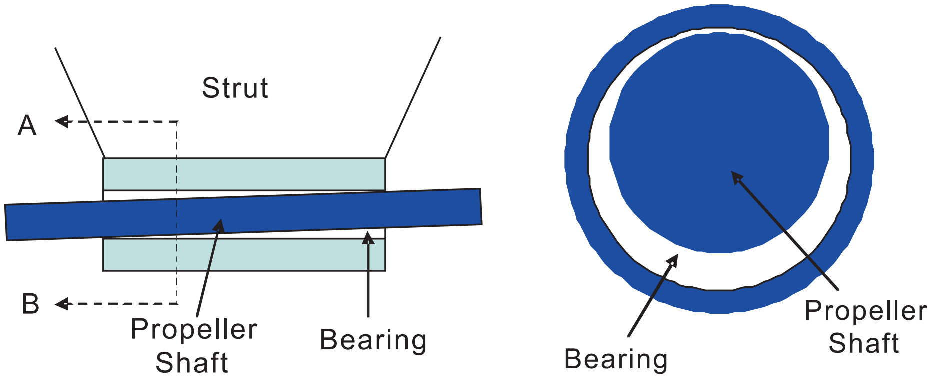

(a) Misalignment of the shaft caused by whirling vibration

(b) Cross section of AB

Figure 8.1: Whirling vibration caused by hydraulic force

sive vibration control scheme was developed by Murayama *et al.* (1992) for a car driving shaft with a new nylon coating to reduce vibration and noise. Many techniques have been evaluated to reduce vibration of propeller shafts such as actively controlled magnetic bearings (Lewis *et al.* , 1989) and active control system consisting of a self-contained pneumatic servo-controller powered by compressed air (Baz *et al.* , 1990b). However an active system is usually very expensive due to the large amount of power required for good performance for large structures such as ship's propellers.

To this end, an MRE vibration absorber for propeller shaft mounted in a ship structure is proposed in this chapter. As presented in the literature, many applications demonstrate that there is potential for the use of MR materials in marine structures as well and therefore the subject is worthy of study by naval architects. In this chapter, the new idea of an MRE vibration absorber for propeller shaft is to change the kinematic boundary condition in the cylindrical direction of the device to adjust MREs stiffness (Choi *et al.* , 2009b). Fig. 8.2 shows the schematic figure of MRE configured propeller shaft vibration absorber. An electro magnetic coil is positioned around the cylindrical support so that when required, a magnetic force could be applied to act on the MREs mechanical properties to improve the structural response of the propeller shaft. The propeller shaft is suspended by a bearing supported by the MRE-steel casing unit winded by coils.

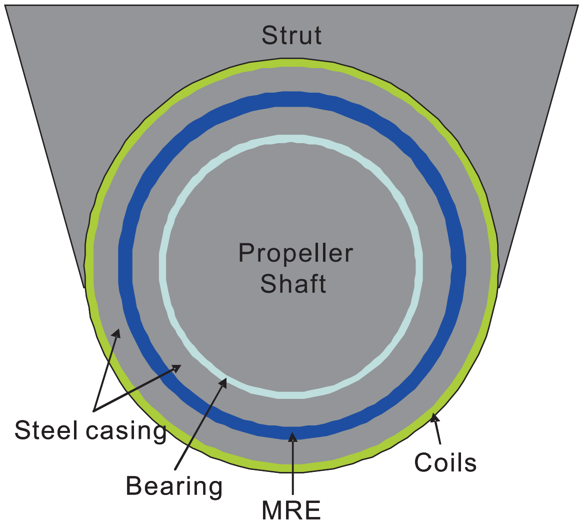

Figure 8.2: Schematic figure of cross section of MRE configured propeller vibration absorber

8.2 Experimental Investigation

8.2.1 The idealised MRE cored shaft

Fig. 8.3 shows simplified model of propeller shaft vibration absorber. One assumption is made that the propeller shaft and the bearing form an integrated system. Magnetic field travels from the coils to inside steel layer through MRE. The magnetic flux is controlled through an electronic feedback circuit. On and off control

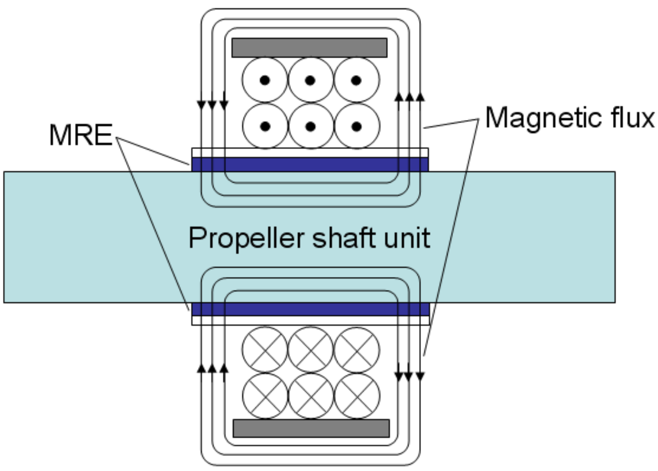

Figure 8.3: Magnetic flux in MRE configured propeller vibration absorber

scheme with electromagnetic field would help to avoid resonant vibration amplitude.

8.2.2 Specimen manufacture

The MRE specimens are a mixture of silicone (Elastosil M4644 A, Wacker Co.), a catalyst (Elastosil M4644 B) and 3-5 micron sized iron powder particles (CIP CC, BASF Co.) (Choi *et al.* , 2008). Fig. 8.4 shows the steel-MRE sandwich configured vibration absorber. The material is injected into the cylindrical steel mould with a syringe, see Fig. 8.4a. The inside of MRE casing is threaded to be able to fit into the steel shaft tightly. The outside steel casing is designed to be fitted inside an electromagnet. The steel mould is then placed in the oven at 80 °C for 12 hrs so that the materials can be cured entirely as can be seen in Fig 8.4b.

(a) The material injection into the mould

(b) Cured MRE casing unit

Figure 8.4: MRE vibration absorber consisting of cylindrical MRE layer in between two steel casings (1. inner steel casing, 2. MRE layer, 3. outer steel casing)

8.2.3 Experimental setup

Based on vibration control mechanism in Fig. 8.3, the experimental setup for the propeller shaft vibration absorber with an electromagnet is shown in Fig. 8.5. The cylindrical shaft is fitted in the electromagnet (Type C, Newport Pagnell England) which can produce about 0.5 Tesla. Due to the limit size of the MRE casing to be fitted in the electromagnet, the length and the diameter of the steel shaft are 400 mm and 18 mm, respectively. The shaft is fixed at two places by electromagnets. Two cylindrical MRE casings are fitted outside the shaft and are placed in the void area of each coil. The cylindrical casing and the inside area of electromagnet are bonded together. A force transducer (PCB 208C01) is fitted to the stinger glued on the middle area of the shaft.

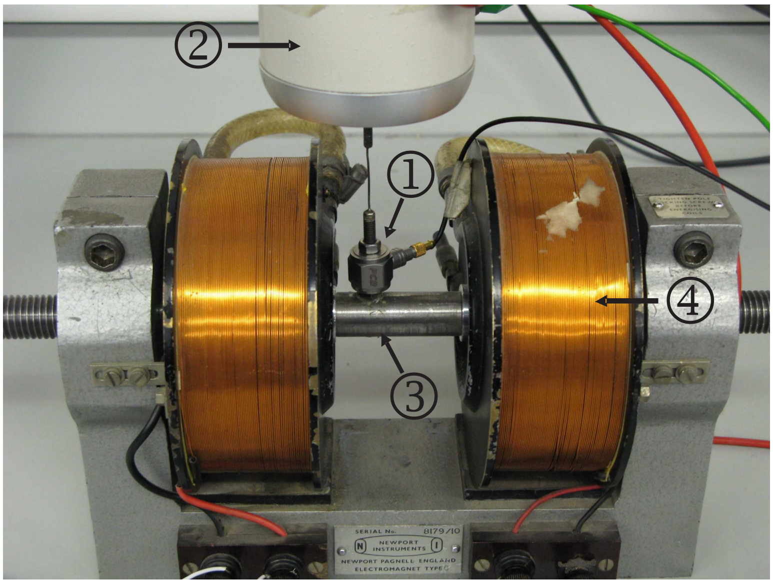

Figure 8.5: Experimental setup for propeller shaft vibration absorber (1. force transducer, 2. shaker, 3. steel shaft, 4. coil)

The accelerometer (PCB 352C22) is attached to the shaft at each measurement point. The generated signal is transferred to the shaker through the amplifier. The shaker is suspended by a soft spring attached to a frame, which the reaction force imposed on the shaker is not transmitted to the test structure (Ewins, 2000). Broadband white noise signals (10-1000 Hz) are generated and measured in-situ. The measurement points of the applied force and acceleration are shown in Fig. 8.6. To better understand vibration characteristics of the shaft, the acceleration points measured are distributed on the shaft. The section between MRE casing (i.e. point '1', '2' and '3') represents the area on the shaft between an engine and a strut of a ship whereas the area outside MRE casing (i.e. point ’4’, ’5’ and ’6’) is assumed to be a free boundary area of the shaft such as outside of a strut or a propeller. It is also important to know how transmitted vibration energy to the structure can be diminished. Thus, the other acceleration point is measured at the outside of the MRE casings (point ’7’). This area is assumed to be a transmitted area from the shaft such as a strut or a ship’s hull.

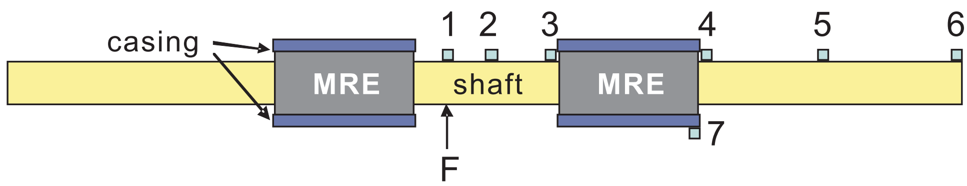

Figure 8.6: The points of force applied and responses measured

8.3 Test Results and Discussions

To better understand the behaviour of the vibration absorber, forced vibration tests are carried out. The purpose of the tests is to present a potential idea of use of MRE as a vibration absorber in a rotational mechanism. The test seeks to compare forced vibration responses with and without magnetic field. In order to acquire a reliable signal, a coherence curve is needed. The coherence curve is a frequency domain measurement of similarity and phase lock between the force and the acceleration signals. The closer the signal is to 1, the fewer disturbances exist during the analysis of the system’s response signal. Two coherence curves are shown in Fig. 8.7. The solid line with dotted mark represents the coherence curve of no magnetic field whereas a solid line with x mark represents that of under magnetic field. Due to the coupling effect between the steel shaft and the electromagnet poor coherence appears in lower frequency ranges (from 10 Hz up to 200 Hz). The coherence curves between nonmagnetic and under a magnetic field show slightly different behaviours until 200 Hz. However, good coherence occurs after 300 Hz to 1000 Hz where the fundamental frequency of the shaft exists and therefore the analyses will be focused in this frequency ranges.

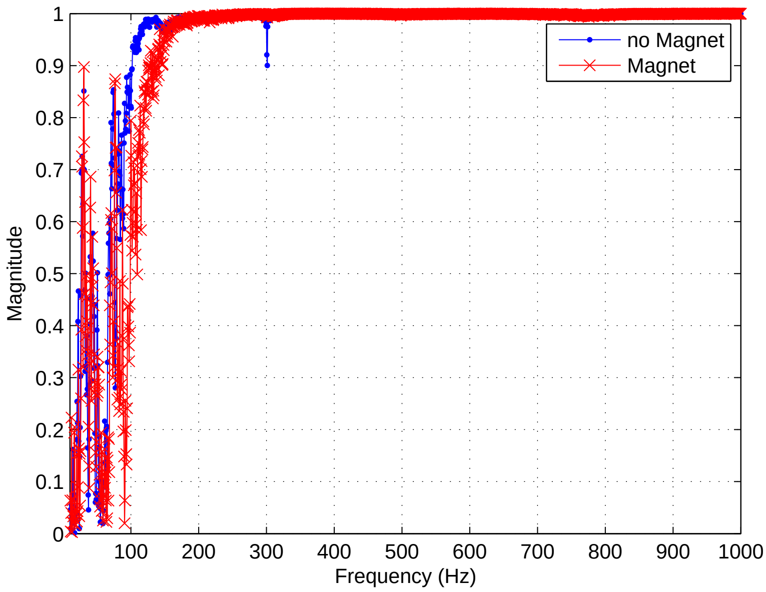

Figure 8.7: Coherence function at point '1'

The transfer accelerance measured inside of MRE layer is shown in Fig. 8.8. This section represents the area on the shaft between an engine and a strut of a ship. Fig. 8.8a shows the point accelerance at point '1' (see Fig. 8.6). The fundamental frequency changes from 426 Hz to 491 Hz by applying a magnetic field. The vibration amplitude reduction is 8.5 dB at the frequency of the resonant peak (426Hz). Fig. 8.8b shows the transfer accelerances measured at the middle of the shaft (point '2'). The pattern of frequency spectrum is similar to the point accelerance at the presence of magnetic field. The vibration amplitude attenuation is 9.9 dB. Fig. 8.8c shows the transfer accelerances measured inside near of MRE layer (point '3'). Vibration amplitude change is about 10.1 dB, which indicate that more than three times amplitude reduction can be achieved.

The transfer accelerance measured outside of MRE layer is shown in Fig. 8.9. This area is assumed to be a free boundary area of the shaft in the real ship structure such as outside of a strut. Fig. 8.9a shows the transfer accelerance measured at outside near of MRE layer (point '4'). A vibration amplitude attenuation of up to 20.6 dB is achieved, which is the most significant vibration reduction. Fig. 8.9b

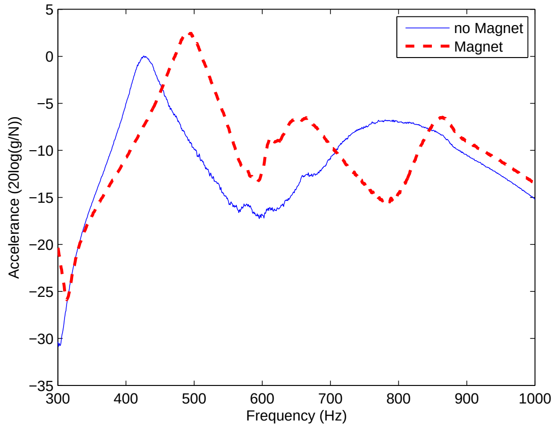

(a) Point '1'

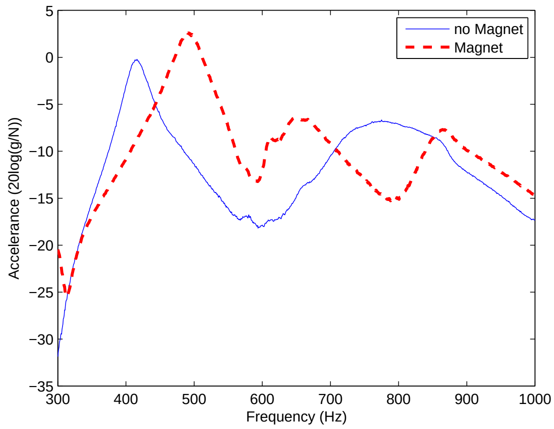

(b) Point '2'

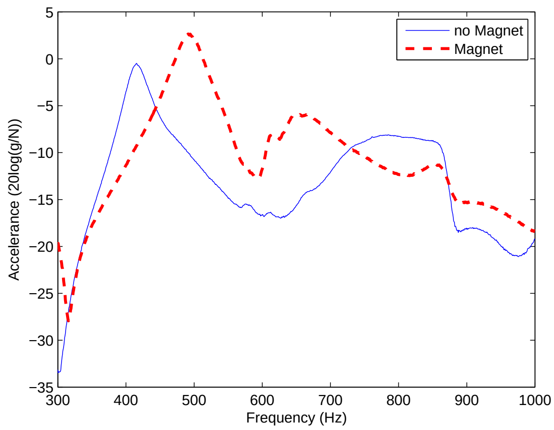

(c) Point '3'

Figure 8.8: Accelerance measured inside of MRE layers

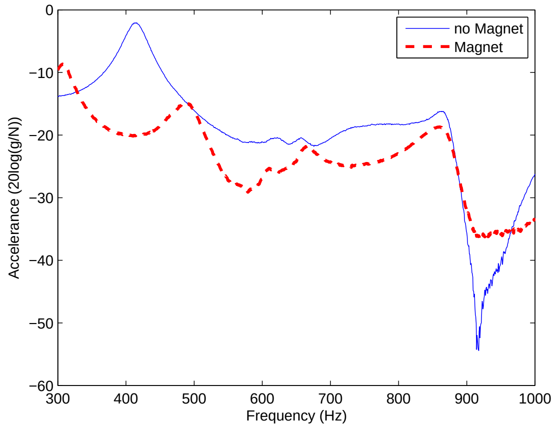

(a) Point '4'

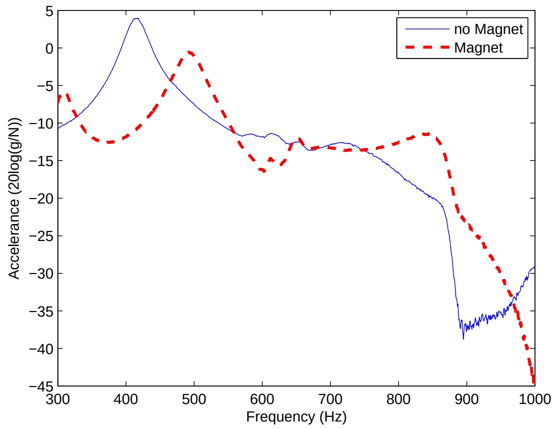

(b) Point '5'

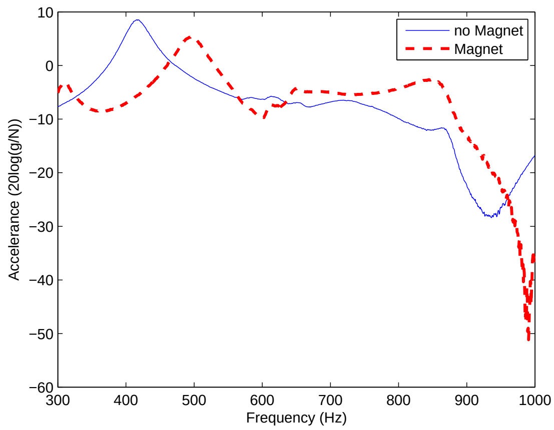

(c) Point '6'

Figure 8.9: Accelerance measured outside of MRE layers

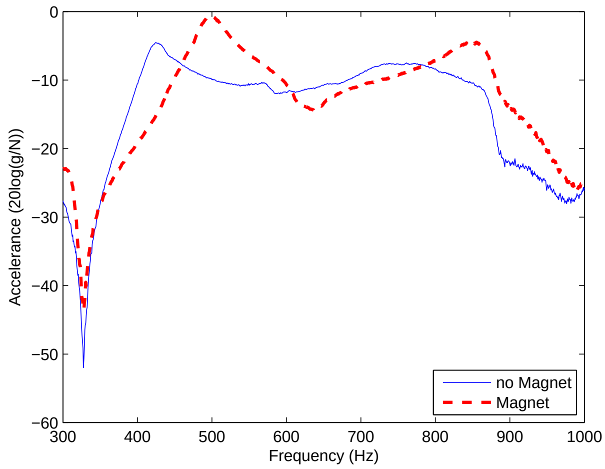

Figure 8.10: Transfer accelerance at outer casing (point '7')

shows the transfer accelerance of point '5'. A vibration amplitude reduction is 16.9 dB. Less vibration attenuation (16.4 dB) can be seen at the end of steel shaft (point '6') is shown in Fig. 8.9c. Compared to the results measured on the area of the shaft between two MRE casings, much more vibration amplitude reduction can be seen outside of the MRE casings. This is because the vibration amplitude is initially high at the free boundary area where the magnetic field does not exist, and therefore the vibration amplitude reduction is much higher in the presence of magnetic field. Considering these results, it can be seen that the MRE layer can reduce the critical shaft vibration amplitude.

Fig. 8.10 shows the transfer accelerance measured outside of MRE casings (point '7'). This area is assumed to be a transmitted area from the shaft such as a strut or a ship structure. Vibration amplitude reduction is 12 dB. This is meaningful results that transmitted vibration amplitude which may affect the journal bearing can be reduced significantly in the real ship structure.

8.4 Numerical Simulations

8.4.1 Validation

Since the experimental setup consists of the electromagnetic unit, MRE vibration absorber and the steel shaft, dynamic characteristics of the shaft needs to be evaluated from frequency spectrum of coupled system. To understand dynamic behaviour of the shaft a simplified finite element (FE) model has been created. FE analysis using ABAQUS/Explicit (ABAQUS, 2007) predicts a fundamental vibration response of a propeller shaft which might be coupled with electromagnet structure in the experiment.

The length and the diameter of the steel shaft are 400 mm and 18 mm, respectively as in the experiment. The length and the thickness of each cylindrical MRE layer are 55 mm and 4 mm, respectively. Each of MRE layer is located 40 mm from the centre of the shaft. Model is defined by 8073 nodes and 6528 of 3D eight nodes cubic elements (C3D8), see Fig. 8.11. The material property of the MRE layer is based on test results presented in Chapter 4. Elastic modulus of steel shaft and MRE are 210 GPa and 4 MPa (12 MPa when a saturated magnetic field applied), respectively. Due to its rubber like behaviour, the Poisson's ratio of MRE is assumed to be 0.49 (Ferry, 1980). In order to investigate frequency shift only, material damping of MRE is not considered. The density of the steel shaft and MRE are 7,800 kg/m^3 and 2,900 kg/m^3, respectively. The boundary condition the most resembling that in the test rig is when the outside surface of the MRE layer is fixed. Therefore, the nodes outside of MRE solid elements are fixed regarding as rigid boundary. The Lanczos eigensolver, an adaptation of power methods to find eigenvalues and eigenvectors of a square matrix, provided by ABAQUS is used to compute the natural frequencies and corresponding mode shapes of the steel shaft. Steady state analyses are carried out from 0 to 1000 Hz by 1Hz. The force is applied at 7.5 mm left of centre of the shaft where is the exact same point as used in experiment and the accelerances are measured at the other side of point '1' and point '6', see Fig. 8.6.

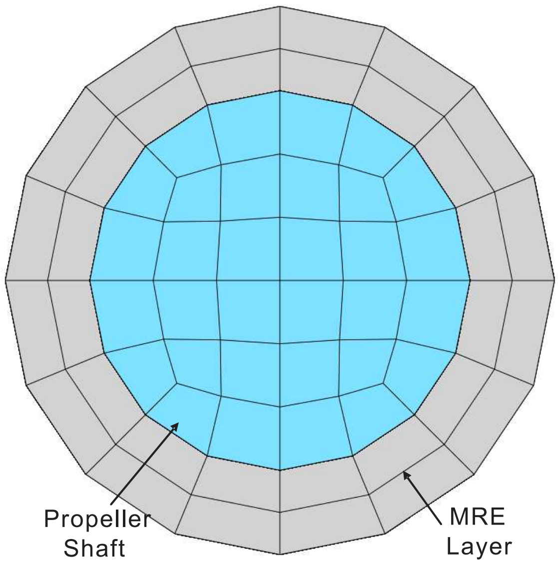

Figure 8.11: Cross section of FEA elements

Fig. 8.12 shows the point and transfer accelerances at two points with and without magnetic field. Both resonant peaks change from 431 Hz to 486 Hz. In this frequency area, the most significant resonant peaks appeared in the experiment results, see Fig. 8.8a and Fig. 8.9c. The amplitude of the resonant peaks at the end of the shaft are higher than those of point accelerances as shown in Fig. 8.12b.

The mode shapes of the shaft without magnetic field are shown in Fig. 8.13. Since the deformation scale factor is 10, the amplitudes of vibration modes can be seen exaggeratedly. The blue elements represent the shaft and the gray elements represent the MRE casing. The first five vibration modes of the shaft corresponds frequency responses as described in Fig. 8.12a. Rigid body motion of the shaft is shown at first mode. Bending mode occurs at 431 Hz which contributes to significant resonant peak. However, there are no more resonant peaks until 1000 Hz. Fig. 8.14 shows vibration modes of the shaft corresponding frequency response under magnetic field. The change of mode shape and frequency can be seen due to MRE with a magnetic field. Corresponding mode of the resonant peak occurs at 486 Hz is the bending mode. However, rigid body mode of the shaft arises at second mode. From these two results, most significant resonant peaks of the shaft occur

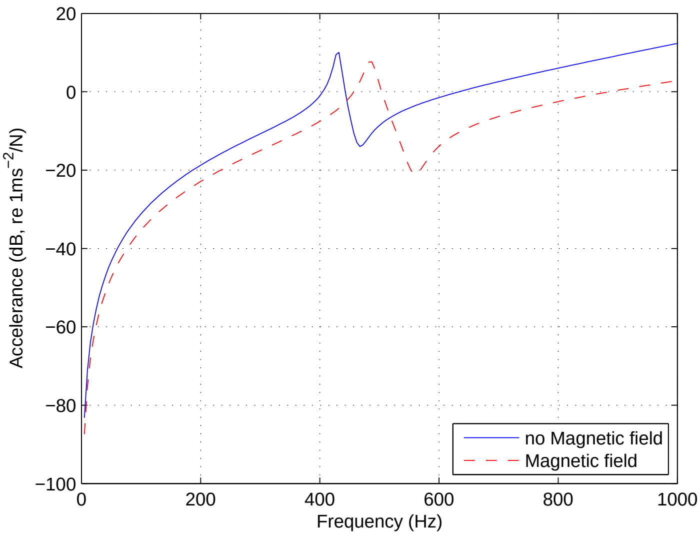

(a) Point accelerance (point ′1′)

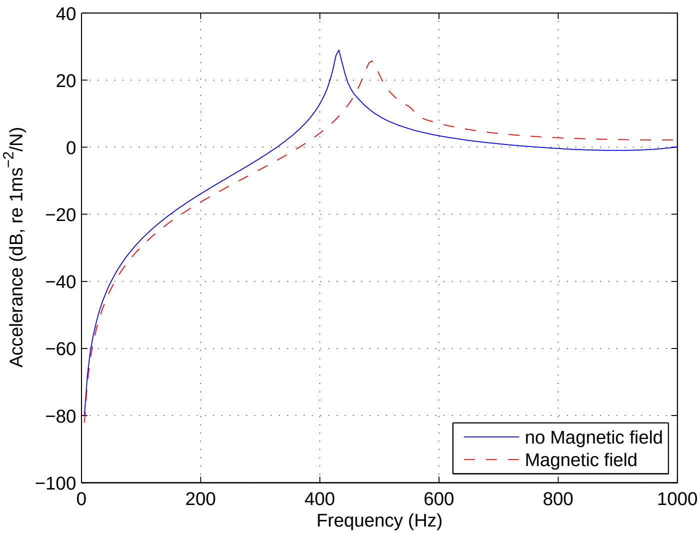

(b) Transfer accelerance at shaft end (point ′6′)

Figure 8.12: Frequency response curves on the shaft

(a) 1^{st} mode (282 Hz)

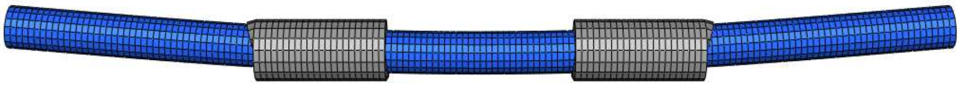

(b) 2^{nd} mode (431 Hz)

(c) 3^{rd} mode (453 Hz)

(d) 4^{th} mode (458 Hz)

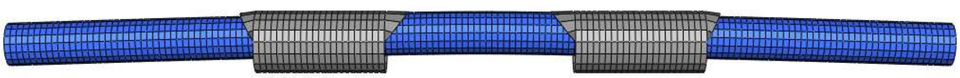

(e) 5^{th} mode (1295 Hz)

Figure 8.13: FEA results of vibration modes of the shaft without magnetic field

(a) 1^{st} mode (486 Hz)

(b) 2^{nd} mode (489 Hz)

(c) 3^{rd} mode (555 Hz)

(d) 4^{th} mode (783 Hz)

(e) 5^{th} mode (2087 Hz)

Figure 8.14: FEA results of vibration modes of the shaft with magnetic field

from bending mode. These results match very well with test results that the most significant resonant peaks appeared in this frequency ranges as shown in Fig. 8.8a and Fig. 8.9c.

8.4.2 Parametric study in terms of different MRE casing configuration

The purpose of the parametric study is to understand how much vibration energy is dissipated by employing an MRE casing in large scale shaft with and without magnetic control. Forced vibration responses of four different cases with different topologies of MRE layers are compared. To investigate better the significant change of frequency response in each case, steady state analyses are carried out from 0 to 1000 Hz by 1Hz, which represents from mechanical vibration to audible frequency ranges. In order to investigate a number of responding modes of the steel shaft, bigger dimensions of elements than those of the experiment are used. The length and the diameter of the shaft are 400 cm and 18 cm, respectively, which are also probable dimensions of the large scale structure. Four different cases by varying length and thickness of MRE layer are varied as shown in Table 8.1. Each of MRE layer is located 40 cm of centre of the shaft at equal distance. The force is applied at 7.5 cm left of centre of the shaft. For numerical comparison, the reference length (L_{ref}) and the thickness (d_{ref}) of each MRE layer are 27.5 cm and 2 cm, where L and d are the length and the thickness of each MRE layer, respectively. The properties of the elements are the same as those used in the previous section.

Case 1 (L / L_{ref} = 1, d / d_{ref} = 1)

Fig 8.15 shows the comparison of frequency responses at case 1 as described in Table 8.1. The characteristics of two curves are shown differently at lower frequency ranges. Even resonant peak without magnetic field is bigger than that under magnetic field at first mode in both cases. Dominant resonant peaks arise at 183 Hz and 272 Hz without magnetic field while the resonant peak disappears around 200 Hz under the magnetic field. This is due to the change of vibration mode shape as

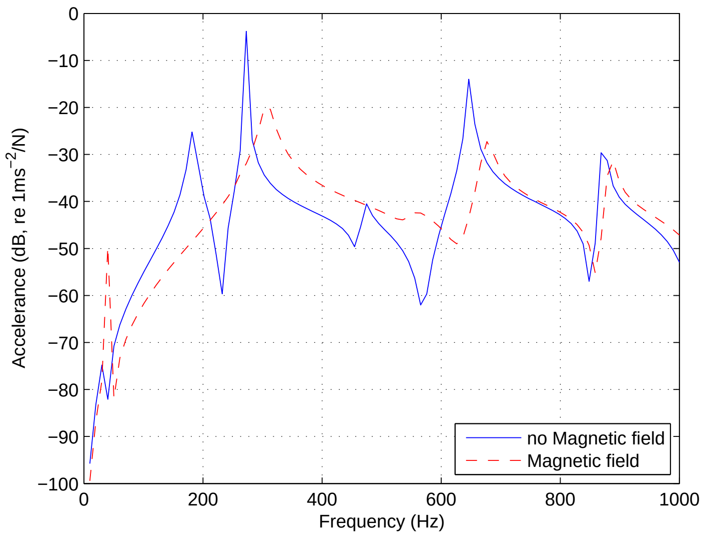

(a) Point accelerance (point '1')

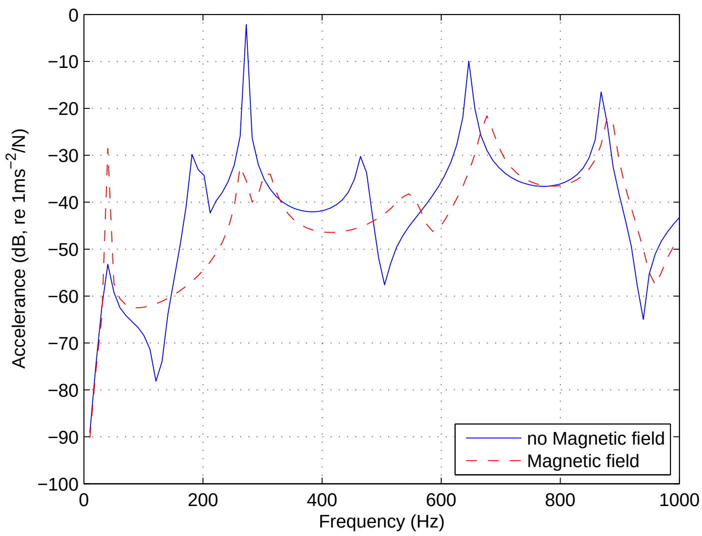

(b) Transfer accelerance at shaft end (point '6')

Figure 8.15: FEA prediction of the point accelerance at first case

(a) 1^{st} mode (27 Hz)

(b) 2^{nd} mode (38 Hz)

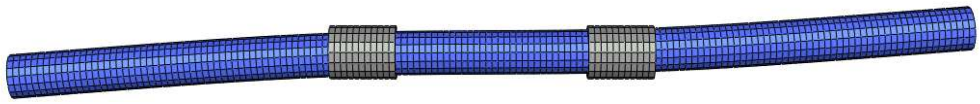

(c) 3^{rd} mode (40 Hz)

(d) 4^{th} mode (41 Hz)

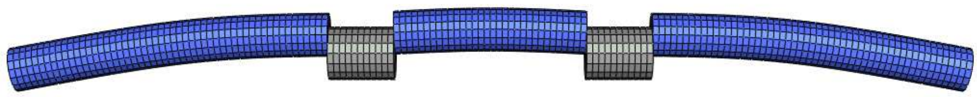

(e) 5^{th} mode (183 Hz)

(f) 6^{th} mode (206 Hz)

(g) 7^{th} mode (272 Hz)

(h) 8^{th} mode (386 Hz)

Figure 8.16: FEA results of vibration modes of the shaft without magnetic field at case 1

(a) Deformed shaft at 1^{st} mode (41 Hz)

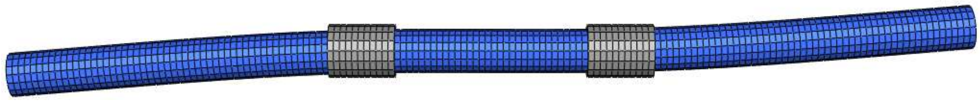

(b) Deformed shaft at 2^{nd} mode (46 Hz)

(c) Deformed shaft at 3^{rd} mode (47 Hz)

(d) Deformed shaft at 4^{th} mode (71 Hz)

(e) Deformed shaft at 5^{th} mode (262 Hz)

(f) Deformed shaft at 6^{th} mode (266 Hz)

(g) Deformed shaft at 7^{th} mode (308 Hz)

(h) Deformed shaft at 8^{th} mode (387 Hz)

Figure 8.17: FEA results of vibration modes of the shaft with magnetic field at case 1

Table 8.1: Different cases of MRE layer

	L/L_{ref}	d/d_{ref}
Case 1	1	1
Case 2	1	2
Case 3	2	1
Case 4	2	2

stiffened MRE changes boundary conditions of the shaft. As the frequency ranges increase, the frequency differences between two curves decrease. This is because the property of the MRE is much smaller than that of the steel shaft, and therefore the frequency change is no more effective in high frequency ranges. However damping effects are shown in both cases.

Fig 8.16 shows corresponding free vibration modes of the shaft without magnetic field at first case. A rigid body vibration mode of the shaft is shown at first mode, which causes less resonant peak as shown in Fig. 8.15a. Mostly bending vibration modes appear except the 4th mode and the 8th mode. Combined bending and whirling vibration mode appears at fifth mode (183 Hz). Fig 8.17 shows free vibration modes of the steel shaft under the magnetic field at first case. Compared to the mode shapes without magnetic field, different mode shapes are shown. Combined bending and whirling vibration mode disappears whereas this was shown at fifth mode without magnetic field. This is also due to stiffened MRE layer as mentioned above in Fig. 8.15.

Case 2 (L / L_{ref} = 1, d / d_{ref} = 2)

Fig 8.18 shows the comparison of frequency responses at second case. Compared to the first case, the thickness of MRE layer is twice the thickness of the reference layer. The fundamental frequency changes from 101 Hz to 151 Hz (50 %) in respond to the magnetic field in both point and transfer accelerances. Large

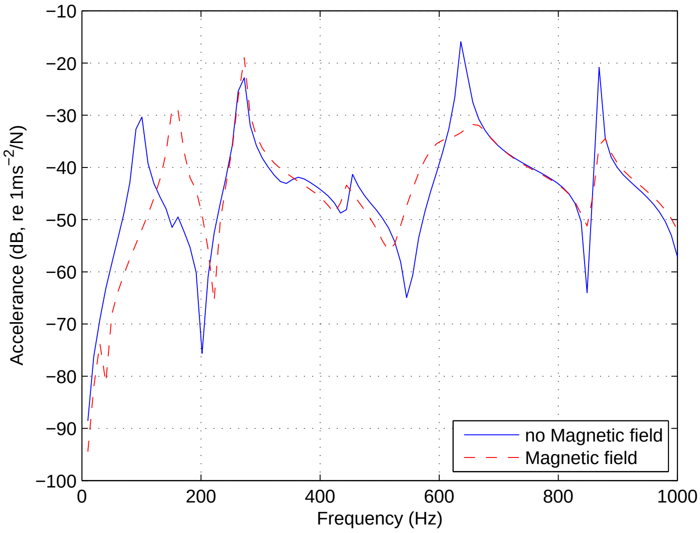

(a) Point accelerance (point ′1′)

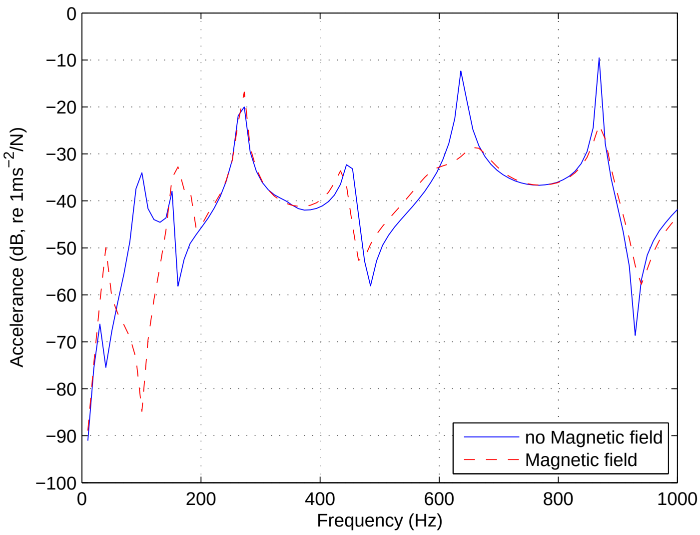

(b) Transfer accelerance at shaft end (point ′6′)

Figure 8.18: FEA prediction of the point accelerance at second case

amount of damping effect arise at higher frequency ranges. This indicates that frequency changes are shown at lower frequency ranges whereas damping changes are shown at higher frequency ranges (after 600 Hz).

Case 3 (L / L_{ref} = 2, d / d_{ref} = 1)

Fig 8.19 shows the result at third case. Only the length of MRE layer is twice the length of the reference layer. Compared to previous two results, the number of resonant peaks drastically reduces. Higher damping effects are shown overall frequency ranges. The fundamental frequency changes from 51 Hz to 61 Hz (20 %) at both points in respond to the magnetic field. The second resonant peak shifts from 220 Hz to 303 Hz (36 %), see Fig 8.19a. However these resonant peaks disappear in transfer accelerance at the end of the shaft (point ’6’). Both frequency shift and damping change can be seen at higher modes as well.

Case 4 (L / L_{ref} = 2, d / d_{ref} = 2)

Fig 8.20 shows the result at fourth case. Both the length and the thickness of MRE layer are twice those of the reference layer. The fundamental frequency changes from 40 Hz to 50 Hz (25 %). The second resonant peak shifts from 131 Hz to 212 Hz (61 %). In transfer accelerance of the point ’6’, two large resonant peaks from 100 Hz to 200 Hz disappear when magnetic field applies, see Fig 8.19b. Interestingly, less frequency shifts are shown than those in case 3 at higher modes from 600 Hz to 1000 Hz. This indicates that large amount of MRE layer does not guarantee the good MR performance.

Overall, it is shown that dimension of MRE layer can change vibration controllability characteristics of the shaft. It is worth to know that the size of MRE layer affect to control selective frequency ranges effectively. Improved MR performance can be seen with even small amount of area of MRE layer.

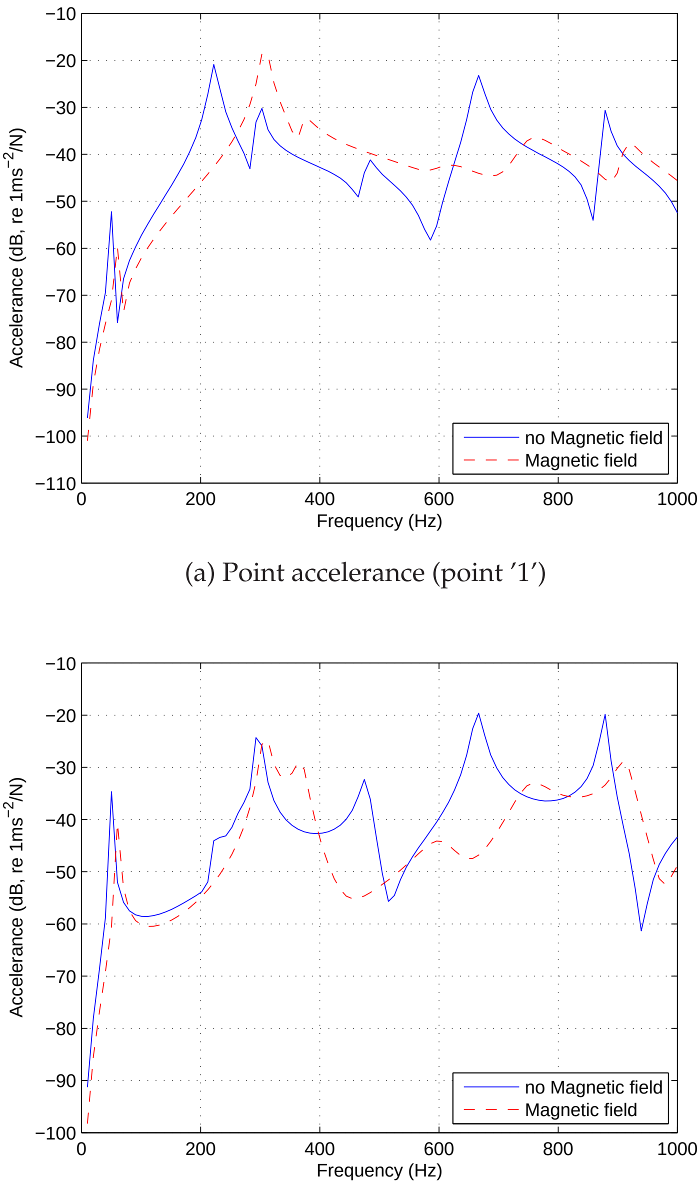

(a) Point accelerance (point '1')

(b) Transfer accelerance at shaft end (point '6')

Figure 8.19: FEA prediction of the point accelerance at third case

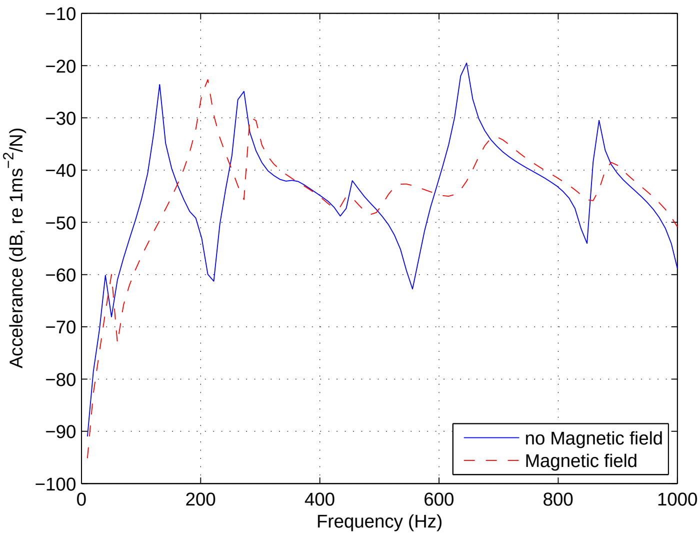

(a) Point accelerance (point ′1′)

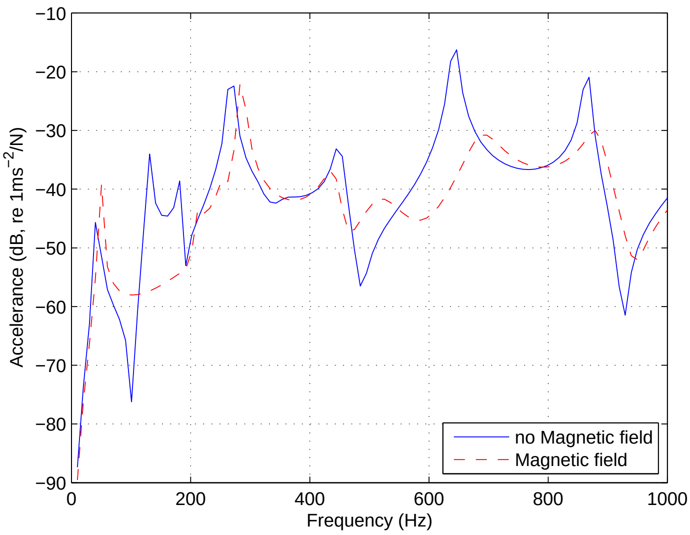

(b) Transfer accelerance at shaft end (point ′6′)

Figure 8.20: FEA prediction of the point accelerance at fourth case

8.5 Conclusions

An experimental study is carried out to illustrate the control capabilities of MRE adaptive vibration absorber for a propeller shaft in real time. It is observed that the vibration amplitudes at fundamental frequency ranges are significantly reduced by applying a magnetic field. Due to property change capability of MRE, a 20% of frequency shift occurs. The largest vibration amplitude reduction was observed about 20 dB, but mostly about 10 dB of vibration reduction were shown. That is to say, MRE absorber can reduce vibration amplitude of the shaft as well as outside of the shaft such as the bearing, the strut and so on. If the MRE specimen is cured under a magnetic field optimally, the effects would be stronger than these results presented in this chapter.

In numerical study, the results agreed well with the experimental results. Frequency response analyses with various size of MRE layer are carried out. It was shown that even small amount of MRE layer, large frequency change can be acquired. These results give a guideline of how to design MRE vibration absorber isolation system in conjunction with an adaptive passive control system.

Overall, this new idea could potentially be used in car industry, marine, and other application where rotating shafts are used to transmit power from the source to the application / delivery location such as a car transmission system and a wind turbine system (Choi *et al.* , 2009b).

Chapter 9

Power Flow Analysis for a Floating Sandwich Raft Isolation System Using a Higher Order Theory

9.1 Introduction

An MRE configured sandwich beam structure was shown to be an adjustable vibration absorber, experimentally in Chapter 6 and numerically in Chapter 7. The potential application of cylindrical sandwich configured MRE as controllable vibration absorber for a propeller shaft was shown in Chapter 8. In this chapter, another possible application of smart sandwich structure is presented as adjustable structure in a floating raft vibration isolation system. The aim is to create the possibility of smart sandwich beam as a floating raft which can control vibration transmission from the machinery to the base structure. To achieve this, it is proposed to model power flow analysis (PFA) based on modal analysis by aid of higher-order sandwich beam theory. Furthermore, case studies of how various topologies of sandwich floating raft can be affected to vibration isolation systems are presented.

9.2 Literature Review on Power Flow Analysis

Power flow analysis (PFA) approaches have been used to predict dynamic characteristics of coupled systems composed of various subsystems. The fundamental concept of power flow is discussed by Goyder & White (1980) and Pinnington &

White (1981). In recent years, this approach has been developed and applied to model complex structure (Clarkson, 1991; Cuschieri, 1990; Hussein & Hunt, 2006; Jenkins *et al.* , 1993; Langley, 1990; Li *et al.* , 1997; Xiong, 1996; Xiong & Song, 1996; Xiong *et al.* , 2001, 2002) and to assess passive, active and vibration control system (Miller *et al.* , 1990; Pan *et al.* , 1992; Xiong, 1996; Xiong *et al.* , 2000, 2003, 2005). Langley (1990) presented the dynamic stiffness method to investigate forced vibration of a row of stiffened rectangular panels, simply supported along the longitudinal edges. Clarkson (1991) applied the receptance method to investigate the transmission of vibrational energy across structural joints of connected beams and connected plates. Cuschieri (1990) used a mobility method to analyze the power flow in periodically connected beams and L-plates subject to a single excitation. Hussein & Hunt (2006) applied the mean power flow method to evaluate the effectiveness of vibration countermeasures of an underground tunnel model which consisted of Euler-Bernoulli beams to account for the rails and the track slab. For complex structures, finite element analysis (FEA) is often used to analyze dynamic behaviours with good accuracy in low frequency range. Jenkins *et al.* (1993) used a finite element model to demonstrate the detailed dynamics of a typical raft-isolation-receiver system using secondary force inputs in parallel with a passive isolation system. They showed that a combined active/passive isolation system is more effective than a passive isolation system at low frequencies. Qu & Selvam (2002) developed dynamic condensation to reduce the number of degrees of freedom (DOF) of finite element models for a damped system. However FEA schemes are usually computationally expensive because of relatively large number of DOF needed to capture the shorter wavelengths of vibration. Thus, it is difficult to analyze problem with high frequency ranges.

The frequency response function method is more suitable to a system consisting of only two subsystems. However as the number of subsystems increases so the computational effort increases. The four-pole parameters method (Molly, 1957; Snowdon, 1971) is a classical technique for deriving dynamic characteristics of an assembled system connected in series or in parallel. This is convenient when considering a series of dynamical elements connected end-to-end. However, it is limited to single-input / single-output (SISO) linear mechanical systems. The four-pole parameters method was extended to multiple-input / multiple-output (MIMO) linear systems considering coupling interactions by Ha & Kim (1995) to predict the frequency response characteristics and by Xiong (1996) to estimate power flow transmission mechanisms.

PFA has become widely used to predict vibrational power flows through various kinds of assembled structures. Xiong & Song (1996) investigated power flow in a flexible floating raft isolation system using the substructure mobility synthesis method. For a generic coupled system consisting of any number of substructures, Xiong *et al.* (2001) developed progressive approaches to PFA and applied them to a complex coupled floating raft vibration isolation system. Generalised mobility/impedance matrix formulations of each substructure were derived allowing the construction of equivalent mobility and equivalent impedance matrices to describe the dynamic behaviour of a substructure assembled from several interconnected substructures within the overall system. Application examples showed that an increase in dynamic stiffness of the raft reduces the vibrating power transmitted from the machinery via the raft to the flexible foundation.

A sandwich type floating raft system offers the advantage that the whole system is much lighter in addition to reducing vibration and noise (Vikal *et al.* , 1981). Sandwich configurations are used where high stiffness / weight and strength / weight ratios are required. The flexural stiffness of a sandwich beam is proportional to $d^2h/4$, where d and h are the thickness of the core material and skin respectively. Due to the high stiffness/weight which results in a higher natural frequency, the number of responding modes is drastically reduced (Mead, 2000). Another advantage of using a sandwich configuration is that power flow levels tend to reduce as the viscoelasticity level of the core material increases (Xiong *et al.* , 2002). Investigation on an active vibration control of energy flow from a machine transmitted to equipment, both mounted on a simply supported PVC sandwich panel, showed that increasing damping ratio of the core material of the sandwich panel reduces the resonant peaks of power flow transmission spectra to the equipment (Xiong *et al.* , 2002). Sandwich structures with viscoelastic cores such as PVC that have relatively high ratios of energy dissipation to energy storage capability have been used in a variety of structural engineering applications where damping is required to dissipate energy (Meunier & Shenoi, 2001).

Analytical models for sandwich structures have been studied using classical sandwich theory (Allen, 1969), first shear deformation theory (Whitney & Pagano, 1970), elastic foundation model (Zenkert, 1997) and various higher order models where the higher order terms are defined at the neutral axis (Reddy, 1999). However, these models have a drawback when sandwich structures are thick, the ratio of the transverse shear modulus to in-plane is low, and the ratio of longitudinal to transverse Young's moduli is high (Hu *et al.* , 2008). The characterization of sandwich structure with soft cores need to be simulated with the aid of an enhanced theory that can constitute its vertical flexibility which affects stress and displacement fields in the face sheets and influences nonlinear displacement patterns along the height of the core (Sokolinsky *et al.* , 2002). Most recently developed higher-order sandwich panel theory (HSAPT) (Frostig *et al.* , 1992) has shown the accuracy of predicted stress, localised effect and eigenvalue problems and validated by experimental results (Sokolinsky *et al.* , 2002, 2004).

Vikal *et al.* (1981) investigated effective vibration isolation by the use of an excitation system supported flexibly on a three layer sandwich beam. However, this was analyzed separately as a continuous system by a lumped mass supported on a spring and dash-pot. Li *et al.* (1997) studied power flow via a floating raft consisting of a three layer sandwich beam connected to two sandwich foundation beams of the same type. However, higher order effects owing to the nonlinear displacement pattern of the core material were not considered. Since the flexibility affects internal resultants in skins, peeling and shear stresses in the core (Allen, 1969; Plantema, 1966), the transverse shear interaction between skins and core material is also an important factor in the vibration response of a sandwich beam with a soft core, which induces the damping for sandwich structure with viscoelastic cores (Hu *et al.* , 2008).

In this chapter, the higher-order sandwich beam theory is implemented in conjunction with progressive approaches of PFA to determine power flows in a sandwich configured floating raft vibration isolation system.

9.3 Application of Power Flow Progressive Method

The equivalent mobility based power flow progressive approach (Xiong *et al.* , 2001) is applied. The general coupled system consisting of each substructure S_1, S_2, ..., S_i, ..., S_n is shown in Fig. 9.1.

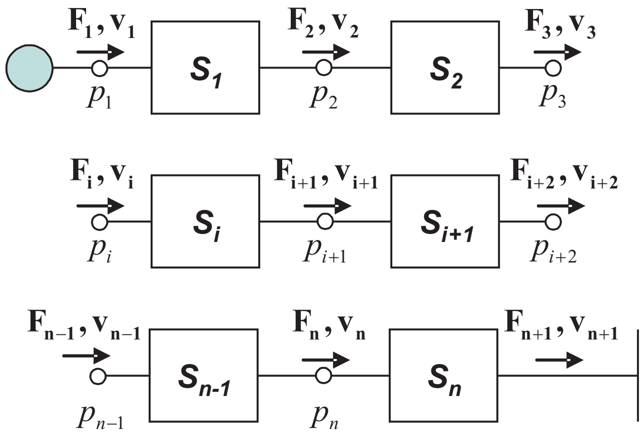

Figure 9.1: Schematic illustration of the coupled systems with n substructures

The power flow transmitted into any substructure is given by

$$P_i = \frac{1}{2}\text{Re}\left\{\mathbf{F}_i^H \cdot \mathbf{v}_i\right\}, i = 1, 2, ..., n. \tag{9.1}$$

where P_i denotes the power flow through any interface of the ith substructure,

H the Hermitian transpose, the force vectors ($\mathbf{F}_i$) and velocity response vectors ($\mathbf{v}_i$) are determined by the following progressive formulations (Choi *et al.* , 2009a; Xiong *et al.* , 2001).

$$\begin{aligned}
\mathbf{v}_i &= \mathbf{A}_i^e \cdot \mathbf{F}_i + \mathbf{N}_i^v \cdot \hat{\mathbf{v}}_{n+1}, \\
\mathbf{F}_{i+1} &= \left[\mathbf{A}_{i+1}^e - \mathbf{A}_i^{22}\right]^{-1} \cdot \mathbf{A}_i^{21} \cdot \mathbf{F}_i + \left[\mathbf{A}_i^{22} - \mathbf{A}_{i+1}^e\right]^{-1} \cdot \mathbf{N}_{i+1}^v \cdot \hat{\mathbf{v}}_{n+1}, \\
\mathbf{A}_i^e &= \mathbf{A}_i^{11} - \mathbf{A}_i^{12} \cdot \left[\mathbf{A}_i^{22} - \mathbf{A}_{i+1}^e\right]^{-1} \cdot \mathbf{A}_i^{21}, \\
\mathbf{N}_i^v &= \mathbf{A}_i^v \cdot \mathbf{A}_{i+1}^v ... \mathbf{A}_n^v, \\
\mathbf{A}_i^v &= \mathbf{A}_i^{12} \cdot \left[\mathbf{A}_i^{22} - \mathbf{A}_{i+1}^e\right]^{-1}, (i = 1, 2, .., n), \\
\mathbf{A}_{n+1}^e &= \mathbf{0},
\end{aligned} \tag{9.2}$$

where $\mathbf{A}_i^e$ is the equivalent mobility matrix of substructure S_i coupled to subsystems $S_{i+1}, ...S_n(i = 1, 2, .., n)$ and $\mathbf{N}_i^v$ is the velocity transmissibility matrix which represents the velocity response vector $\mathbf{v}_i$ produced by a unit velocity input $\hat{\mathbf{v}}_{n+1}$, and it reflects the effect of the boundary motion excitations $\hat{\mathbf{v}}_{n+1}$ upon substructure $S_i(i = 1, 2, ..., n)$.

A floating sandwich raft isolation system as shown in Fig. 9.2 comprising : (1) rigid masses (m_1, m_2) representing the source of vibration such as machinery, e.g. substructure S_1; (2) viscoelastic isolators, e.g. substructure S_2 and S_4; (3) a sandwich floating raft, e.g. substructure S_3; and (4) a sandwich beam base structure, e.g. substructure S_5, where c_1 and c_2 are centres of rigid masses and b_i (i=1, 2, 3, 4) is a horizontal distance between centre of mass and isolators in substructure 2, respectively.

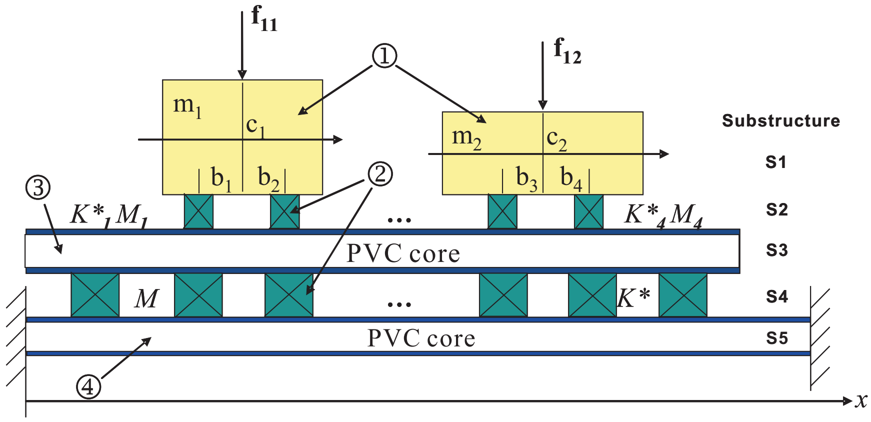

Figure 9.2: Floating sandwich raft vibration isolation system (1. rigid mass, 2. isolators, 3. sandwich floating raft, 4. sandwich base structure)

For substructure S_1, with two inputs and four outputs of the two rigid masses, it is assumed that each mass is supported by two isolators which behave in a passive way, and that motion takes place only in the vertical direction. The generalized mobility matrix $\mathbf{A}_1$ is as follows,

$$\left\{ \begin{array}{c} \mathbf{v}_1 \\ \mathbf{v}_2 \end{array} \right\} = \left[\begin{array}{cc} \mathbf{A}_1^{11} & \mathbf{A}_1^{12} \\ \mathbf{A}_1^{21} & \mathbf{A}_1^{22} \end{array} \right] \cdot \left\{ \begin{array}{c} \mathbf{F}_1 \\ \mathbf{F}_2 \end{array} \right\} \tag{9.3}$$

where $\mathbf{F}_1$ is the prescribed excitation force and the sub-matrices of matrix $\mathbf{A}_1$ are given by

$$\mathbf{A}_1^{11} = \frac{1}{j\omega} \left[\begin{array}{cc} 1/m_1 & 0 \\ 0 & 1/m_2 \end{array} \right], \tag{9.4}$$

$$\mathbf{A}_1^{12} = \frac{1}{j\omega} \left[\begin{array}{cccc} 1/m_1 & 1/m_1 & 0 & 0 \\ 0 & 0 & 1/m_2 & 1/m_2 \end{array} \right], \mathbf{A}_1^{21} = [\mathbf{A}_1^{12}]^T, \tag{9.5}$$

$$\mathbf{A}_1^{22} = \frac{1}{j\omega}\begin{bmatrix} \begin{bmatrix} \frac{1}{m_1}+\frac{b_1^2}{J_1} & \frac{1}{m_1}-\frac{b_1b_2}{J_1} \\ \frac{1}{m_1}-\frac{b_1b_2}{J_1} & \frac{1}{m_1}+\frac{b_1^2}{J_1} \end{bmatrix} & \mathbf{0}_{2\times 2} \\ \mathbf{0}_{2\times 2} & \begin{bmatrix} \frac{1}{m_2}+\frac{b_3^2}{J_2} & \frac{1}{m_2}-\frac{b_3b_4}{J_2} \\ \frac{1}{m_2}-\frac{b_3b_4}{J_2} & \frac{1}{m_2}+\frac{b_3^2}{J_2} \end{bmatrix} \end{bmatrix}. \tag{9.6}$$

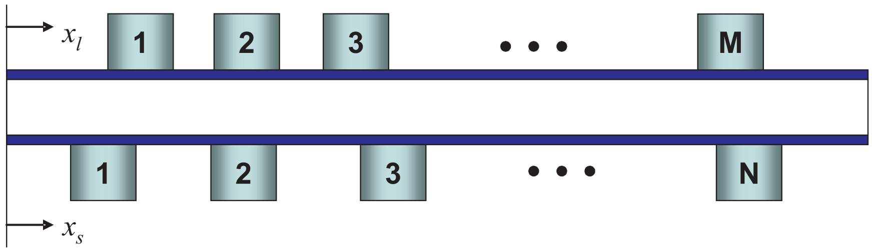

Figure 9.3: Schematic figure to express mobility matrix and normal mode functions at each skin of sandwich beam

Fig. 9.3 shows the sandwich beam (S_3) which is the floating raft as shown in Fig. 9.2. For the isolator substructure S_2 consisting of M identical isolators, the generalized mobility matrix $\mathbf{A}_2$ is presented by

$$\mathbf{A}_2^{11} = \text{diag}\left[\frac{1}{j\omega M_l}+\frac{j\omega}{2K_l^*}\right]_{M\times M}, \tag{9.7}$$

$$\mathbf{A}_2^{12} = \text{diag}\left[\frac{1}{j\omega M_l}\right]_{M\times M} = \mathbf{A}_2^{21}, \tag{9.8}$$

$$\mathbf{A}_2^{22} = \mathbf{A}_2^{11}, \tag{9.9}$$

where M_l is the mass of each isolator. Similarly, for the isolator substructure S_4 consisting of N identical isolators shown in Fig. 9.3, the generalized mobility matrix $\mathbf{A}_4$ is presented by

$$\mathbf{A}_4^{11} = \mathrm{diag}\left[\frac{1}{j\omega M_s} + \frac{j\omega}{2K_s^*}\right]_{N\times N}, \tag{9.10}$$

$$\mathbf{A}_4^{12} = \mathrm{diag}\left[\frac{1}{j\omega M_s}\right]_{N\times N} = \mathbf{A}_4^{21}, \tag{9.11}$$

$$\mathbf{A}_4^{22} = \mathbf{A}_4^{11}, \tag{9.12}$$

where M_s is the mass of each isolator. For the flexible raft structure S_3, the mobility matrix $\mathbf{A}_3$ can be derived by using a modal analysis method as follows,

$$\mathbf{A}_3^{11} = [\chi_{ls}(x_l^{(3)}, x_s^{(3)})]_{M\times M}, \tag{9.13}$$

$$\mathbf{A}_3^{12} = [\chi_{ls}(x_l^{(3)}, x_s^{(4)})]_{M\times N}, \tag{9.14}$$

$$\mathbf{A}_3^{21} = [\chi_{ls}(x_l^{(4)}, x_s^{(3)})]_{N\times M}, \tag{9.15}$$

$$\mathbf{A}_3^{22} = [\chi_{ls}(x_l^{(4)}, x_s^{(4)})]_{N\times N}, \tag{9.16}$$

where $x_l (l = 1, 2, 3, ..., M)$ are the positional co-ordinates of the isolators in the substructure S_2 mounted between the rigid masses and the top skin of the sandwich floating raft in the substructure S_3, and $x_s (s = 1, 2, 3, ..., N)$ denote the positional coordinates of the substructure S_4 mounted between the sandwich floating raft and the sandwich base structure. Here, the components of the mobility matrix $\mathbf{A}_3^{12}$ of the floating raft can be described as follows,

$$\chi_{ls}(x_l^{(3)}, x_s^{(4)}) = \frac{j\omega}{m}\sum_{n=1}^{\infty}\frac{\psi_n^{(3)}(x_l^{(3)})\psi_n^{(4)}(x_s^{(4)})}{\left[\Omega_n^{(3)}\right]^2(1+j\eta_n^{(3)}) - \omega^2}, (l = 1, ..., M, s = 1, ..., N), \tag{9.17}$$

where the normal mode functions of the top and bottom skins of the free free sandwich beam for the raft structure in S_3 are denoted by $\psi_n^{(3)}$ and $\psi_n^{(4)}$ respectively.

Similarly, the mobility matrix of the base sandwich structure S_5 can be described as follows,

$$\mathbf{A}_5 = [\Xi_{sk}(x_s^{(5)}, x_k^{(5)})]_{N\times N}, (s, k = 1, 2, ..., N). \tag{9.18}$$

The components of the mobility matrix of the base structure can be described as follows,

$$\Xi_{sk}(x_s^{(5)}, x_k^{(5)}) = \frac{j\omega}{m}\sum_{n=1}^{\infty}\frac{\varphi_n^{(5)}(x_s^{(5)})\varphi_n^{(5)}(x_k^{(5)})}{\left[\Omega_n^{(5)}\right]^2(1+j\eta_n^{(5)})-\omega^2}, \tag{9.19}$$

where $\varphi_n^{(5)}$ denotes the normal mode functions of the top skins of the clamped sandwich beam for the base structure in S_5.

9.4 Natural Vibration Characteristics of Sandwich Beams Using Higher Order Theory

Especially, this study attempts to find out frequency change in different kinds of boundary conditions and frequency dependent damping effect of MRE embedded sandwich beam with potential, eventual application in smart floating raft vibration isolation systems using by smart sandwich raft for ship structures to reduce noise occurred in high frequency band. In order to estimate the total power flow in a sandwich floating raft isolation system, the natural characteristics of sandwich structures need to be studied first. For numerical simplicity the floating raft, substructure S_3, can be modelled as a free-free sandwich beam while the base structure, substructure S_5, can be modelled as a clamped-clamped sandwich beam. From the numerical calculations, corresponding values of natural vibration (Ω_n, mode shapes (ψ_n, φ_n) and modal loss factor (η_n) from Eq. 7.24 of two different, free-free and clamped, sandwich structures are given to Eqs. 9.17 and 9.19 as an input values.

9.5 Power Flow Analysis for Sandwich Floating Raft Vibration Isolation System

For numerical calculations, the following data are used : m_1 = 50 Kg, m_2 = 30 Kg, b_i = 25 mm (i=1, 2, 3, 4). The stiffness and mass of the isolator in substructure 2 is 20 N/mm (K_l) and 0.5 Kg (M_l) and those of the isolator in substructure 4 is 40 N/mm (K_s) and 0.5 Kg (M_s). Four isolators, two at each mass, are used in substructure 2 while three isolators are used in substructure 4. The loss factor (η_I) of the isolators in substructure 2 and 4 is 0.05. Vertical harmonic excitation forces are of the forms $f_{11} = e^{i\omega t}$, $f_{12} = 2f_{11}$. The sandwich beam in substructure S_3 and S_5 consists of two glass-ceramic skins of dimensions 300 $\times$ 30 $\times$ 1.0 mm^3 which are bonded to the top and bottom of a PVC core of dimensions 300 $\times$ 30 $\times$ 20 mm^3. The Young's modulus of the isotropic glass-ceramic skins and the shear modulus of the core are 36 GPa and 20 MPa respectively and the respective densities of the skins and core are 4,400 and 52.06 Kg/m^3, as used Sokolinsky *et al.* (2002). The loss factor (η_I) of the core materials is 0.05.

9.5.1 Input power and transmitted power

Fig. 9.4 compares the input power spectrum P_1 owing to the two machines to the total power flow transmission spectra P_3 and P_5. The difference between them indicates the energy dissipated in this raft isolation system. It can be seen that the input power flow spectrum P_1 is relatively simple in form with three pronounced peaks corresponding to the natural frequencies of the isolation system. The transmission spectra P_3 and P_5, however, vary significantly with the exciting frequencies in the medium- and high- frequency range, since they now contain contributions from the elastic mode coupled dynamics of the overall system. The relatively small number of coupled system and intermediate mass of isolators at substructure 3 reduce the number of peaks and power spectrum P_3 respectively. The number of peaks indicate that the total input power spectrum P_1 is less sensitive than the total transmitted power spectrum to the changes of the excitation

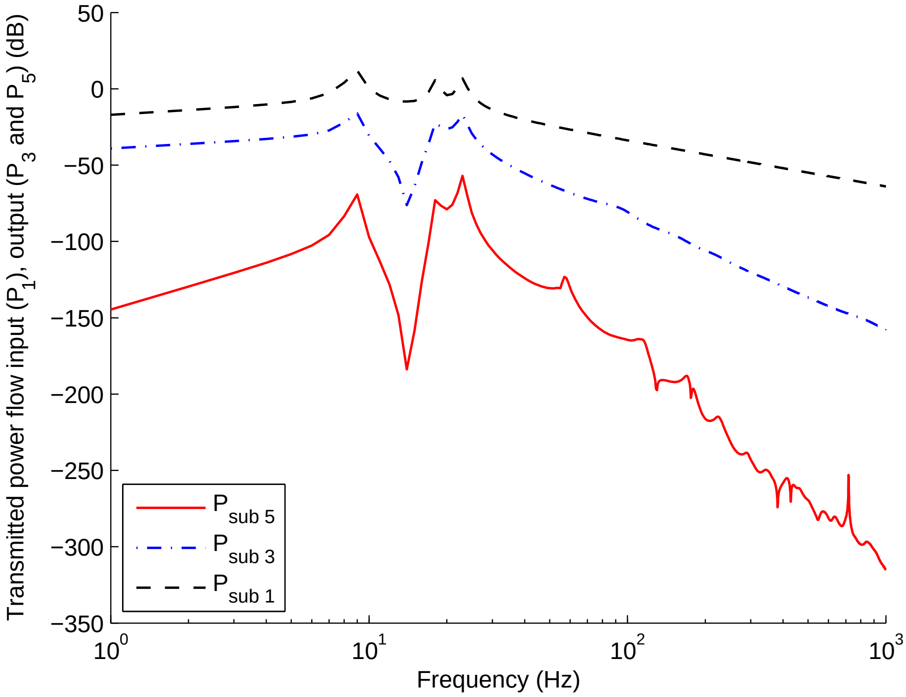

Figure 9.4: Comparison of power flow spectra

frequencies as shown in Fig. 9.4. The behaviour of the power flow spectrum is supported by numerical results (Xiong *et al.* , 2001).

Based on the parameters described in the previous section, the influence of different variables such as thickness of core, thickness of skin, stiffness of sandwich raft and base structure and the effect of isolators on power transmitted to the flexible foundation are discussed below.

9.5.2 Effect of sandwich raft on power transmissions

Fig. 9.5a compares power flow spectra P_5 considering different thicknesses of core material in substructure 3 whilst skin thickness remains at 1mm. When the thickness of the core increases from 20 to 80mm, the transmitted power spectrum decreases. The reason for this is that when the thickness of the core increases the stiffness of the sandwich beam also increases, which results in decreasing power transmitted to the base structure. This again is supported by the conclusion in

Xiong *et al.* (1996). This indicates that an increase in core thickness of the sandwich raft increases its stiffness, thus reducing the power transmitted to the foundation at low-frequency ranges, and alters resonant peaks at medium-frequency ranges, hence providing good vibration isolation. This result shows good agreement with the trends in Li *et al.* (1997), i.e. that the transmitted energy decreases as thickness of the core increases. Fig. 9.5b compares power flow spectra with different thicknesses of skin material of the sandwich raft for core thickness of 20 mm. The change in thickness of the skin materials does not affect the power spectrum at low-frequency ranges. From medium-frequency ranges to high frequency ranges, the transmitted power spectrum decreases prominently with the increase of skin thickness.

9.5.3 Effect of sandwich base structure on power transmissions

Fig. 9.6a shows power flow spectra (P5) of the isolation system with different thickness of core material of sandwich beam in substructure 5 whilst skin thickness remains at 1 mm. Similar to the result of Fig. 9.5a, the core thickness changes also affect the transmitted power. However, since decreased power flow from floating raft may not be effective to further decreasing power flow at foundation, change in the power flow spectrum of the foundation is less significant than that of the floating raft in the whole frequency range.

Fig. 9.6b presents power flow spectra with different thicknesses of skin material of sandwich beam for substructure S_5 for core thickness of 20 mm. The change in thickness of the skin material does not affect much on power spectrum in the whole frequency ranges. Even though there are power decreases at high frequencies, the power reduction is not much more effective than that of the floating raft, substructure S_3.

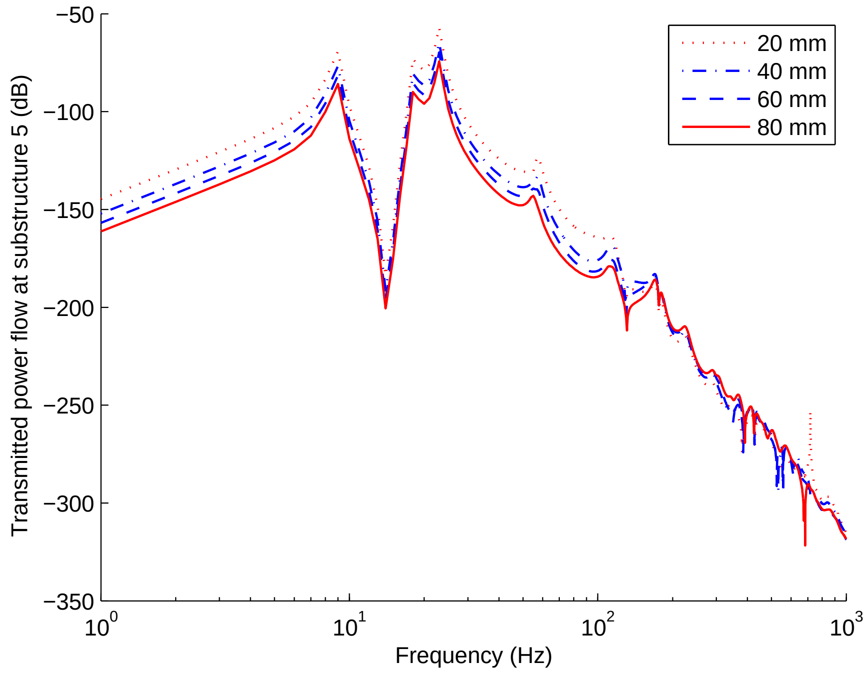

(a)

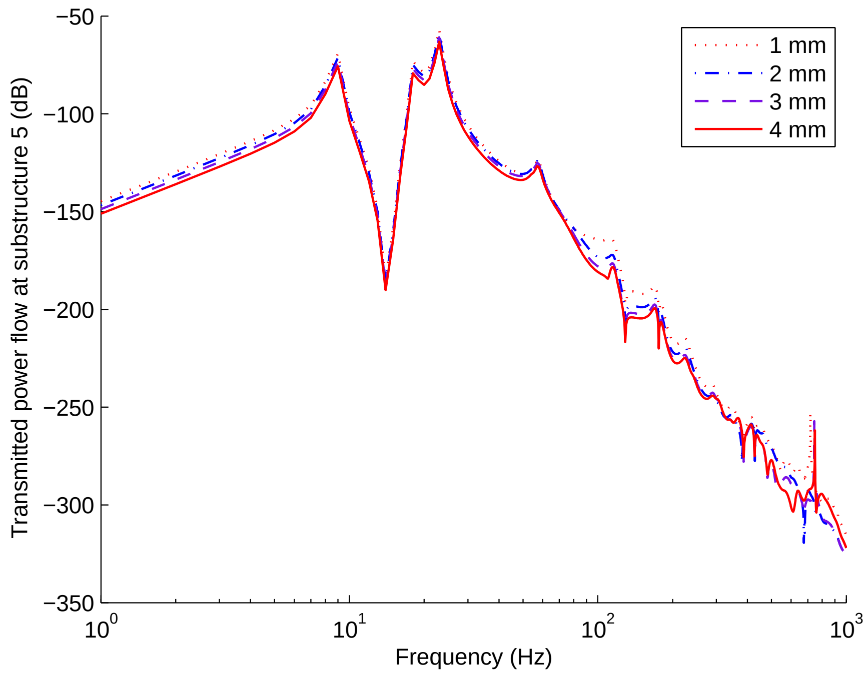

(b)

Figure 9.5: Comparison of power flow spectra (P_5) under the different thickness of (a) core material and (b) skin material in substructure 3

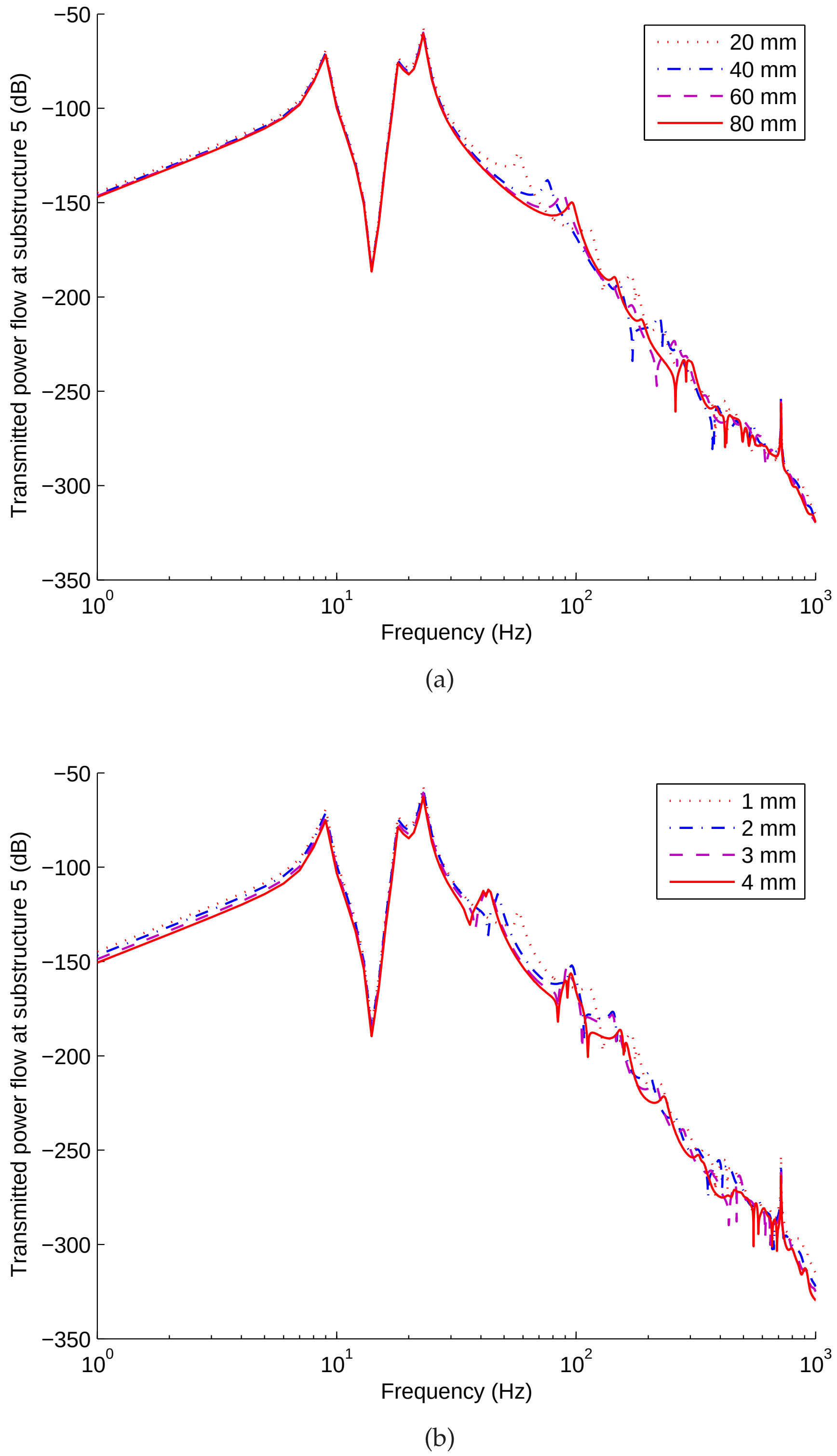

Figure 9.6: Comparison of power flow spectra (P_5) under the different thickness of (a) core material and (b) skin material in substructure 5

9.5.4 Changing skin and core modulus of raft beam

Fig. 9.7a shows a comparison of power flow spectra (P_5) with different properties of skin material of the sandwich beam in substructure 3. The reference Young's modulus (E_{ref}) of the skin material is 36 GPa. It is clear that even though the modulus changes by a ten-fold margin there is little effect on the power flow spectrum because it cannot reflect the whole stiffness of the floating raft effectively. Fig. 9.7b shows a comparison of power flow spectra (P_5) with the different properties of core material of sandwich beam in substructure 3, where reference shear modulus (G_{ref}) of the core material is 20 MPa. This result shows that property change of the core material is more effective than that of the skin material.

9.5.5 Effect of isolators

Fig. 9.8 shows a comparison of transmitted power spectra with different stiffness of the isolators in substructure 2 and substructure 4. The respective reference stiffnesses (K_{ref}) of the isolators are 20 and 40 N/mm in substructure 2 and substructure 4. Comparisons are made with isolators stiffnesses of one tenth and ten times that of the reference values, i.e. stiffness ratios of 0.1 and 10. Transmitted power spectrum (P_5) changes as stiffness of the isolator changes. Contrary to the results of sandwich beam structure, transmitted power changes in inverse proportion to the change of the stiffness of the isolators. In Fig. 9.8a, the fundamental frequency of around 10 Hz is altered as the stiffness of the isolator changes. However after 100 Hz, the pattern of the three power spectrum curves are similar. Fig. 9.8b shows that in lower-frequency range the resonant peaks dominated by isolators are altered as the stiffness of the isolator changes up to 50 Hz. This is because the coupling effect of the two stage isolation system, in which the floating raft as well as base beam behave like rigid body. However above the frequency of 50 Hz the resonant peaks of the three power spectrum are identical because of the coupling effect of elastic modes of raft and base beams. Since the stiffness of the isolators in substructure 4 is higher than that in substructure 2, the change of fundamental

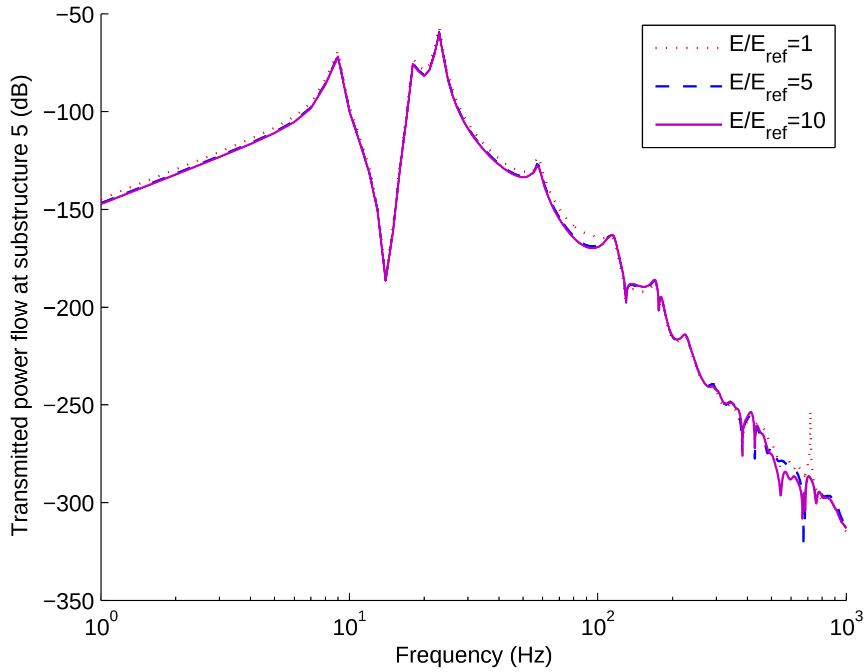

(a)

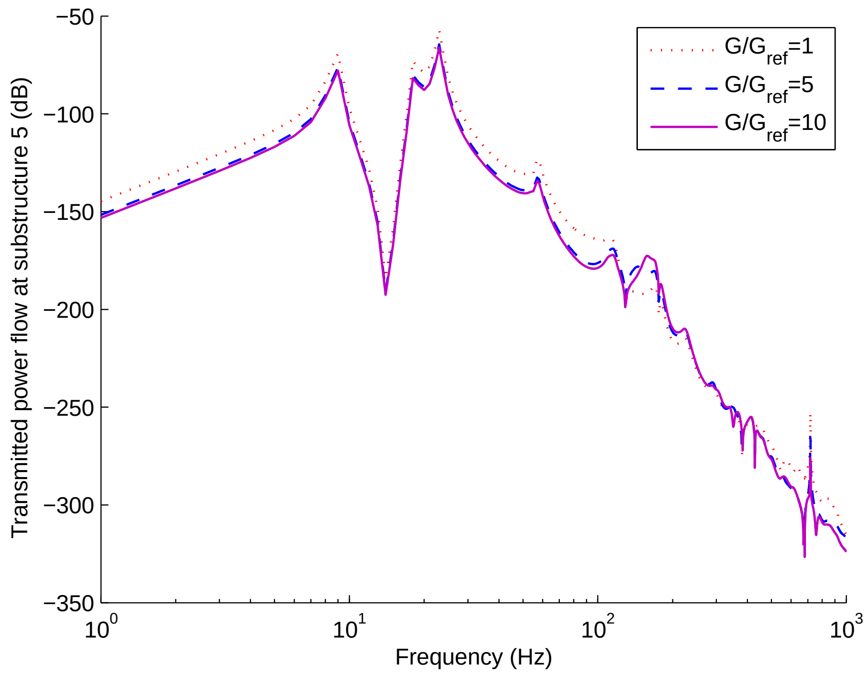

(b)

Figure 9.7: Comparison of power flow spectra (P_5) under the different properties of (a) skin material and (b) core material in substructure 3

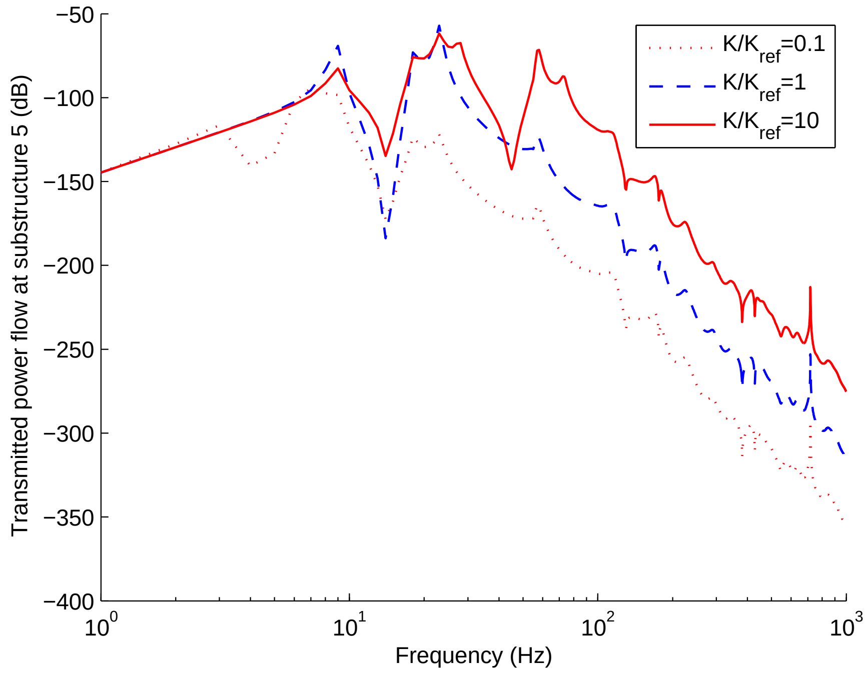

(a)

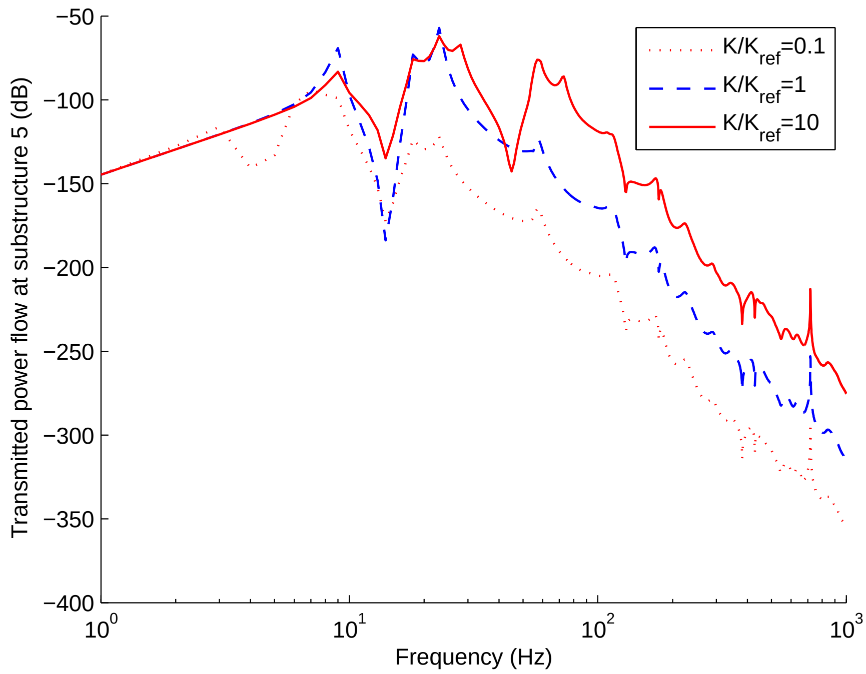

(b)

Figure 9.8: Comparison of power flow spectra (P_5) under the different stiffness of isolators between (a) substructure 2 and (b) substructure 4

frequency ranges are shifted to higher-frequency ranges. These results show that coupling mechanism between isolators and flexible beams need to be considered in the design of the floating raft isolation systems.

9.5.6 Damping effect of core materials in sandwich raft beam

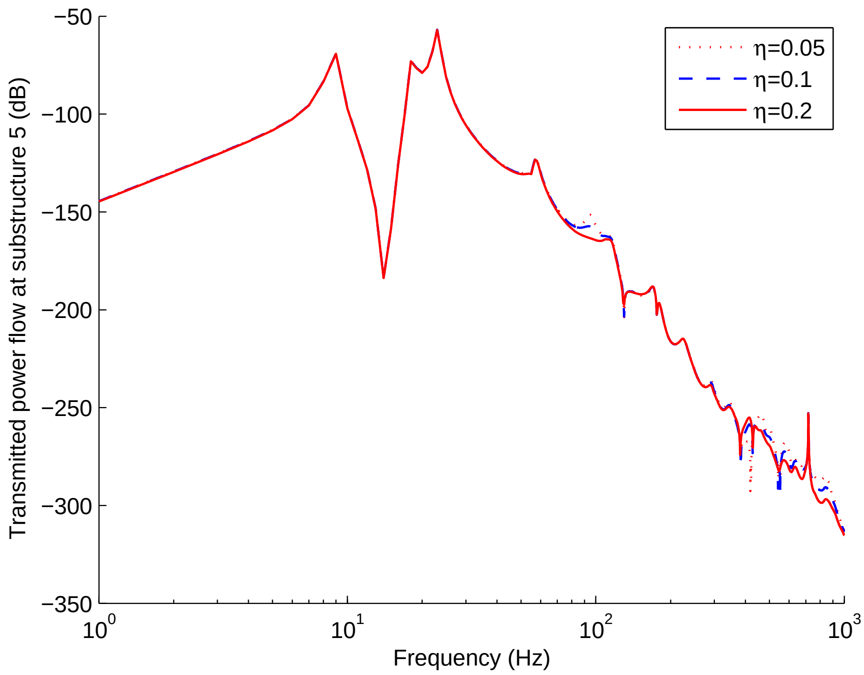

Figure 9.9: Comparison of power flow spectra (P_5) under the different damping of core material in substructure 3

The influence of the damping effect for core materials of the floating raft can be observed in Fig. 9.9. It is shown that increasing the loss factor of the core material reduces the resonant peaks of the transmitted power flow spectra (P_5) in the medium- to high- frequency ranges. At low- frequencies ranges, changes in the transmitted powers cannot be observed. Also, there is not much effect on the reduction of resonant peak prominently. However, the damping effect can be seen in the medium frequency range at about 100 Hz. It is interesting to note that there is a pronounced peak observed in the transmitted power spectrum in P_5 at about 650 Hz. This is because the modal damping of the sandwich raft beam corresponding to the symmetric vibration mode of the beam is very small. This phenomenon can be explained from Fig. 9.9 which shows different modal loss factors for each mode based on numerical calculation. This indicates that this resonant peak cannot be avoided by increasing damping only in the high-frequency ranges, which is not found in floating raft isolation system with isotropic beams. Further calculations show that this peak can be avoided by changing stiffness of the raft and placement of isolators.

9.6 Conclusion

A higher-order sandwich theory is implemented in conjunction with an equivalent mobility-based power flow progressive method to determine power flow for a sandwich configured floating raft vibration isolation system. The generalized mobility matrices of a sandwich floating raft and flexible foundation are derived using higher-order sandwich theory.

The results from the application of the models developed herein show the following attributes: (a) increasing thickness of the core material of sandwich type floating raft decreases transmitted power more effectively than that of foundation; (b) when different properties of core material of floating raft are used, the power spectrum varies in whole frequency range, which leads to the conclusion that when a sandwich beam is considered as a floating raft, the core material choice is more influential than that of skin material; (c) the stiffness change of isolators does not affect the pattern of power spectrum in high-frequency ranges, though compromises between numbers and stiffnesses of the isolators must be considered carefully; (d) the loss factors of a sandwich configured floating raft influence the power flow transmitted to the foundation effectively from medium- to high-frequency range. However the resonant peak corresponding to the symmetric mode of the sandwich raft in high-frequency ranges cannot be avoided by increasing damping only. The resonant peak can be avoided by changing stiffness of the raft and placement of isolators.

Overall, since a sandwich structure is adaptable, a smart sandwich beam can be shown to be an adjustable floating raft which can control transmitted power from the machinery to the base structure.

Chapter 10

Discussion and Novelty

This thesis described work concerned with the dynamic behaviour of magnetorheological elastomers (MRE) and MRE cored smart sandwich structure. Four novel or unique features distinguish this work as outlined below.

10.1 Analysis of Dynamic Shear Properties of MRE

Dynamic MRE performances in terms of curing time, strain range and porous effect under different magnetic field strength have been investigated. It has been found that MRE samples cured in optimum time under magnetic field exhibit higher stiffness than samples cured for longer periods. Large hysteresis effect of MRE indicates that cured sample under magnetic field shows better damping effect than sample cured room temperature only. It is worth noting that the change in loss factor is also dependent on strain ranges. Furthermore, the overall performance (stiffness and damping changes) of porous MRE is found to be better than that of denser MRE, since the magnetic forces create larger displacements within the matrix of MRE with pores. However, the porous effect may result in poor integrity of material. With a controlled introduction of pores during manufacture, elastomers with a good MR effect may be developed.

In addition an enhanced theoretical model with magnetisation effect on iron particles is presented to achieve proper curing time. Good agreement between the experimental results and the theoretical prediction including the magnetisation effect on MRE is found. In parallel with this, a new macro scale modelling approach for rubber like nonlinear behaving materials by adopting FEA analysis is presented to obtain the optimum volume of pores and size of iron particles to enhance the performance of MREs. The overall performance (stiffness and damping changes) of porous MRE is found to be better than that of denser MRE, since the magnetic forces create larger displacements within the matrix of MRE with pores. It has been demonstrated that the change of shear modulus is found to increase with an increase in the volume fraction of pores. Moreover, numerical results also show that the size of iron particles within MRE materials influences MR performance: as the size of iron particles decreases, higher stiffness and hysteretic behaviour is observed.

This leads to the conclusion that despite the same combination of iron particles and elastomers, the characteristics of MRE can be different owing to variations in the size of iron particles, different curing time and volume fraction of pores.

10.2 Analysis of MRE Core Embedded Sandwich Beam

A new forced vibration test rig was developed to carry out comprehensive experimental forced vibrational tests of MRE embedded sandwich beam to study various aspects such as different magnetic field strength, various oscillations of force amplitudes, boundary conditions and damping effects under localised magnetic fields.

The results led to the following observations: (a) Frequency changes of clamped beam were more effective than those of simply supported beam. However, an obvious damping effect was observed when the beam was simply supported and when the air gap was reduced; (b)Since sandwich beam with thick steel skins induced more magnetic field than that with thin steel skins, more energy dissipation could occur with thick skins under the same magnetic field strength; (c) The force amplitude, the magnetic field strength and the combination of localised magnetic field affect the damping values; (d) The damping changes were effective when magnetic fields were applied in the middle rather than near of boundaries; (e) The magnetic field with same polarity was shown to lead to different behaviour of the beam compared to when the magnetic of with different polarity was deployed. Overall, these results enable to give a guideline for conducting potential applications for various shapes of MRE configured sandwich structures.

In addition the vibration characteristics of an MRE cored sandwich beam are investigated to understand pheonomenon of frequency and damping changes under the magnetic field, theoretically and numerically. Higher order sandwich beam theory is extended to include damping properties of MRE. Validations for the analytical model agree well with experimental and FEA results for a steel skin and PVC core sandwich beam. Theoretical sensitivity analyses show damping effect in terms of different topologies. It is seen that relatively thicker cored sandwich beam exhibits more damping effect. Futhermore, FEA results reveal that when boundary condition is more constrained, higher frequency change effects can be obtained, which is reasonably agreeable with experimental results shown in Chapter 5. It has been demonstrated that higher order sandwich beam theory appears to be the most versatile and accurate modelling method for sandwich beam with soft core material.

10.3 Power Flow Analysis Based on Higher Order Sandwich Beam Theory

In parallel to the development of higher order sandwich beam theory, power flow analysis for the smart floating sandwich raft vibration isolation system was carried out. A higher-order sandwich theory was implemented in conjunction with an equivalent mobility-based power flow progressive method to determine power flow for a sandwich configured floating raft vibration isolation system for a steel skin and PVC core sandwich beam. The generalized mobility matrices of a sandwich floating raft and flexible foundation were derived using higher-order sandwich theory. Modal loss factor predicted from higher order sandwich beam theory in terms of different boundary condition was also implemented.

The results from the application of the models developed herein showed the following attributes: (a) increasing thickness of the core material of sandwich type floating raft decreases transmitted power more effectively than that of foundation; (b) when different properties of core material of floating raft are used, the power spectrum varies in whole frequency range, which leads to the conclusion that when a sandwich beam is considered as a floating raft, the core material choice is more influential than that of skin material; (c) the stiffness change of isolators does not affect the pattern of power spectrum in high-frequency ranges, though compromises between numbers and stiffnesses of the isolators must be considered carefully; (d) the loss factors of a sandwich configured floating raft influence the power flow transmitted to the foundation effectively from medium- to high-frequency range. However the resonant peak corresponding to the symmetric mode of the sandwich raft in high-frequency ranges cannot be avoided by increasing damping only. The resonant peak can be avoided by changing stiffness of the raft and placement of isolators.

Overall, since a sandwich structure is adaptable, a smart sandwich beam is shown to be an adjustable floating raft which can control transmitted power from the machinery to the base structure.

10.4 Potential Applications for Propeller Shaft

An experimental study is carried out to illustrate the control capabilities of an MRE based adaptive vibration absorber for a propeller shaft in real time. It is observed that the vibration amplitudes at fundamental frequency ranges are significantly reduced by applying a magnetic field. Due to property change capability of MRE, a significant frequency shift occurs and vibration amplitude reduction was observed. That is to say, an MRE absorber can reduce vibration amplitude of the shaft as well as outside of the shaft such as in the bearings, the strut and so on. In numerical studies, frequency response analyses with various size of MRE layer were carried out. It was shown that even small amounts of MRE layer, large frequency change can be acquired. These results give a guideline of how to design MRE vibration absorber isolation system in conjunction with an adaptive passive control system. Overall, this new idea could potentially be used in car industry, marine, and other application where rotating shafts are used to transmit power from the source to the application / delivery location such as a car transmission system and a wind turbine system.

Chapter 11

Conclusions and Further Research Work

11.1 Conclusions

The work presented in this thesis has provided an extensive examination on the dynamic characteristics of MRE material and MRE adaptive sandwich structures. The experimental investigations provide essential information on the curing time and porous dependency on the dynamic MRE properties. These experimental works have contributed to increasing the available knowledge of MRE materials as well as the database of their dynamic material properties. A theoretical investigation when combined with the knowledge of magnetisation effect depending on curing time provides a unique method which allows the prediction of the property of MRE. From macro scaled FE simulations, change of shearmodulus is found to increase with an increase in the volume fraction of pores. Numerical results also show that the size of iron particles withinMREmaterials influencesMR performance: as the size of iron particles decreases, lower stiffness and higher hysteretic behaviour is observed.

In addition, the new developed forced vibration test rig has provided a comprehensive examination of the dynamic behaviour of the MRE adaptive sandwich structures based on material characterisations with respect to different boundary conditions, various topologies and localised magnetic fields. Furthermore, higher order sandwich beam theory has been demonstrated as being the most versatile and practical model to predict the modal frequencies and damping effect of a MRE configured sandwich beam. FEA results revealed that different MR performance can be achievedwhich depends on the location ofmagnetic fields applied even with same amount of magnetic field area. These results indicate that the beneficial effect of localised magnetic field is dependent of area of magnetic field as well as location of magnetic field.

Experimental and numerical works on adaptive vibration absorber for a propeller shaft has illustrated the control capabilities of MRE adaptive vibration absorber for a propeller shaft in real time. It is observed that the vibration amplitudes at fundamental frequency ranges are significantly reduced by applying a magnetic field. This new idea could potentially provide an improved means to reduce/eliminate vibration in rotating shafts that are used to transmit power from the source to the delivery location.

Finally, power flow analysis using progressive methods, based on modal analysis by aid of higher-order sandwich beam theory, for flexible sandwich configured floating raft vibration isolation system was proposed using PVC core. Case studies of how various topologies of sandwich floating raft can act as vibration isolation systems have been presented. It can be concluded that smart sandwich beam as a floating raft controls vibration transmission from the machinery to the base structure.

11.2 Further Research Work

Several areas for further experimental and theoretical investigations that will need to be addressed have been identified as follows:

- For material characteristics of MRE, more studies on aging and life cycle prediction of MRE needs to be carried out.

- For structural characteristics, frequency dependent magnetic preload effect on MRE core embedded sandwich beam should be carried out based on higher order sandwich theory.

- Macro scale FE analysis restricts the analysis to mechanical properties of MRE. More accurate modeling including magnetic attraction and repulsion among iron particles to explore the behaviour of MRE using a usersubroutine provided by ABAQUS is necessary.
- Experiment set up for vibration absorber for a propeller shaft shoud be conducted with a rotating shaft and bearing including control algorithm.
- The effect of electromagnetic interference (EMI) on other onboard electric equipment needs to be considered for real applications.

References

ABRAMCHUK, S., KRAMARENKO, E., STEPANOV, G., NIKITIN, L. V., FILIPCSEI, G., KHOKHLOV, A. R., & ZRNYI, M. 2007. Novel highly elastic magnetic materials for dampers and seals: Part I. Preparation and characterization of the elastic materials. *Polymers for Advanced Technologies*, **18**, 883–890.

AGARWAL, B.B., & BROUTMAN, L.J. 1990. *Analysis and performance of fibre composites*. John Wiley&Sons.

ALLEN, H.G. 1969. *Analysis and Design of Structural Sandwich Panels*. Pergamon Press, Oxford.

AUSANIO, G., BONETTI, E., IANNOTTI, V., LANOTTE, L., LUPONIO, C., & PASQUINI, L. 2002. Time dependence of magnetization and strain in Terfenol. *Journal of Magnetism and Magnetic Materials*, **242**(Part 2), 1453–1456.

BACCAREDDA, MARIO, BUTTA, ENZO, FROSINI, VITTORIO, & DE PETRIS, SILVANO. 1967. Mechanical secondary relaxation effects in polysulfone. *Journal of Polymer Science Part A-2: Polymer Physics*, **5(6)**, 1296–1299.

BALDWIN, C, KIDDY, J, SALTER, T, CHEN, P, & NIEMCZUK, J. 2002. Fiber optic structural health monitoring system : rough sea trials of the RV triton. *MTS/IEEE Oceans*, **3**, 1807–1814.

BANDYOPADHYAY, PR. 2002. A biomimetic propulsor for active noise control : Experiments. *Naval Undersea Warfare Center, NUWC-NPT Tech. Rep.*, **11351**.

BANDYOPADHYAY, PR. 2005. Trends in biorobotic autonomous undersea vehicles. *IEEE Journal of oceanic engineering*, **30(1)**.

BARRETT, R. 1994. Active plate and missile wing development using directionally attached piezoelectric elements. *AIAA Journal*, **32**, 601–609.

BAZ, A, IMAM, K, & MCCOY, J. 1990a. Active vibration control of flexible beams using shape memory actuators. *Journal of Sound and Vibration*, **140(3)**, 437–456.

BAZ, A., GILHEANY, J., & STEIMEL, P. 1990b. Active vibration control of propeller shafts. *Journal of Sound and Vibration*, **136**(3), 361–372.

BERGSTROM, J. 1999. *Large strain time-dependent behavior of elastomeric materials*. Ph.D. thesis, MIT.

BERNHARD, R.J., HALL, H.R., & JONES, J.D. 1992. Adaptive-passive noise control. *Inter-Noise*, **92**, 427–430.

BLOCK, H., & KELLY, J.P. 1988. Electro-rheology. *J. Physics*, **D(21)**, 1661–1677.

BLOM, P., & KARI, L. 2005. Amplitude and frequency dependence of magneto-sensitive rubber in a wide frequency range. *Polymer Testing*, **24**(5), 656–662.

BLOM, P., & KARI, L. 2008. Smart audio frequency energy flow control by magneto-sensitive rubber isolators. *Smart Materials and Structures*, **17**, 1–5.

BROWN, E.N., WHITE, S.R., & SCOTTS, N.R. 2005. Retardation and repair of fatigue cracks in a microcapsule toughened epoxy composite. Part II: In situ self-healing. *Composites Science and Technology*, **65**, 2474–2480.

BUTER, A., & BREITBACH, E. 2000. Adaptive blade twist - calculations and experimental results. *Aerospace Science and Technology*, **4**, 309–319.

CARLSON, J.D., & JOLLY, M.R. 2000. MR fluid, foam and elastomer devices. *Mechatronics*, **10**(4-5), 555–569.

CHOI, S.B., & CHEONG, C.C. 1996. Vibration control of a flexible beam using shape memory alloy actuators. *Journal of Guidance, Control, and Dynamics*, **19(5)**, 1178–1180.

CHOI, W.J., XIONG, Y.P., & SHENOI, R.A. 2007. Vibration characteristics of smart sandwich beams embedded with magnetorheological elastomer cores. *Pages 421–428 of: First International Conference on Marine Structures, March 12-14, Glasgow, UK*.

CHOI, W.J., XIONG, Y.P., & SHENOI, R.A. 2008 (May). Characterisation of magnetorheological elastomer materials for the core of smart sandwich structures. *Pages 818–826 of:* FERREIRA, ANTONIO (ed), *8th International Conference on Sandwich Structures*, vol. 2. Journal of sandwich structures and materials.

CHOI, W.J., XIONG, Y.P., & SHENOI, R.A. 2009a. Power flow analysis for a floating sandwich raft isolation system using a higher-order theory. *Journal of Sound and Vibration*, **319**, 228–246.

CHOI, W.J., XIONG, Y.P., & SHENOI, R.A. 2009b. Vibration control apparatus, UK Patent Application No. 0902659.2. *London, UK, Patent Office*.

CLARK, R.L., SAUNDERS, W.R., & GIBBS, G.P. 1998. *Adaptive structures: dynamics and control*. New York, Chichester : Wiley-Interscience.

CLARKSON, B.L. 1991. Estimation of the coupling loss factor of structural joints. *Proceedings of The Institution of Mechanical Engineers Part C-Journal of Mechanical Engineering Science*, **205**(1), 17–22.

CRAWLEY, EF. 1992. Intelligent structures - A technology overview and assessment. *Smart structures for aircraft and spacecraft*, **6**, 1–16.

CUSCHIERI, J.M. 1990. Vibration transmission through periodic structures using a mobility power flow approach. *Journal of Sound and Vibration*, **143**(1), 65–74.

DAVIS, L.C. 1998. Model of magnetorheological elastomers. *Journal of Applied Physics*, **85(6)**, 3348–3351.

DAWOOD, T.A., SHENOI, R.A., & SAHIN, M. 2007. A procedure to embed fibre Bragg Grating strain sensors into GFRP sandwich structures. *Composites Part A: Applied Science and Manufacturing*, **38**, 217–226.

DEMCHUK, S.A., & KUZ'MIN, V.A. 2002. Viscoelastic properties of magnetorheological elastomers in the regime of dynamic deformation. *Journal of Engineering Physics and Thermophysics*, **75(2)**, 396–400.

DENG, H., & GONG, X. 2008. Application of magnetorheological elastomer to vibration absorber. *Communications in Nonlinear Science and Numerical Simulation*, **13**(9), 1938–1947.

DENG, H., GONG, X., & WANG, L. 2006. Development of An Adaptive Tuned Vibration Absorber with Magnetorheological Elastomer. *Smart Materials and Structures*, **15(5)**, N111–N116.

DIAMANTI, K., SOUTIS, C., & HODGKINSON, J. 2005. Lamb waves for the non-destructive inspection of monolithic and sandwich composite beams. *Composites*, **Part A 36**, 189–195.

DITTRICH, K.W. 1998. Prospects of smart structures for future aircraft. *Mechanics of Composite Materials and Structures*, 509–517.

DONG, Y.S., XIONG, J.L., LI, A.Q., & LIN, P.H. 2006. A passive damping device with TiNi shape memory alloy rings and its properties. *Material Science and Engineering : A Structural materials properties microstructure and processing*, **416(1-2)**, 92–97.

DORFMANN, A., & OGDEN, R. W. 2003. Magnetoelastic modelling of elastomers. *European Journal of Mechanics - A/Solids*, **22**(4), 497–507.

EWINS, D.J. 2000. *Modal Testing, Theory, Practice, and Application*. Research studies press LTD.

FERRY, J.D. 1980. *Viscoelastic properties of polymers*. John Wiley & Sons, Inc.

FLETCHER, W.P., & GENT, A.N. 1953. Non-linearity in the dynamic properties of vulcanised rubber compounds. *Trans. Inst. Rubber Ind.*, **29**, 266–280.

FRANCHEK, M.A., RYAN, M.W., & BERNHARD, R.J. 1996. Adaptive passive vibration control. *Journal of Sound and Vibration*, **189**(5), 565–585.

FROSTIG, Y. 1992. Behavior of delaminated sandwich beam with transversely flexible core-high order theory. *Composite Structures*, **38**, 383–394.

FROSTIG, Y., & BARUCH, M. 1994. Free vibrations of sandwich beams with a transversely flexible core : A high order approach. *Journal of Sound and Vibration*, **176(2)**, 195–208.

FROSTIG, Y., BARUCH, M., & SHEINMAN, I. 1992. High-order theory for sandwich-beam behavior with transversely flexible core. *Journal of Engineering Mechanics*, **118(5)**, 1026–1043.

GINDER, J.M., NICHOLS, M.E., ELIE, L.D., & CLARK, S.M. 2000. Controllable stiffness components based on magnetorheological elastomers. *Pages 418–425 of: Wereley, N.M.(ed. Smart and Materials 2000: Smart Structures and Integrated Systems, Proceedings of SPIE 3985)*.

GINDER, J.M., CLARK, S.M., SCHLOTTER, W.F., & NICHOLS, M.E. 2002. Magnetostrictive phenomena in magnetorheological elastomers. *Int. J. Modern Phys. B*, **16**, 2412–2418.

GOYDER, H.G.D., & WHITE, R.G. 1980. Vibration power flow from machines into built-up structures. *Journal of Sound and Vibration*, **68**, 59–117.

HA, J.Y., & KIM, K.J. 1995. Analysis of mimo mechanical systems using the vectorial four pole parameter method. *Journal of Sound and Vibration*, **180**(2), 333–350.

HERSZBERG, I., LI, H., DHARMAWAN, F., MOURITZ, A., NGUYEN, M., & BAYANDOR, J. 2005. Damage assessment and monitoring of composite ship joints. *Composite Structures*, **67**, 205–216.

HODGSON, E.W., BENDER, A., GOLDFARB, J., HANSEN, H., QUINN, G., SRIBNIK, F., & ERKEY, C.T. 2004. A chameleon suit to liberate human exploration of space environments. *NASA Institute for Advanced Concepts Contract # 07600-082*.

HOUSNER, G.W., BERGMAN, L.A., CAUGHEY, T.K., CHASSIAKOS, A.G., CLAUS, R.O., MASRI, S.F., SKELTON, R.E., SOONG, T.T., SPENCER, B.F., & YAO, J.T.P. 1997. Structural control : past, present, and future. *Journal of Engineering Mechanics*, **123(9)**, 897–971.

HU, H., BELOUETTAR, S., POTIER-FERRY, M., & DAYA, E.M. 2008. Review and assessment of various theories for modeling sandwich composites. *Composite Structures*, **84**(3), 282–292.

HU, Y., WANG, Y.L., GONG, X.L., GONG, X.Q., ZHANG, X.Z., JIANG, W.Q., ZHANG, P.Q., & CHEN, Z.Y. 2005. New magnetorheological elastomers based on polyurethane/Si-rubber hybrid. *Polymer Testing*, **24**(3), 324–329.

HUMBEECK, J.V., & KUSTOV, S. 2005. Active and passive damping of noise and vibrations through shape memory alloys: applications and mechanisms. *Smart Materials and Structures*, **14**, s171–s185.

HUSSEIN, M.F.M., & HUNT, H.E.M. 2006. A power flow method for evaluating vibration from underground railways. *Journal of Sound and Vibration*, **293**(3-5), 667–679.

HYDE, T.T., & AGNES, G. 2000. Adaptive structures. *Aerospace America*.

JENKINS, M.D., NELSON, P.A., PINNINGTON, R.J., & ELLIOTT, S.J. 1993. Active isolation of periodic machinery vibrations. *Journal of Sound and Vibration*, **166**(1), 117–140.

JENSEN, A.E., & IRGENS, F. 1999. Thickness vibration of sandwich plates and beams and delamination detection. *Journal of Intelligent Material Systems and Structures*, **10(1)**, 46–55.

JOLLY, M.R., CARLSON, J.D., MUNOZ, B.C., & BULLIONS, T.A. 1996a. The magnetoviscoelastic response of elastomer composites consisting of ferrous particles embedded in a polymer matrix. *Journal of Intelligent Material and Structures*, **7**, 613–621.

JOLLY, M.R., CARLSON, J.D., & MUNOZ, B.C. 1996b. A Model of the behavior of magnetorheological materials. *Smart Materials and Structures*, **5**, 607–614.

JOLLY, M.R., BENDER, J.W., & CARLSON, J.D. 1999. Properties and applications of commercial magnetorheological fluids. *Journal of Intelligent Material Systems and Structures*, **10(1)**, 5–13.

KAGEYA, K., KAGEYAMA, K., KIMPARA, I., SUZUKI, T., OHSAWA, I., MURAYAMA, H., & ITO, K. 1998. Smart marine structures: an approach to the monitoring of ship structures with fiber-optic sensor. *Smart Materials and Structures*, **7**, 472–478.

KALLIO, M. 2005. *The elastic and damping properties of magnetorheological elastomers*. Ph.D. thesis, Tampere University of Technology.

KALLIO, M., LINDROOS, T., AALTO, S., JARVINEN, E., KARNA, T., & MEINANDER, T. 2007. Dynamic compression testing of a tunable spring element consisting of a magnetorheological elastomer. *Smart Materials and Structures*, **16**, 506–514.

KESSLER, S.S., SPEARING, S.M., & SOUTIS, C. 2002. Damage detection in composite materials using Lamb wave methods. *Smart materials and structures*, **11**, 269–278.

LANGLEY, R.S. 1990. Analysis of power flow in beams and frameworks using the direct-dynamic stiffness method. *Journal of Sound and Vibration*, **136**(3), 439–452.

LEE, Y.S. 2000. *Active Control of Smart Structures using Distributed Piezoelectric Transducers*. Ph.D. thesis, University of Southampton.

LEWIS, D.W., ALLAIRE, P.E., & THOMAS, P.W. 1989. Active magnetic control of oscillatory axial shaft vibrations in ship shaft transmission systems part 1: System natural frequencies and laboratory scale model. *Tribology Transactions*, **32(2)**, 170–178.

LI, T.Y., ZHANG, X.M., ZUO, Y.T., & XU, M.B. 1997. Structural power flow analysis for a floating raft isolation system consisting of constrained damped beams. *Journal of Sound and Vibration*, **202**(1), 47–54.

LI, V.C., LIMB, Y.M., & CHANC, Y. 1998. Feasibility study of a passive smart self-healing cementitious composite. *Composites*, **29B**, 819–827.

LIU, Y., WATERS, T.P., & BRENNAN, M.J. 2005. A comparison of semi-active damping control strategies for vibration isolation of harmonic disturbances. *Journal of Sound and Vibration*, **280**, 21–39.

LLOYD, J.M. 2004. *Electrical properties of macro-fiber composite actuators and sensors*. M.Phil. thesis, Virginia Polytechnic Institute and State University.

LOKANDER, M. 2004. *Performance of magnetorheological rubber materials*. Ph.D. thesis, KTH Fibre and Polymer Technology.

LOKANDER, M., & STENBERG, B. 2003. Performance of isotropic magnetorheological rubber materials. *Polymer Testing*, **22**(3), 245–251.

MADDEN, J., VANDESTEEG, N., ANQUETIL, P., MADDEN, P., THKSHI, A., PYTEL, R., LAFONTAINE, S., WIERINGA, P., & HUNTER, I. 2004. Artificial muscle technology : physical principles and naval prospects. *IEEE Journal of Oceanic Engineering*, **29(3)**, 706–728.

MARC, W.M. 1998. *Shape control of structures and materials with shape memory alloys*. Ph.D. thesis, Technische Universiteit Eindhoven.

MEAD, D.J. 2000. *Passive vibration control*. Wiley and Sons Ltd.

MEUNIER, M., & SHENOI, R.A. 2001. Dynamic analysis of composite sandwich plates with damping modelled using higher order theory. *Composite Structures*, **54**, 243–254.

MICHAUD-CUNNINGHAM, J. 2005. *A study of MR materials with XPCS*. Ph.D. thesis, Department of Physics, University of Michigan.

MILLER, D.W., HALL, S.R., & VON FLOTOW, A.H. 1990. Optimal control of power flow at structural junctions. *Journal of Sound and Vibration*, **140**, 475–497.

MOLLY, C.T. 1957. Use of four-pole parameters in vibration calculations. *Journal of the Acoustical Society of America*, **29**, 842–853.

MONNER, H.P., & WIERACH, P. 2005. Overview of smart-structures technology at the German Aerospace Center. *In: Institute of Composite Structures and Adaptive Systems*.

MURAYAMA, K., IKAWA, S., YAMAMOTO, S., & MURAKAMI, K. 1992. Development of propeller shaft with a new nylon coating. *Society of Automotive Engineers*, 47–57.

NAYAK, A.K., MOY, S.S.J., & SHENOI, R.A. 2005. A higher order finite element theory for buckling and vibration analysis of initially stressed composite sandwich plates. *Journal of Sound and Vibration*, **286**(4-5), 763–780.

OH, J.T., PARK, H.C., & HWANG, W. 2001. Active shape control of a double-plate structures using piezoeceramics and SMA wires. *Smart Materials and Structures*, **10**, 1100–1106.

PAN, J., PAN, J., & HANSEN, C.H. 1992. Total power flow from a vibrating rigid body to a thin panel through multiple elastic mounts. *The Journal of the Acoustical Society of America*, **92(2)**, 895–907.

PEAIRS, D.M., PARK, G., & INMAN, D.J. 2004. Practical issues of activating self-repairing bolted joints. *Smart Materials and Structures*, **13**, 1414–1423.

PEI, Q., ROSENTHAL, M., STANFORD, S., & PRAHLAD, H. 2004. Multiple-degrees-of-freedom electroelastomer roll actuators. *Smart Materials and Structures*, **13**, N86–N92.

PHANI, A.S., & VENKATRAMAN, K. 2003. Vibration control of sandwich beams using electro-rheological fluids. *Mechanical Systems and Signal Processing*, **17(5)**, 1083–1095.

PINNINGTON, R.J., & WHITE, R.G. 1981. Power flow through machine isolators to resonant and non-resonant beam. *Journal of Sound and Vibration*, **75**, 179–197.

PLANTEMA, F.J. 1966. *Sandwich construction*. John Wiley & Sons, New York.

PRENDERGAST, P.J., & MCHUGH, P.E. 2004. Topics in bio-mechanical engineering, materials and technologies for artificial muscle : a review for the mechatronic muscle project. *Pages 184–215 of: Trinity Centre for Bioengineering & National Centre for Biomedical Engineering Science*.

QU, Z.Q., & SELVAM, R.P. 2002. Efficient method for dynamic condensation of nonclassically damped vibration systems. *Aiaa Journal*, **40**(2), 368–375.

RABINOW, J. 1948. The magnetic fluid clutch. *AIEE Trans.*, **67**, 1308–1315.

RANDALL, C.A., KELNBERGER, A., YANG, G.Y., EITEL, R.E., & SHROUT, T.R. 2005. High strain piezoelectric multilayer actuators - A material science and engineering challenge. *Journal of Electroceramics*, **14(3)**, 177–191.

REDDY, J.N. 1999. *Theory and analysis of laminated composite plates*. Mechanics of Composite Materials and structures.

RIBAKOV, Y., & GLUCK, J. 2002. Selective controlled base isolation system with magnetorheological dampers. *Earthquake engineering and structural dynamics*, **31**, 1301–1324.

ROSENSWEIG, R.E. 1985. *Ferrohydrodynamics*. Cambridge University Press.

RUSTIGHI, E., BRENNAN, M.J., & MACE, B.R. 2005. Real-time control of a shape memory alloy adaptive tuned vibration absorber. *Institute of Physics Publishing*, **14**, 1184–1195.

SAHASRABUDHE, S.S., & NAGARAJAIAH, S. 2005. Semi-active control of sliding isolated bridges using MR dampers: an experimental and numerical study. *Earthquake engineering and structural dynamics*, **34**, 965–983.

SAHIN, M. 2004. *Damage identification in beam-like structures by vibration-based analysis and artificial neural networks*. Ph.D. thesis, University of Southampton.

SETAREH, M., RITCHEY, J.K., BAXTER, A.J., & MURRAY, T.M. 2006. Pendulum tuned mass damper for floor vibration control. *Journal of performance of constructed facilited*, **20(1)**, 64–73.

SHEN, Y., GOLNARAGHI, M.F., & HEPPLER, G.R. 2004. Experimental research and modeling of magnetorheological elastormers. *Journal of Intelligent Material Systems And Structures*, **15**, 27–35.

SHENOI, R.A., GROVES, A., & RAJAPAKSE, Y.D.S. 2005. *Theory and Applicantions of Sandwich Structures*. University of Southampton Press.

SHERRIT, S. 2005. Smart material/actuator needs in extreme environments in space. *In: The proceedings of the SPIE Smart Structures Conference*, vol. 5761.

SHIGA, M., HIROSE, M., & OKADA, K. 1992. Tokkai. *Japan Patents*, **Hei4266970**.

SHIGA, T., OKADA, A., & KURAUCHI, T. 2003. Magnetroviscoelastic behavior of composite gels. *Journal of Applied Polymer Science*, **58 (4)**, 787–792.

SNOWDON, J.C. 1971. Mechanical four-pole parameters and their applications. *Journal of Sound and Vibration*, **15**, 307–323.

SODANO, H.A. 2003. *Macro-fiber composites for sensing, actuation and power generation*. M.Phil. thesis, Virginia Polytechnic Institute and State University.

SOKOLINSKY, V.S., NUTT, S.R., & FROSTIG, Y. 2002. Boundary condition effects in free vibration of higher-order soft sandwich beams. *American Institute of Aeronautics and Astronautics*, **40**, 1220–1227.

SOKOLINSKY, V.S., BREMEN, H.F., LAVOIE, J.A., & NUTT, S.R. 2004. Analytical and exprimental study of free vibration response of soft-core sandwich beams. *Journal of Sandwich Structures and Materials*, **6**, 239–261.

STEPANOV, G.V., ABRAMCHUK, S.S., GRISHIN, D.A., NIKITIN, L.V., KRAMARENKO, E.YU., & KHOKHLOV, A.R. 2007. Effect of a homogeneous magnetic field on the viscoelastic behavior of magnetic elastomers. *Polymer*, **48**(2), 488–495.

STEWART, W.M., GINDER, J.M., ELIE, L.D., & NICHOLS, M.E. 1998. *Method and apparatus for reducing brake shudder, US Patent 5,816,587*.

SUN, Q., ZHOU, J.X., & ZHANG, L. 2003. An adaptive beam model and dynamic characteristics of magnetorheological materials. *Journal of Sound and Vibration*, **261**(3), 465–481.

SURESH, R., TJIN, S.C., & NGO, N.Q. 2005. Application of a new fiber Bragg grating based shear force sensor. *Smart Materilas and Structures*, **14**, 982–988.

TAO, G. 2004. *Adaptive control design and analysis*. John Wiley & Sons, Inc.

TSENG, K.K.H., & NAIDU, A.S.K. 2002. Non-parametric damage detection and characterization using smart piezoceramic material. *Smart Materials and Structures*, **11**, 317–329.

ÜBERALL, H. 1973. *Surface waves in acoustics, in Physical Acoustics, edited be W.P. Mason and R.N. Thurston*. Vol. 10. Academic, New York.

VARGA, Z., FILIPCSEI, G., & ZRÍNYI, M. 2006. Magnetic field sensitive functional elastomers with tuneable elastic modulus. *Polymer*, **47**, 227–233.

VIKAL, R.C.D., GUPTA, K.N., & NAKRA, B.C. 1981. Vibration of an excitation system supported flexibly on a viscoelastic sandwich beam at its mid-point. *Journal of Sound and Vibration*, **75(1)**, 87–99.

VINSON, J.R. 1975. *Composite materials and their use in structures*. Applied science publishers.

WACKER-SILICONES. 2005. *Material Data Sheet (Elastosil M4644 A/B)*. Tech. rept. Wacker Co.

WADA, B.K., FANSON, J.I., & CRAWLEY, E.F. 1990. Adaptive structures. *Mechanical Engineering*, 41–46.

WANG, Y., HU, Y., CHEN, L., GONG, X., JIANG, W., ZHANG, P., & CHEN, Z. 2006. Effects of rubber/magnetic particle interactions on the performance of magnetorheological elastomers. *Polymer Testing*, **25**, 262–267.

WATSON, J.R. 1997. *US Patent 5,609,353*.

WEINBERG, B., NIKITCZUK, J., FISCH, A., & MAVROIDIS, C. 2005. Development of electro-rheological fluidic resistive actuators for haptic vehicular instrument controls. *Smart Materials and Structures*, **14**, 1107–1119.

WHITNEY, J.M., & PAGANO, N.J. 1970. Shear deformation in heterogeneous anisotropic plates. *Journal of Applied Mechanics*, 1031–1036.

WILKIE, W.K., BRYANT, R.G., HIGH, J.W., FOX, R.L., HELLBAUM, R.F., JALINK, A., LITTLE, B.D., & MIRICK, P.H. 2000. Low-cost piezocomposite actuator for structural control applications. *NASA Langley Research Center, Hampton, VA 23681-2199*.

XIONG, Y.P. 1996. *Power flow transmission mechanisom and optimum control of complex coupled flexible system of machinery and foundation*. Ph.D. thesis, Shandong University of Technology.

XIONG, Y.P., & SONG, K.J. 1996. Power flow analysis for a new isolation system-flexible floating raft. *Chinese Journal of Mechanical Engineering*, **9**, 260–264.

XIONG, Y.P., SONG, K.J., & AI, X. 1996. Influence of flexible foundation on isolator wave effects. *Shock And Vibration*, **3**(1), 61–67.

XIONG, Y.P., XING, J.T., PRICE, W.G., & WANG, X.P. 2000. Hybrid active and passive control of vibratory power flow in flexible isolation system. *Shock And Vibration*, **7**(3), 139–148.

XIONG, Y.P., XING, J.T., & PRICE, W.G. 2001. Power flow analysis of complex coupled systems by progressive approaches. *Journal of Sound and Vibration*, **239**(2), 275–295.

XIONG, Y.P., XING, J.T., PRICE, W.G., & SHENOI, R.A. 2002. Active control of energy flow from source to equipment on a sandwich panel. *In: Proceedings of the 5th International Conference on Vibration Engineering*. China Aviation Industry, Nanjing, China.

XIONG, Y.P., XING, J.T., & PRICE, W.G. 2003. A general linear mathematical model of power flow analysis and control for integrated structure-control systems. *Journal of Sound and Vibration*, **267(2)**, 301–334.

XIONG, Y.P., XING, J.T., & PRICE, W.G. 2005. A power flow mode theory based on a system's damping distribution and power flow design approaches. *Proceeding of The Royal Society A*, **461**, 3381–3411.

YALCINTAS, M., & DAI, H. 2004. Vibration Suppression Capabilities of Magnetorheological Materials Based Adaptive Structures. *Smart Materials and Structures*, **13**, 1–11.

YANG, M., & QIAO, P. 2005. Modeling and experimental detection of damage in various materials using the pulse-echo method and piezoeletric sensors/actuators. *Smart Matererials and Structures*, **14**, 1083–1100.

YIN, H.M., SUN, L.Z., & CHEN, J.S. 2006. Magneto-elastic modeling of composites containing chain-structured magnetostrictive particles. *Journal of the Mechanics and Physics of Solids*, **54**, 975–1003.

YOSHIKAWA, S., FARRELL, M., WARKENTIN, D., JACQUES, R., & SAARMAA, E. 1999. Monolithic piezoelectric actuators and vibration dampers with interdigitated electrodes. *Proceedings SPIE 6th international symposium on smart structures and materials*.

ZENKERT, D. 1997. *An introduction to sandwich construction*. The chameleon press LTD, London.

ZHANG, Y. 2001. *Semi-active control of dynamically excited structures using active interaction control*. Ph.D. thesis, California Institute of Technology.

ZHOU, G.Y. 2003. Shear properties of a magnetorheological elastomer. *Smart Materilas and Structures*, **12**, 139–146.

ZHOU, G.Y., & WANG, Q. 2005. Magnetrorhelogical elastomer-based smart sandwich beams with nonconductive skins. *Smart Materilas and Structures*, **14**, 1001–1009.

ZHOU, G.Y., & WANG, Q. 2006. Use of magnetorheological elastomer in adaptive sandwich beam with conductive skins. Part II: dynamic property. *International journal of Solids and Structures*, **43**, 5403–5420.

Appendix A

Component of mass and stiffness matrix for simply supported beam

The present appendix stores the following expressions that are essential for the calculation of mass matrix **M** and stiffness matrix **K** to be used to evaluate eigenvalue in the section 7.2 discuss elsewhere in the thesis.

From Eq. 7.23 matrices of the mass and the complex stiffness are presented as follows (Choi *et al.* , 2007),

$$
\begin{aligned}
\mathbf{M}_{11} &= m_t + \frac{1}{12} m_c d_t^2 \kappa^2 + \frac{1}{3} m_c \\
\mathbf{M}_{12} &= \frac{1}{6} m_c - \frac{1}{24} m_c d_t d_b \kappa^2 \\
\mathbf{M}_{13} &= -\frac{1}{6} m_c d_t \kappa \\
\mathbf{M}_{14} &= -\frac{1}{12} m_c d_t \kappa
\end{aligned}
$$

$$
\begin{aligned}
\mathbf{M}_{21} &= \frac{1}{6} m_c - \frac{1}{24} m_c d_t d_b \kappa^2 \\
\mathbf{M}_{22} &= m_b - \frac{1}{12} m_c d_b^2 \kappa^2 + \frac{1}{3} m_c \\
\mathbf{M}_{23} &= \frac{1}{12} m_c d_b \kappa \\
\mathbf{M}_{24} &= \frac{1}{6} m_c d_b \kappa
\end{aligned}
$$

$$
\begin{aligned}
\mathbf{M}_{31} &= \frac{1}{6}m_c d_t \kappa \\
\mathbf{M}_{32} &= -\frac{1}{12}m_c d_b \kappa \\
\mathbf{M}_{33} &= -m_t - \frac{1}{3}m_c \\
\mathbf{M}_{34} &= -\frac{1}{6}m_c
\end{aligned}
$$

$$
\begin{aligned}
\mathbf{M}_{41} &= \frac{1}{12}m_c d_t \kappa \\
\mathbf{M}_{42} &= -\frac{1}{6}m_c d_b \kappa \\
\mathbf{M}_{43} &= -\frac{1}{6}m_c \\
\mathbf{M}_{44} &= -m_b - \frac{1}{3}m_c
\end{aligned}
$$

$$
\begin{aligned}
\mathbf{K}_{11} &= EI_t\kappa^4 + bE_c^*/c \\
\mathbf{K}_{12} &= -bE_c^*/c \\
\mathbf{K}_{13} &= 0 \\
\mathbf{K}_{14} &= 0 \\
\mathbf{K}_{15} &= \frac{1}{2}\kappa b(c + d_t)
\end{aligned}
$$

$$
\begin{aligned}
\mathbf{K}_{21} &= -bE_c^*/c \\
\mathbf{K}_{22} &= EI_b\kappa^4 + bE_c^*/c \\
\mathbf{K}_{23} &= 0 \\
\mathbf{K}_{24} &= 0 \\
\mathbf{K}_{25} &= \frac{1}{2}\kappa b(c + d_b)
\end{aligned}
$$

$$
\begin{aligned}
\mathbf{K}_{31} &= 0 \\
\mathbf{K}_{32} &= 0 \\
\mathbf{K}_{33} &= -EA_t\kappa^2 \\
\mathbf{K}_{34} &= 0 \\
\mathbf{K}_{35} &= b
\end{aligned}
$$

$$
\begin{aligned}
\mathbf{K}_{41} &= 0 \\
\mathbf{K}_{42} &= 0 \\
\mathbf{K}_{43} &= 0 \\
\mathbf{K}_{44} &= -EA_b\kappa^2 \\
\mathbf{K}_{45} &= -b
\end{aligned}
$$

$$
\begin{aligned}
\mathbf{K}_{51} &= \frac{1}{2}\kappa b(c+d_t) \\
\mathbf{K}_{52} &= \frac{1}{2}\kappa b(c+d_b) \\
\mathbf{K}_{53} &= -b \\
\mathbf{K}_{54} &= -b\kappa^2 \\
\mathbf{K}_{55} &= \frac{c}{G_c^*} + \frac{c^3 b}{12E_c^*}\kappa^2
\end{aligned}
$$

where m_t, m_b, m_c are mass of top, bottom and core respectively and b is the width of the core and κ is $n\pi/L$, where L is the length of the beam.

Appendix B

Numerical coefficients for governing equation by using central difference method

Discretized equations in terms of five variables, w_t, w_b, u_t, u_b and τ, are described as follows,

$$\begin{aligned} a_1 w^t_{i-2} + b_1 w^t_{i-1} + c_1 w^b_{i-1} + d_1 u^t_{i-1} + e_1 u^b_{i-1} + f_1 \tau_{i-1} + g_1 w^t_i + h_1 w^b_i \\ + i_1 w^t_{i+1} + j_1 w^b_{i+1} + k_1 u^t_{i+1} + l_1 u^b_{i+1} + m_1 \tau_{i+1} + n_1 w^t_{i+2} = 0 \end{aligned} \tag{B.1}$$

$$\begin{aligned} a_2 w^b_{i-2} + b_2 w^t_{i-1} + c_2 w^b_{i-1} + d_2 u^t_{i-1} + e_2 u^b_{i-1} + f_2 \tau_{i-1} + g_2 w^t_i + h_2 w^b_i \\ + i_2 w^t_{i+1} + j_2 w^b_{i+1} + k_2 u^t_{i+1} + l_2 u^b_{i+1} + m_2 \tau_{i+1} + n_2 w^b_{i+2} = 0 \end{aligned} \tag{B.2}$$

$$\begin{aligned} a_3 w^t_{i-1} + b_3 w^b_{i-1} + c_3 u^t_{i-1} + d_3 u^t_i + e_3 u^b_i + f_3 \tau_i + g_3 w^t_{i+1} + h_3 w^b_{i+1} \\ + i_3 u^t_{i+1} = 0 \end{aligned} \tag{B.3}$$

$$\begin{aligned} a_4 w^t_{i-1} + b_4 w^b_{i-1} + c_4 u^t_{i-1} + d_4 u^t_i + e_4 u^b_i + f_4 \tau_i + g_4 w^t_{i+1} + h_4 w^b_{i+1} \\ + i_4 u^t_{i+1} = 0 \end{aligned} \tag{B.4}$$

$$a_5 w^t_{i-1} + b_5 w^b_{i-1} + c_5 \tau_{i-1} - u^t_i + u^b_i + d_5 \tau_i + e_5 w^t_{i+1} + f_5 w^b_{i+1} + g_5 \tau_{i+1} = 0. \tag{B.5}$$

where,

$$
\begin{aligned}
a_1 &= \frac{EI_t}{h^4} \\
b_1 &= -\frac{4EI_t}{h^4} - \frac{m_c d_t^2}{12h^2} \\
c_1 &= \frac{m_c d_t d_b}{24h^2} \\
d_1 &= -\frac{m_c d_t}{12h} \\
e_1 &= -\frac{m_c d_t}{24h} \\
f_1 &= \frac{b(c + d_t)}{4h} \\
g_1 &= \frac{6EI_t}{h^4} + \frac{bE_c}{c} + m_t + \frac{m_c d_t^2}{6h^2} + \frac{m_c}{3} \\
h_1 &= -\frac{bEc}{c} - \frac{m_c d_t d_b}{12h^2} + \frac{1}{6m_c} \\
i_1 &= -\frac{4EI_t}{h^4} - \frac{m_c d_t^2}{12h^2} \\
j_1 &= \frac{m_c d_t d_b}{24h^2} \\
k_1 &= \frac{m_c d_t}{12h} \\
l_1 &= \frac{m_c d_t}{24h} \\
m_1 &= -\frac{b(c + d_t)}{4h} \\
n_1 &= \frac{EI_t}{h^4}
\end{aligned}
$$

$$
\begin{aligned}
a_2 &= \frac{EI_b}{h^4}\\
b_2 &= \frac{m_c d_t d_b}{24h^2}\\
c_2 &= -\frac{4EI_b}{h^4} - \frac{m_c d_b^2}{12h^2}\\
d_2 &= \frac{m_c d_b}{24h}\\
e_2 &= \frac{m_c d_b}{12h}\\
f_2 &= \frac{b(c+d_b)}{4h}\\
g_2 &= -\frac{bEc}{c} - \frac{m_c d_t d_b}{12h^2} + \frac{1}{6m_c}\\
h_2 &= \frac{6EI_b}{h^4} + \frac{bE_c}{c} + m_b + \frac{m_c d_b^2}{6h^2} + \frac{m_c}{3}\\
i_2 &= \frac{m_c d_t d_b}{24h^2}\\
j_2 &= -\frac{4EI_b}{h^4} - \frac{m_c d_b^2}{12h^2}\\
k_2 &= -\frac{m_c d_b}{24h}\\
l_2 &= -\frac{m_c d_b}{12h}\\
m_2 &= -\frac{b(c+d_b)}{4h}\\
n_2 &= \frac{EI_b}{h^4}
\end{aligned}
$$

$$
\begin{aligned}
a_3 &= -\frac{m_c d_t}{12h} \\
b_3 &= \frac{m_c d_b}{24h} \\
c_3 &= \frac{EA_t}{h^2} \\
d_3 &= -\frac{2EA_t}{h^2} - m_t - \frac{m_c}{3} \\
e_3 &= -\frac{m_c}{6} \\
f_3 &= b \\
g_3 &= \frac{m_c d_t}{12h} \\
h_3 &= -\frac{m_c d_b}{24h} \\
i_3 &= \frac{EA_t}{h^2}
\end{aligned}
$$

$$
\begin{aligned}
a_4 &= -\frac{m_c d_t}{24h} \\
b_4 &= \frac{m_c d_b}{12h} \\
c_4 &= \frac{EA_b}{h^2} \\
d_4 &= -\frac{m_c}{6} \\
e_4 &= -\frac{2EA_b}{h^2} - m_b - \frac{m_c}{3} \\
f_4 &= -b \\
g_4 &= \frac{m_c d_t}{24h} \\
h_4 &= -\frac{m_c d_b}{12h} \\
i_4 &= \frac{EA_b}{h^2}
\end{aligned}
$$

$$
\begin{aligned}
a_5 &= -\frac{b(c+d_t)}{4h} \\
b_5 &= -\frac{b(c+d_b)}{4h} \\
c_5 &= \frac{c^3 b}{12h^2 E} \\
d_5 &= -\frac{cb}{G_c} - \frac{c^3 b}{6Eh^2} \\
e_5 &= \frac{b(c+d_t)}{4h} \\
f_5 &= \frac{b(c+d_b)}{4h} \\
g_5 &= \frac{c^3 b}{12h^2 E}
\end{aligned}
$$